UNIVERSITY OF SOUTHAMPTON

Faculty of Engineering and Physical Sciences
School of Physics and Astronomy

An Investigation into Extreme Light Scattering in Disordered Photonic Networks

by

Luke Richard Burke

A thesis for the degree of
Doctor of Philosophy

June 2025

University of Southampton

Abstract

Faculty of Engineering and Physical Sciences
School of Physics and Astronomy

Doctor of Philosophy

An Investigation into Extreme Light Scattering in Disordered Photonic Networks

by Luke Richard Burke

Disordered photonic networks provide a unique environment to explore light scattering on the mesoscopic scale. The physical description of multiple scattering in strongly scattering random media is an ongoing field of research, with many theoretical and numerical models exploring the phase transition of light from the diffusive to the localised regime. Experimental verification of these theories is necessary to determine the validity of these results. In this thesis, a novel experimental spatio-temporal pump probe technique is used to characterise anisotropic scattering in GaP nanowire mats to determine the diffusion constant in the transverse and longitudinal directions. Coherent backscatter and total transmission and reflection spectroscopy are used to determine optical characteristics such as the transport mean free path and absorption length. Results corroborate previous independent measurements and promote the use of the pump probe technique for studying anisotropic diffusive light transport.

The multiple scattering process also forms an obstruction to optical imaging through disordered media, such as in clouds or biological tissue. The existence of correlations in the speckle of coherently transmitted or reflected light provides an opportunity to detect information of the target object through seemingly opaque media. Previous works focus on the optical memory effect and its application in such environments. The Lorentz reciprocity of scattered light in the time reverse optical memory effect allows for detection of a specific signal unique to the scattering target; which presents the opportunity for advancement in the field of imaging through scattering media. This phenomenon is explored experimentally, a phase based modulation of the process is characterised, and the principle is then demonstrated in a pulsed optical system.

Contents

List of Figures

List of Tables

Declaration of Authorship

I declare that this thesis and the work presented in it is my own and has been generated by me as the result of my own original research.

I confirm that:

1. This work was done wholly or mainly while in candidature for a research degree at this University;
2. Where any part of this thesis has previously been submitted for a degree or any other qualification at this University or any other institution, this has been clearly stated;
3. Where I have consulted the published work of others, this is always clearly attributed;
4. Where I have quoted from the work of others, the source is always given. With the exception of such quotations, this thesis is entirely my own work;
5. I have acknowledged all main sources of help;
6. Where the thesis is based on work done by myself jointly with others, I have made clear exactly what was done by others and what I have contributed myself;
7. None of this work has been published before submission

Signed:..... Date:.....

Acknowledgements

This thesis is the product of many years of study, experimentation, and persistence. None of it could have been realised without the significant support of a number of individuals. Firstly, I would like to thank my primary supervisor, Prof. Otto Muskens for his constructive discussion, enthusiastic experimental contribution, and academic guidance. I would also like to thank my secondary supervisor, Dr. Idris Ajia, whose advice and company in the lab was invaluable to me and the project.

A special thank you to my good friends and colleagues Dr. Callum Wheeler and Megan Freeman, whose time was greatly appreciated and their sympathy reciprocated. My thanks go to Dr. Jake Daykin and Dr. Daniel Lawson for their help during the many long days of lab work. Great appreciation goes to all members of the Integrated Nanophotonics Group and the Quantum Light and Matter Group, who have made the past few years far more enjoyable than they otherwise would have been, I will always cherish their friendship, humour, and camaraderie.

I would like to express my deepest gratitude to my parents for their endless support, love and patience. Finally, I would like to thank my partner Hannah McGovern who has stuck with me through this sometimes Sisyphean endeavour and wish her all my best with her own doctoral studies.

Chapter 1

Introduction

Random scattering in disordered media has been the subject of physical study for centuries, from thermodynamics, to electronics, to quantum mechanics, all manner of interactions require the study of particles, objects, or waves scattering off of one another. The incorporation of electromagnetism into this broad picture gives rise to the study of the scattering of light. The single scattering of light waves from single small particles, mesoscopic spheres, and larger geometric objects is well described by predicting the electromagnetic field as it propagates and is perturbed by the object. The progression from single to multiple scattering creates a new mathematical environment in which the classical description of light no longer accurately depicts the physical processes, and with the advent of quantum mechanics a more detailed picture evolved. This was researched extensively in the latter half of the 20th century up to today, leading to a number of discoveries and advancements.

Disordered light scattering is a physical phenomena which is currently being implemented across many areas of research, including improving solar cell efficiency (1)(2)(3), designing random lasers (4), and creating random lenses (5). Alongside its industrial and practical scientific applications, there are areas of theoretical research that are yet to be verified experimentally with regards to disordered light scattering. The most prominent of these is Anderson localisation of light in three dimensions. This elusive scattering regime has been the focus of many research groups in the past few decades, both experimental and theoretical, however it has yet to be demonstrated experimentally with certainty, leading to an ongoing debate of its likelihood of realisation (6)(7).

More recently, a promising outlook is presented by Yamilov et al. (8), where a review of the mechanisms inhibiting the manifestation of three dimensional light localisation is performed and a new system is presented in which these are negated, resulting in a numerical simulation of a localised state of electromagnetic waves in a slab of perfect electrically conducting spheres. Hallmarks of this localisation include the existence of extremely long light paths inside the material, deviating from the diffusive description

of light propagation. Another is the reduced transverse spatial extent of the light at the exit surface of the material. The novel methodology shown in this thesis allows for the direct measurement of the spatial extent of the transmitted light from such scattering materials, as well as ultrafast detection of the transmitted intensity allowing for the determination of the decay of the long light paths.

One highly active field of research within the umbrella of disordered scattering is the correlation of fields produced by multiple scattering of coherent sources. The speckle pattern, a randomised spatial or spectral distribution of intensities produced by waves propagating through disordered media, is found to contain rich information about the system through which it passes, and retains information from its source. For this reason it is termed the optical memory effect (OME). This is exploited in modern practices for medical and sensing applications, and research is ongoing for new applications and improvements.

The time reverse memory effect (TRME) is a specific contribution to the correlation of speckle patterns due to the time reversal symmetry of scattered light, thus it is inherently specific to the target. If it were possible to implement the specific signal of the TRME it would present a stable signal which could reduce the noise contribution from environmental sources. The OME has been well established and studied in the transmission geometry, as this is often the case for practical applications, however a limited number of studies have examined the reflection geometry and the TRME since its discovery by Freund et al. (9) in 1988. A more detailed study of the effect and the correlation is therefore required, especially regarding the phase dependence as it is the phase stability under multiple scattering which enables the application of the memory effect.

In this thesis a number of established and novel experimental techniques are used to investigate the scattering of light on the mesoscopic scale. A modified pump probe technique is used to measure anisotropic scattering in strongly scattering gallium phosphide nanowire samples. This technique combines ultra-fast laser pulses and lock-in detection to measure a non-linear response in the semiconducting nanowires, giving time of flight information across the exit surface of the sample without the use of interferometry. Finally, an experimental investigation into the phase dependence of speckle correlation is undertaken, utilising the TRME in both continuous wave and pulsed optical systems.

There is a vast range of opportunity for discovery in the field of disordered light scattering, recent theoretical progress has once again outstripped experimental studies and there remains a number of unsolved, and possibly unseen, experimental challenges to overcome in order to realise the predicted physical manifestations of strong Anderson localisation of light. Anisotropic scatterers remain an avenue of possibility for quasi-one or two dimensional localisation, and the interplay between this effect and

the transverse diffusion of photons should be taken into account. It has been recently experimentally demonstrated that near the mobility gap produced by strong Anderson localisation, the effect of anisotropic scattering by individual scatterers reduces, leading to a less ellipsoidal transmittance at the output (10). To begin this process, a determination of the anisotropic diffusion of light in strongly scattering samples is undertaken.

The aim of this project is to investigate the propagation of light through disordered strongly scattering media on the mesoscopic scale. This is done by developing new methodologies to characterise strongly scattering materials within the theoretical descriptions established in literature. Specifically the main areas of study will be diffusive light propagation, scattering anisotropy and speckle correlation:

- Measure the transport of light in a strongly scattering disordered photonic network and compare this with the diffusive model of light propagation.
- Investigate anisotropic light diffusion in a strongly scattering sample and compare this with the diffusive model of light propagation.
- Measure the phase dependence of the time reverse memory effect, verifying the conservation of phase throughout the multiple scattering process via cross correlation of speckles.

The diffusive description of light transport in scattering media is well established, recent works have made significant progress in determining both the theoretical and experimental limits of this approximation, i.e. where the diffusive picture should break down. This project aims to certify that the diffusive model continues to describe the strong scattering seen in strongly scattering samples which have been characterised using a range of separate techniques.

Anisotropic light scattering is an area of significant interest of the report. The anisotropy exploited in liquid crystals and nanomaterial design has opened new pathways in the development of optical displays and metamaterials. It has been recently experimentally demonstrated that near the mobility gap produced by strong Anderson localisation, the effect of anisotropic scattering by individual scatterers reduces, leading to a less ellipsoidal transmittance at the output (10). The development of new techniques to measure the anisotropy of random, multiply scattering materials may help to provide further avenues of research and hence enable development of useful optical properties. (11)

Finally the correlation of speckles produced by coherent waves is a useful tool in measuring the properties of scattering media, and for interrogating features or objects hidden behind or inside them. Experimental investigation of the phase dependence of the time reverse memory effect and the proposal of a new technique could lead to the improvement of signal stability in future experiments.

1.1 Thesis Structure

Chapter 2 provides the theoretical background of the work, comprising of a review of literature pertaining to the topics discussed. A foundation of understanding is established in light scattering and disordered light-matter interactions, before a more in depth mathematical description is provided of the diffusive propagation of light in strongly scattering environments. This is presented in terms of transmission and time of flight, and then further in terms of speckle correlations and reflection based geometries.

Chapter 3 details optical characterisation measurements of samples to be used in later chapters. Various experimental techniques are used, including total transmission and reflection spectroscopy, coherent backscatter spectroscopy and dark field spectroscopy.

Chapter 4 presents an all optical pump probe experiment which allows stroboscopic microscopy of extremely scattering samples. The methodology and experimental technique are discussed, as well as an explanation of some of the effects which can be detrimental to obtaining a measurement and how they can be mitigated. Time of flight measurements as well as spatial distributions are obtained and fitted using theoretical descriptions developed in chapter 2, culminating in a comparison of the diffusion constants of samples which have undergone mechanical compression.

Chapter 5 is the third experimental chapter, presenting an experimental exploration of the time reversal symmetry of the optical memory effect, developing from the angular and spatial correlation of time reverse speckle patterns, to the control of phase difference in the Sagnac interferometer geometry and finally to application to a pulsed regime.

Concluding remarks and future works are discussed in chapter 6.

Chapter 2

Theoretical Background

2.1 Mesoscopic Light Matter Interaction

Mesoscopic scattering of waves in disordered media continues to be an area of keen research in a variety of fields due to both its broad applications and use cases, as well as its complex theoretical basis. This drives a theoretical and experimental motivation to understand these complex interactions and a practical desire to apply this knowledge in new technologies and methodologies. This section of the report will discuss the progress that has been made in the former, explaining the physical concepts which form the basis of this investigation.

The scattering of a wave can occur when it interacts with a scattering object or encounters a change in the medium of propagation. For optical scattering, the refractive index of the material is a key parameter in determining the strength of the interaction between the light wave and the material, hence higher index material contrasts are preferable for strong light scattering.

The size of the scatterer has a strong effect on the way light will interact with the object, relative to the wavelength of the incoming wave. When the scatterer is much smaller than the wavelength of the incoming light, the scattering occurs in the Rayleigh scattering regime:

$$I_{sc} \propto \frac{I_0}{\lambda^4} \tag{2.1}$$

in this regime there is an inverse power law dependence of the scattered light intensity on wavelength, and it is well known that it is this dependence which gives rise to the rich colours of the sky during the day as well as at sunrise and sunset.

In mesoscopic systems where the size of the scatterer is of the same order as the wavelength of the light, the scattering interactions tend to be stronger and thus are more likely to give rise to multiple interactions. Continuing with the example of atmospheric

phenomena, it is this regime which gives rise to the whitish grey colouration of clouds. Water droplets which condense in clouds are spheres with diameters of the order of nanometers to microns, overlapping with the visible and near infra-red spectrum. Due to their relatively strong interaction and variety in size, light rays over a broad spectrum from the sun are scattered multiple times inside the cloud before they escape and propagate to us on the ground. This causes any spatial coherence in the waves to be lost, thus obscuring what is beyond the clouds and giving rise to a relatively uniform distribution of intensity. This scattering regime is called Mie scattering and is well described for spherical objects (12).

Mie theory encompasses the interaction of electromagnetic waves with spherical and cylindrical objects which incorporate a form of radial or angular symmetry. In most cases it is applied to objects of size comparable to the wavelength of the incident light. The solutions are obtained by solving Maxwell's equations at the surface of the object and gives absorption and scattering cross-sections for the particle. This is caused by the charge carrier density currents that arise due to the electric and magnetic field interacting with charges on the surface of and inside the sphere (13). As the size of the sphere increases, these resonances shift towards higher wavelengths, meaning that by tuning the size of these spheres it is possible to control the wavelength dependence of the scattering cross Section (14).

However, this sensitive size dependence can also be a significant challenge because a small distribution in sizes leads to a significant broadening of the resonant peaks. Another issue to contend with is that larger spheres also produce higher order polar responses which reduces the intensity of the dipole and quadripole resonances and can lead to a flattening of the response. Although Mie theory only explicitly applies to spheres, the concept is similar for antenna-like structures as well as nanowires, whereby the size, shape and orientation of the mesoscopic object is strongly related to its optical properties (13).

Mie resonators with highly controllable dimensions have been used to great effect to produce metamaterials with predetermined optical properties. By adjusting the diameter and length of ordered arrays of silicon nanocylinders, Seo et al. (15) were able to produce tunable absorption patterns in the observable optical frequencies, producing mats of varying colours. Other optical properties which are difficult or possibly impossible to achieve using other techniques have also been realised using structured metamaterials, such as a negative index of refraction (16). This enabled further breakthroughs such as the development of the theory of a perfect lens (17). Ordered arrays of silicon nanodisks have also been shown to produce an effective anti-reflection coating, allowing strong coupling into the substrate, with applications again in light harvesting (18). Although the highly ordered structure of metamaterials does not exactly fit within the area of interest of this project, the strength of the Mie resonances and thus

the changes in the optical properties of the material exemplifies what can be achieved with such devices.

Dielectric materials, such as silicon, produce not only electric Mie resonances but also magnetic ones. These magnetic dipole and multipole resonances can greatly enhance the scattering efficiency of the material (19)(20) and can produce strong nonlinear responses (21) such as the Kerker effect (22). In such a case the overlap of the electric and magnetic resonances can lead to complete forward or back scattering. Tunable electric and magnetic dipoles have recently been measured separately in colloidal silicon nanospheres by using linearly polarised light and altering the polarisation of the detected light (14). This is possible since the dipole resonances are orientated according to the polarisation of the incident light. By tailoring the density of the scatterers within the colloid (or fill fraction of the meta-fluid) and the diameter of the scatterers (and thus the wavelength dependence of the resonant scattering), the fluid exhibits a highly controllable effective refractive index. Spherical silicon nanospheres have also been used to create micro-resonators which have a wavelength dependent absorption coefficient, which leads to more efficient absorption in the infra-red region (23).

Metals with free charge carriers can also produce strong interactions with light, due to the induced oscillation of the free charge carriers within the metal. The name given to the quantum of these oscillations is a plasmon and it has a resonant frequency again dependant upon the material properties. Plasmonic devices have proved to be very efficient tools in electronic and optical devices, with applications ranging from enhanced Raman spectroscopy to biochemical sensing. One downside to using metallic resonators however is that they often have large losses at and around their peak scattering resonances. This is significant since inelastic scattering losses cause a breakdown of the scattering process and therefore inhibits light localisation, as will be explained in Section 2.2.

The main samples studied in this thesis are a strongly scattering mat of gallium phosphide nanowires. Gallium phosphide is a semiconducting material with a high refractive index in the infarred region ($\sim$ 3.1 in the region of interest) and a relatively low absorption coefficient. The band gap is situated at $\sim 582\,nm$ in the bulk material. The nanowires are grown using metal-organic vapour phase epitaxy (MOVPE)(24). The nanowires are grown using two different substrates with crystal lattice structures (111) and (100). The different substrates lead to growth preferentially along the vertical in the case of the 111 substrate, or distributed across a larger range of angles showing a perpendicular component to the growth in the case of the 100 substrate. In the course of this thesis the samples will be referred to by the crystalline structure of the substrates, 100 and 111.

The role of disorder in the propagation of light in scattering environments has been discussed for decades. Seminally, (25) proposed the complex interference of waves leading

to a phase transition in the material, arising from the disordered nature of the structure itself. Highly ordered structures such as photonic crystals exhibit well defined properties and can give rise to photonic band-gaps, spectral regions in which light transport is prohibited (26)(27). The transition from ordered to disordered and hyperuniform structures has been subject to great study (28)(29).

2.2 Multiple Scattering: Diffusion and Localisation

2.2.1 Diffusion Approximation

In a multiply scattering system, whereby multiple interactions lead to a rapid randomisation of the direction of propagation, a diffusion approximation can be introduced which describes the transport as a differential equation in time and space. For an optical system the scattering centres may be realised as particles in a surrounding medium with a contrast in the refractive index. In classical terms, and taking the scattering to be elastic such that there is no energy loss over time, light can be treated in this case as analogous to a single scattering particle traversing the space with a fixed velocity.

The picture becomes more complex when the scattering object is treated as a wave or wavefunction, as the intensity or observable characteristics such as position and velocity, become subject to self interference and, in the case of transverse vector waves, polarisation dependence. The effect of polarisation dependence is largely ignored in the theoretical treatment of the diffuse propagation of light in a random media as discussed in Chapter 4, however it becomes much more significant in the context of coherent back scatter, the subject of Section 2.2.2.

2.2.2 Coherent Backscatter

If a material is sufficiently scattering, light which is incident on the material may also become scattered back towards its direction of entry, or back-scattered. This can lead to light paths inside the material which are symmetric under time reversal as shown in Figure 2.1, and if the incident light is coherent this can produce interference effects due to the reciprocal paths inducing the same change in phase, and therefore constructive interference and a positive enhancement of the intensity called a coherent back scatter (CBS) cone (30).

When light follows these two paths simultaneously, and exits the sample at the same angle, their contribution to the specular intensity as a result of their superposition is dependent upon their phase difference, which is a function of the length of their path through the sample. The sum of contributions from the many paths which can be explored by light within the sample tends towards an enhancement of the intensity as the

difference in angle, and phase, approaches zero. As the difference in angle increases away from the exact back-scatter direction, the phase of the light along the two paths begins to separate also, returning to the randomisation of phase which averages away to no significant contribution, thus giving a cone of higher intensity of light centred around this exact backscatter direction(31).

The interference is possible due to the polarisation of the scattered light being retained throughout the scattering process. For light which enters the material vertically polarised and exits the material vertically polarised, light following the reciprocal path will interfere, whereas for light which enters in the same fashion but exits the material horizontally polarised, the light paths are no longer symmetric under time reversal and thus will not cause interference. The strong vector dependence of the localisation effects thus provides an easy method for detecting the coherent back-scatter, as a polarised coherent light source may be directed onto the sample and the diffuse background and coherent back-scatter can be measured by observing the scattered light in parallel and cross polarisation orientations respectively.

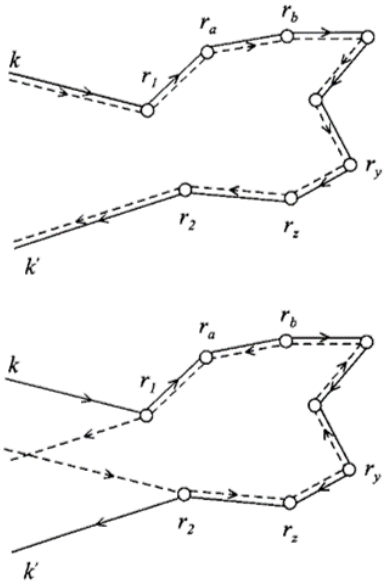

FIGURE 2.1: Illustration of the random walk of light rays in a multiply scattering medium. Incoming and outgoing wave vectors are labelled k, k', scattering paths between positions r_1 and r_2 are shown for co-propagating (above) and counter-propagating (below) transport directions. Figure reproduced from reference (32).

This approach using polarisation to measure the normalised coherent backscatter (CBS) is valid for point like particles in the Rayleigh-Gans or Rayleigh limit, however does not describe mesoscopic scattering well (33). For this reason the CBS cone is also normalised to a reference scattering material with a relatively Lambertian diffuse reflection and extremely narrow CBS cone, corresponding to a very long transport mean free path inside the material.

The enhancement factor of CBS from a disordered slab of finite thickness is limited by the size and thickness of the slab. When measuring the coherent backscatter, since the very tip of the CBS cone is formed of the longest light paths and these paths are most likely to escape or become attenuated in the material, this can lead to a rounding in the cone. The angular dependence of this CBS cone is given by a function of the transport mean free path, l_t, for polarised light as

$$\theta_{FWHM} \approx \frac{0.7}{k_0 l_t}, \tag{2.2}$$

where θ_{FWHM} is the full width half maximum of the cone of coherent back scatter and k_0 is the wavenumber of the light (34).

Another limit to the experimentally measured enhancement factor is due to the choice of reference. An ideal reference material produces a purely diffuse scattering profile over all wavelengths, with no enhancement in the exact backwards direction, yet with a transport mean free path sufficiently short to be practically workable. So far no such ideal material has been found, however polytetrafluoroethylene (PTFE) produces a broadly diffuse scattering profile across a wide range of wavelengths from the visible to near infrared while having a very narrow CBS cone over this range. The alternative is to polarise the incident light and measure the CBS cone in the parallel channel, then measure the perpendicular channel as the reference. As mentioned previously, this is possible due to elastic scattering interactions and the preservation of polarisation. When measuring over a wide range of wavelengths, it is important to ensure that any polarising optical device used in this method has a uniform performance.

The measurement of the mean free path of the scattering gallium phosphide nanowires used in this thesis was originally characterised in 2009 (35). It was surmised that the strong light-matter interaction exhibited was caused by resonant scattering occurring along the radial axis of the nanowires, as opposed to the longitudinal (or length-wise) direction. Resonant scattering may also lead to a resonant behaviour in the transport mean free path, and hence the energy transport velocity through a diffusive medium (36).

In their 2017 paper, Schertel et al. (37) were able to measure coherent back-scattering and speckle correlations in mixtures of cerium fluoride (CeF_3), titanium oxide (TiO), and glycerol. Due to the Faraday rotation which can be induced by magnetic fields, they were able to break the reciprocity of the material and thus measure a reduction in the central coherent back-scattered cone. Another important point to be made when considering these findings is that the weak localisation is still present when the scattering nanoparticles are dispersed in a medium with relatively high refractive index ($\sim$1.46) compared to air.

It is also possible to alter the refractive index of the material on short timescales within the dwell time of the light within the sample in order to break the reciprocity of the time reverse paths. This was demonstrated in porous GaP substrates in 2012 (38), in a process similar to that which is used in the experiments shown in Chapter 4. A high intensity pump pulse causes a change to the refractive index via photoinduced absorption of a probe pulse, which is then measured using lock-in detection.

2.2.3 Anderson Localisation of Light

The theory of Anderson localisation predicts that in a sufficiently disordered electrically conducting material, strong scattering of the electrons due to impurities and imperfections in the crystal lattice would lead to a reduction of the mean free path of the electrons, ultimately causing a phase transition from a conducting to an insulating phase, as the electron transport transitions to a localised state (25). Inside a metal or semiconducting material, sufficiently disordered defects in the crystal lattice can act as such scattering centres, and this effect has been demonstrated in electronic conductance fluctuations (39) and using sound waves in a three dimensional scattering medium (40).

It was postulated that since this is a general wave based phenomenon it could be extended to acoustic and electromagnetic (EM) waves among others, and has since been uncovered in several of these areas (39). In 2016 Cobus et al. (41) were able to demonstrate Anderson localisation in ultrasonic waves in three dimensions using a dynamic coherent backscattering method. The fits to the self consistent theory of localisation demonstrated a localisation length smaller than the sample thickness over a range of frequencies. Several key differences between other models an and the electromagnetic model exist however, such as the existence of electron-electron interactions due to coulomb repulsion which can result in Mott localisation, a distinct effect. Weak localisation has been identified in many disordered photonic media and transverse strong localisation has been shown in disordered two dimensional photonic lattices (42).

The dimensionality of the problem significantly affects the likelihood of this occurrence. It has been shown that for 1 and 2 dimensional infinite scattering systems, localisation of states is guaranteed, yet in 3 dimensions there exists a phase transition at a given degree of randomisation in which the extended states become localised. This phenomenon is termed the scaling theory of localisation and defines the dimensionless parameter, g, the conductance of the material. The theory was developed from the works of Edwards and Thouless (43), from whom it takes its name.

The key comparison used to determine whether a wave becomes localised in a system with a given number of dimensions is the scale of the localisation length, ξ, relative to the system size. In a 1 dimensional system the localisation length scales as the mean free path and in a 2 dimensional system the localisation length scales with its exponent

(44). In a three dimensional system, a critical point exists where a transition is expected from the largely extended to the localised regime.

There are several factors which make producing strong localisation in three dimensional photonic materials exceedingly difficult. One of the difficulties that has been identified when trying to produce strong localisation effects in 3D photonic materials is the near field interaction between scattering particles. The high field amplitudes in the space around the particles can cause losses through coupling between dipoles excited in the particles(45), as well as through evanescent waves (46). The strong inelastic interactions between scatterers contributes positively to the diffusion without enabling interference, thus counteracting the localisation effect. In their 2017 paper for example, Escalante and Skipetrov (47) discuss the effect of longitudinal EM waves which generally decay in the far field but which can cause significant coupling in the near field (47). They present theoretical works which indicate hollow or coated nanospheres may be more suitable for coherent multiple scattering, and subsequent experimental works provide interesting results (48).

Further to this there is another complication, the likelihood of forming a "closed loop" is strongly dependant upon the number of degrees of freedom of the wave. In a three dimensional system there are a large number of possible paths (or channels) available, on top of this for electromagnetic waves polarisation plays a role, since light of opposing polarisations will not interfere. This extra degree of freedom due to the vector-like nature of light makes observation of localisation in three dimensions increasingly unlikely (49). An exciting development however is the discovery of anomalous light transport in a strongly scattering titania sample by Cobus et al. (50). As previously stated, titania samples are susceptible to fluorescence and absorption in long time trail experiments, however these findings were made in very short ($\sim ps$) timescales.

Another of the identified experimental constraints is the low effective refractive index of scatterers in current strongly scattering materials. This is where it is hoped that Mie resonances in dielectric materials could lead to a breakthrough (51). Fluorescence is a significant inhibitor to localisation, since it detracts from the scattering of the waves, and can give indicators due to an apparent delay of the transmission and reduction of the beamwidth, similar to the expected hallmarks of localisation. These complications and others have led researchers to question the feasibility of observing 3D localisation in photonic networks (49)(52). In spite of this, theoretical works continue to probe the localisation limit in three dimensional photonic systems (53) (54) (29) (8).

In the 2004 book 'Mesoscopic physics of electrons and photons', Akkermans and Montambaux (32) present a detailed theoretical analysis of the diffusion of light and electrons in the multiply scattering regime, incorporating experimental results into their discussion, and highlighting the significant contributions to the theoretical works. They describe the limitation of the diffuse scattering model in the high confinement regime

and present mathematical descriptions of the quantum effects which can arise in such cases.

Coherent light which is transmitted through such a material produces a far-field speckle pattern; a two dimensional interference pattern at a distance far from the exit plane which is a result of the constructive and deconstructive interference over the many light paths. The difference in phase due to the variation in length of the many light paths, as well as the randomisation of the direction of exit causes a variation in the intensity of the speckle at a distance away from the exit surface. This variation can be described statistically and is not apparent in the classical diffuse model of light transport because the speckle pattern is a coherent effect and the standard diffusion model does not deal explicitly with the phase of the wave.

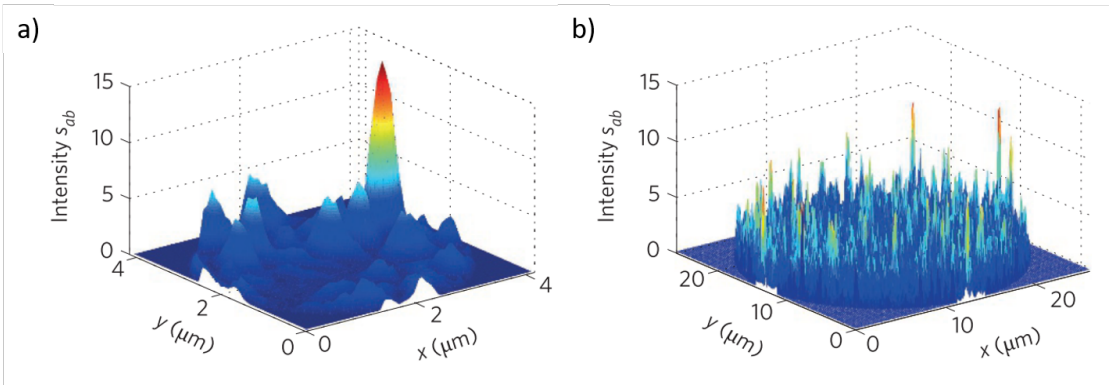

FIGURE 2.2: Speckle pattern produced in a disordered medium when illuminated with coherent light. The variation in spatial intensity is due to interference from multiple light paths. The speckle pattern is shown both for an in focus (a) and out of focus (b) illumination which shows how the number of illuminated channels affects the speckle variation. Figure reproduced from reference (11).

An important concept in this theory is that of a quantum crossing, a point in space where two paths overlap. This leads to a complex amplitude contribution to the total intensity of the transmitted light. When considering a multiply scattering medium there are long range contributions in which one or more quantum crossings among multiple paths in the material can give rise to correlations in the speckle pattern. The likelihood of these crossings occurring is inversely proportional to the conductance, $1/g^n$ where g is the dimensionless quantity equivalent to the conductance of a material, and n is the number of crossings. These correlations can be measured using transmission spectroscopy and thus determine the scattering strength of the material.

2.2.4 Diffusion Through a Finite Slab

When applying the diffusion equation to a slab of finite thickness and size we must introduce boundary conditions to incorporate the edges of the medium into the mathematical description. For the thickness of the sample we shall consider the air-scattering medium interface to occur at a position $z = 0$. For a sample of thickness L the back surface of the medium is then positioned at $z = L$.

For a sufficiently scattering material with a relatively large mismatch of the refractive index of the scattering medium to the surrounding, internal reflections at the front and back surface of the sample become non-negligible and thus reflection at the boundary becomes subject to imposed boundary conditions. If we present the example of a coherent source being incident on the front face of the sample at $z = 0$, we can imagine that a given scattering path inside the sample may eventually return to the front surface after a number of scattering events. This path may then be reflected back into the sample due to total internal reflection, and the same is true for paths reaching the end face. This can be accounted for by considering an extrapolation length, $z_{e_{1,2}}$. The extrapolation length can be considered a plane outside the sample at a position $z = -z_{e1}$ and $z = L + z_{e2}$ at the front and back of the slab respectively where the intensity produced from this diffuse source is zero, constraining the diffusion equation to Dirichlet boundary conditions. Light which is incident on the sample is assumed to be a coherent source that upon entering the sample converts from ballistic propagation to diffusive propagation over a series of scattering events. There is therefore a source of diffusive intensity which is described as a negative exponential of the diffusive source injection depth, z_p, which scales as the mean free path of the sample. In most treatments the injection depth and the extrapolation lengths are assumed to be equal.

The extrapolation length z_e can be calculated from the reflectivity of the slab at each interface as follows (55):

$$z_{e_{1,2}} = \frac{2l_t}{3}\left(\frac{1 + R_{1,2}}{1 - R_{1,2}}\right) \tag{2.3}$$

Where R is the averaged reflectivity at the boundary for all angles and polarisations, which can be calculated using the Fresnel equations. In the case of a scattering layer in contact with a substrate of higher refractive index, we can define two boundaries, the boundary between the scattering layer and the substrate, ab, and that between the substrate and the surrounding medium, bc, in most cases this medium will be air. The total reflectivity at the rear interface is then found using the equation (56)

$$R(\theta) = R_{ab}(\theta_1) + \frac{T_{ab}(\theta_1)R_{bc}(\theta_2)R_{ba}(\theta_2)e^{-2\alpha h/cos(\theta_2)}}{1 - R_{bc}(\theta_2)R_{ba}(\theta_2)e^{-2\alpha h/cos(\theta_2)}} \tag{2.4}$$

where θ_1 is the angle of incidence from the scattering layer a to the normal of the boundary, and θ_2 is the angle of a refracted light ray travelling in the substrate b. The absorption coefficient of the substrate and the substrate thickness are given by α and h, and $T(\theta)$, $R(\theta)$ represent the transmitted and reflected light at each boundary respectively.

Absorption length in the diffusing medium can be represented in two ways, either in terms of the average distance light propagates along its path before its intensity is reduced by a factor e, l_a, or the average depth into the material which a diffusive source propagates before its intensity is reduced by a factor e, L_a. The two are related via the transport length as (57)

$$L_a = \sqrt{\frac{l_a l_t}{3}}. \tag{2.5}$$

In the static case, the total transmission of the sample is given by (58)

$$T_d = \frac{1}{l_t}\int_0^L T_d(z_p)\exp\Big(-\frac{z_p}{l_t}\Big)dz_p, \tag{2.6}$$

where

$$\begin{aligned} T_d(z_p) = &\frac{\frac{L_a}{l_t - L_a}[\exp(\frac{L}{L_a} - \frac{L}{z_p}) - 1][1 + \frac{z_{e_1}}{L_a}]}{2(1 + \frac{z_{e_1} z_{e_2}}{L_a^2})\sinh(\frac{L}{L_a}) + 4(L_a^{-1})z_{e_1}\cosh(\frac{L}{L_a})} \\ &+ \frac{\frac{L_a}{z_p + L_a}[\exp(-\frac{L}{L_a} - \frac{L}{z_p}) - 1][1 - \frac{z_{e_1}}{L_a}]}{2(1 + \frac{z_{e_1} z_{e_2}}{L_a^2})\sinh(\frac{L}{L_a}) + 4(L_a^{-1})z_{e_1}\cosh(\frac{L}{L_a})}, \end{aligned} \tag{2.7}$$

and the total reflection is given by

$$R_d = \frac{1}{l_t}\int_0^L R_d(z_p)\exp\Big(-\frac{z_p}{l_t}\Big)dz_p, \tag{2.8}$$

where

$$\begin{aligned} R_d(z_p) = &\frac{\frac{L_a \exp(-L/L_a)}{1 + L_a}[\exp(-\frac{L}{L_a} - \frac{L}{z_p}) - 1][1 + \frac{z_{e_1}}{L_a}]}{2(1 + \frac{z_{e_1} z_{e_1}}{L_a^2})\sinh(\frac{L}{L_a}) + 4(L_a^{-1})z_{e_2}\cosh(\frac{L}{L_a})} \\ &+ \frac{\frac{L_a}{z_p + L_a}[\exp(\frac{L}{L_a} - \frac{L}{z_p}) - 1][1 - \frac{z_{e_1}}{L_a}]}{2(1 + \frac{z_{e_1} z_{e_2}}{L_a^2})\sinh(\frac{L}{L_a}) + 4(L_a^{-1})z_{e_2}\cosh(\frac{L}{L_a})}. \end{aligned} \tag{2.9}$$

These equations simplify in the case of a thick absorbing sample ($L \gg L_a$) to give the exponential decays (59)

$$T_d = \frac{2L_a(l_t + z_{e_1})}{L_a^2 + L_a(z_{e_1} + z_{e_2}) + z_{e_1}z_{e_2}} \exp\Big(-\frac{L}{L_a}\Big), \tag{2.10}$$

and

$$R_d = \frac{L_a(L_a + z_{e_1})}{L_a^2 + (z_{e_1} + L_a z_{e_2}) + z_{e_1}z_{e_2}} \exp\Big(-\frac{z_p}{L_a}\Big). \tag{2.11}$$

Thus by measuring the thickness and total transmission of the sample and calculating the extrapolation lengths from the angular and polarisation averaged Fresnel equations for reflectivity at an interface, it is possible to calculate the absorption length L_a inside the sample for a given effective refractive index, approximated using a relative fill fraction of the nanowires. From this value, a corresponding total reflectivity can be calculated from a fixed injection depth z_p and compared.

The solution of these equations to obtain L_a is non-trivial, therefore when it comes to solving for L_a we shall do so numerically.

2.2.5 Anisotropic Scattering and Time Dependent Diffusion Equation

Anisotropic scattering where energy is preferentially scattered into transverse modes of transport has been shown to be advantageous for Anderson localisation of light, and in extreme limits could create quasi-one or two dimensional materials, thus increasing the return probability (60). It is therefore pertinent to ensure an accurate depiction of the mathematics of anisotropic scattering. The diffusion constant, **D**, energy transport velocity, $\mathbf{v}_e$, and transport mean free path, $\mathbf{l}_t$, creating a codependency which is difficult to disentangle using macroscopic measurements alone.

Anisotropy can be introduced through the structuring of random materials or through direction dependent scattering of single scatterers. Since the transport mean free path, l_t, is related to the scattering mean free path, l as:

$$l_t = \frac{l}{1-g} \tag{2.12}$$

where the asymmetry coefficient, $g = \langle cos(\theta) \rangle$, describes the average deviation in direction of propagation (expressed in terms of the angle, θ) expected from a single scattering event. It then becomes clear that the value of g becomes a vector in the case

of a material where the scattering strength is dependent on the direction of incidence. Therefore a significant determination must be made whether to assume the asymmetrical scattering coefficient is constant irrespective of the direction of transport, and therefore that the transport mean free path is not direction dependent. In the case of the samples studied and the measurements presented in this work, it is logical to reduce the transport mean free path vector to a single scalar quantity, assuming that the coherent backscatter measurements taken give an average of the transport mean free path in all directions, and certainly along the perpendicular component, $\hat{r}$, due to rotational averaging of the cone, $l_t = \overline{\mathbf{l}_t}$. This then leaves the diffusion constant, $\mathbf{D}$, as a vector quantity, which will incorporate any significant difference in the scattering asymmetry of the individual scatterers of the system, as well as any structural asymmetry of the system itself.

When considering the time resolved transmission, the effect of absorption is introduced via an exponential decay with characteristic decay constant τ_a, the absorption time. The absorption time can be calculated from the absorption length L_a as

$$\tau_a = \frac{3L_a^2}{2D_r + D_z} \tag{2.13}$$

This is found using the relations

$$L_a = \frac{l_t}{\sqrt{3(1-a)}} \tag{2.14}$$

$$\tau_a = \frac{l_t}{v_E(1-a)} \tag{2.15}$$

where

$$v_E = \frac{2D_r + D_z}{l_t} \tag{2.16}$$

is the energy transport velocity of the material, and

$$a = \frac{\sigma_{sca}}{\sigma_{ext}} \tag{2.17}$$

is the albedo, a ratio of the scattering and extinction coefficients of the single scattering interaction, which does not appear in equation 2.13 and thus does not need to be explicitly calculated in order to obtain τ_a.

The energy velocity, v_E, calculated in equation 2.16 is a calculated as a function of the diffusion over three degrees of freedom, both the forward and perpendicular directions. When considering a purely isotropic diffusing medium, the rate of diffusion in all three dimensions would intuitively be constant i.e. $D_z = D_x = D_y$. However if we wish to examine an anisotropic sample where D_z and D_r may take on different values we must incorporate this into the diffusion model.

By incorporating the extrapolation length into the time and space dependent transmission obtained from the diffusion equation, a full equation of the transmission at the back surface of the sample can be obtained according to diffusion theory

$$\begin{aligned} T(x,y,t) =& \frac{S_0}{16\pi^{\frac{3}{2}} t^{\frac{5}{2}} \sqrt{D_z D_r^2}} exp\left(-\frac{r^2}{4D_r t}\right) exp\left(-\frac{(2D_r + D_z)t}{3L_a^2}\right) \\ & \times \sum_{m=-\infty}^{\infty} \left[A'(m) exp\left(-\frac{A'(m)^2}{4D_z t}\right) - B'(m) exp\left(-\frac{B'(m)^2}{4D_z t}\right)\right] \end{aligned} \tag{2.18}$$

where $A'(m) \equiv (2m+1)(L+2z_e) - l_t 2z_e$ and $B'(m) \equiv (2m+1)(L+2z_e) + l_t$.

This is of the form given in reference (61). Previous studies have used this relation to explore diffusion using interferometric experiments, measuring photonic glasses (62), liquid crystals (61), PTFE and paper (63), titania nanoparticles (64) as well as microporous (65) and particulate (59) gallium phosphide. These measurements provide a comprehensive basis for the interpretation of such measurements.

2.3 Speckle Correlation and the Optical Memory Effect

2.3.1 Correlations in Wave Propagation

The Optical Memory Effect (OME) finds its theoretical foundations in mesoscopic electronic conductance fluctuation and experiments of the 1980's. It was found that the fluctuations observed in the conductance through a material due to mesoscopic interference of the coherent electron in the randomly scattering environments of materials could be generalised to other wave-like phenomena, such as light or sound, in similarly random scattering environments. The deviations in the electronic potential of conducting materials present a scattering medium which enables the crossing of transmission channels which, with the scalar nature of the electron wavefunction, causes them to interfere as they traverse the sample. This can be compared to coherent light which is transmitted through a sample consisting of a number of scattering centres dispersed throughout the medium. The caveats to this are that the sample must be thick enough that the light undergoes multiple scattering ($L, W >> l_t$ where L is the sample length in the direction of propagation, W is the sample width/cross-section, and l_t is the transport mean free path).

When observing the intensity of light in the far field produced by coherent light transmission (or reflection) from a scattering sample, the interference of multiple contributing paths of light within the sample leads to an angular distribution of intensities called a speckle pattern. The contributions from multiple paths inside the sample would usually average out to a randomisation of the phase and thus have no significant contribution to the outputted intensity when averaged over many realisations of the sample,

$\langle I \rangle$. This would result in a retrieval of the diffuse intensity distribution following a Lambertian envelope in the expected intensity.

However, as mentioned in Section 2.1, when undergoing multiple scattering, it is possible for light which is incident on the sample from separate positions on the surface, or angles, to explore the same regions of the sample. This contributes to a correlation in the outputted amplitude of the transmitted (or reflected) signal, in the same way as the crossing of channels in the exploration of the electronic wavefunction in the conductance experiments. When these paths cross and the phases are no longer completely uncorrelated with one another, the contribution to the intensity becomes correlated over many realisations of the speckle. The same is true for optical paths which are symmetric under time reversal, since they inherently explore the same regions of the sample.

This description explains the physical phenomenon that when a small deviation of the angle of incidence is introduced, the outgoing correlated signal is also shifted by a comparable slight change in angle. These contributions to the speckle pattern, which seem to retain information from before interacting with the sample, are hence described as the optical memory effect.

$$C = C^{(1)} + C^{(2)} + C^{(3)}. \tag{2.19}$$

These represent the short range, long range, and universal correlations respectively. an illustration of these contributions are shown in Figure 2.3.

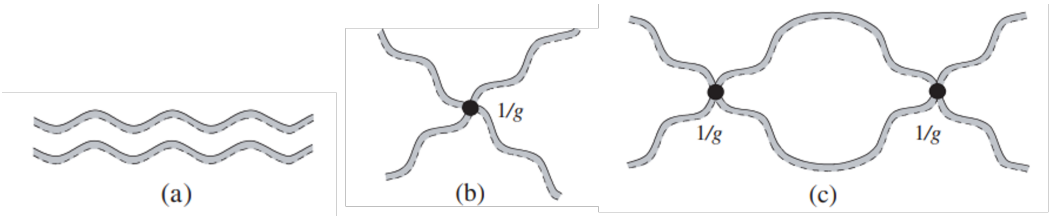

FIGURE 2.3: Three contributions of short range $C^{(1)}$ (a), long range $C^{(2)}$ (b), and universal $C^{(3)}$ (c) to the correlation function. g refers to the mesoscopic conductance factor. Figure reproduced from Akkermans and Montambaux (66).

The discovery of the optical memory effect led to significant progress in signal imaging in disordered scattering environments, as produced by fog and clouds, or in medical applications such as in biological tissues.

2.3.2 The Time Reverse Optical Memory Effect

The contribution of the crossed paths to the speckle correlation are described as the $\mathbf{C}^{(1)}$, $\mathbf{C}^{(2)}$, and $\mathbf{C}^{(3)}$ correlation functions. This was put forward by Feng et al. (67)

and further expanded by Berkovits and Kaveh (68) to include the contribution from time reverse paths. The distribution of the correlation as a function of the angle of separation, θ (or by direct comparison the transverse component of the wave vector, Δq) from the incident and outgoing beams is given by the sum of these contributions. Experimental verification of the $C^{(1)}$ correlation in laser speckle was first demonstrated by Freund et al. (9) in transmission and reflection.

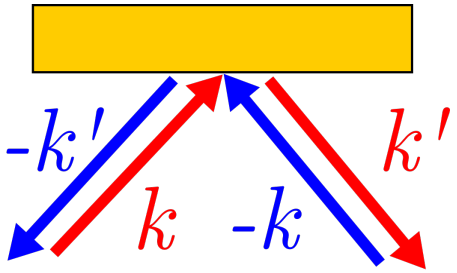

FIGURE 2.4: An illustration of the time reversal geometry showing Lorentz reciprocal paths, k, k' and $-k$, $-k'$.

In Figure 2.4, an illustration of the time reverse geometry for reflection is shown with two incoming wave vectors, k and $-k$. The two outgoing wave vectors are k' and $-k'$.

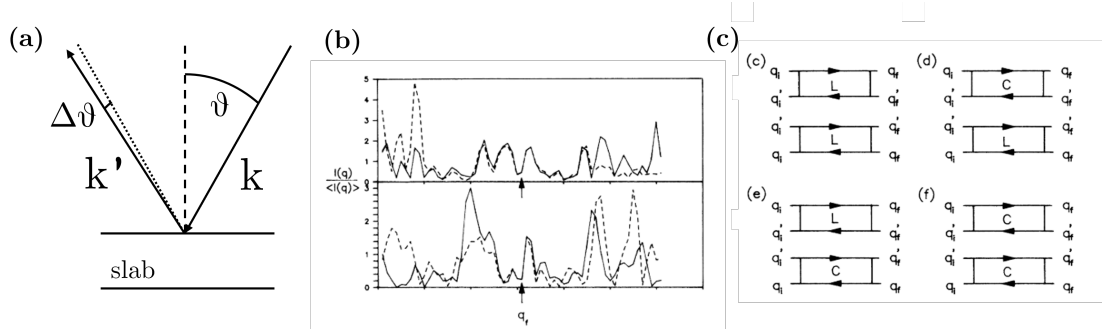

FIGURE 2.5: An illustration of the reflection geometry is shown in (a), showing that the angle of incidence or reflection, θ, is defined relative to the normal of the surface of the slab. An example of correlation in the speckle intensity is shown in (b) for reflection (upper) and transmission (lower). Maximum correlation is centred around the region where the incident and reflected light follow time reversed paths ($q = -q'$). Feynman diagrams for the four contributions to the intensity correlation in the time reverse geometry are illustrated in (c). (b) and (c), reproduced from reference (68)

When undergoing a change in the angle of incidence, the change in the transverse wave vector, Δq is found trigonometrically to be

$$\begin{aligned} \Delta q &= k sin(\Delta\theta) \\ k &= \frac{2\pi}{\lambda} \end{aligned} \tag{2.20}$$

In the reflection geometry the correlation between the speckles takes the form

$$C^{(1)R}_{aba'b'} = \delta_{\Delta q_a \Delta q_b} \frac{[F_R^{(1)}(\Delta q_a) + F_R^{(1)}(q_a + q_b + \Delta q_a)]^2}{[1 + F_R^{(1)}(q_a + q_b)][1 + F_R^{(1)}(q_a + q_b - 2\Delta q_a)]}, \tag{2.21}$$

where $F_R^{(1)}$ is of the form

$$F_R^{(1)}(q) = \frac{L \sinh(q(L - l_t)) \sinh(q l_t)}{(L - l_t) q l_t \sinh(qL)}. \tag{2.22}$$

First order dependence of the correlation of the speckle as a function of the transverse spatial displacement of the wavefront relative to the sample is given by (69)

$$C^{(1)}(\Delta r) = \left(\frac{\sin(k\Delta r)}{k\Delta r} \right)^2 \exp(-\Delta r / l_s). \tag{2.23}$$

This short range contribution is the dominant factor when considering weak scatterers, as the $C^{(2)}$ and $C^{(3)}$ contributions fall off, as before, as $1/g$ and $1/g^2$ respectively. (70)

This relation presents two peaks in the correlation, one where Δq is zero, i.e. where the direction of incidence and reflection are the same and $q_a = q'_a$. The second is the time reverse geometry which centres around $\Delta q_a = q_a + q_b$, where $q_a = -q'_b$ and vice versa. The correlation of the time reverse optical memory was shown in 1991 (71). The practical applications of this phenomenon are many, the detection of a reflective object through a thin multiply scattering obstruction is a common problem in a number of fields. The use of amplitude, phase, and frequency modulation of coherent sources to generate correlated signals has been described (72), and further innovations have led to significant advancements (73)(74)(75).

2.3.3 Speckle Generation and Rayleigh Statistics

The fundamental role of phase in the generation of spatial speckle patterns raises the possibility of controlling this property to alter the intensity distribution. This has been used experimentally in optical wavefront shaping to produce focusing through multiple scattering media (76)(77). In a time reversible reflection geometry, the spatial correlation between speckles is due to the angular distribution of field amplitudes. The field amplitude in a speckle spot, **A**, is given by

$$\mathbf{A} = \sum_{i=1}^{N} \mathbf{a}_i, \tag{2.24}$$

where

$$\mathbf{a}_i = ae^{i\phi_i} \tag{2.25}$$

is the field produced by a single transmission channel between an input and the speckle position, a being the absolute amplitude of the field and ϕ_i the phase for light travelling along a specific path i. N is then the number of channels. These contributions are vectors due to their wave vector polarisation.

In a sufficiently random medium, the average of the field amplitude at the exit surface of the sample is zero, since the phase is completely randomised. This arises an assumption that there is a sufficiently large number of open transmission channels of varying path lengths, leading to a randomisation of the complex value of the amplitude at the output.

$$\langle \mathbf{a}_i \rangle = 0 \tag{2.26}$$

The contribution to the intensity from two possible channels is then given as the product of the complex amplitude of one channel and the complex conjugate of the second channel

$$\mathbf{a}_j \mathbf{a}_j^* = a_i a_j \delta_{ij} \tag{2.27}$$

giving a scalar contribution under the condition $\delta_{i,j}$, i.e. where the phase difference between the two paths is zero. This means that the average intensity obtained for a complete speckle pattern is given as

$$\langle I \rangle = \sum_{i,j}^{N} \mathbf{a}_i \mathbf{a}_j^* = Na^2, \tag{2.28}$$

when all possible paths are taken into account.

If we examine the expected value of the square of the intensity $\langle I^2 \rangle$ we obtain:

$$\langle I^2 \rangle = \left\langle \sum_{i,j,k,l}^{N} \mathbf{a}_i \mathbf{a}_j^* \mathbf{a}_k \mathbf{a}_l^* \right\rangle = \sum_{i,k}^{N} a^4 (\delta_{i,j}\delta_{k,l} + \delta_{i,l}\delta_{j,k}) = 2N^2 a^4 \tag{2.29}$$

This means that the variance of the fluctuations in the intensity distribution, $\sigma_I^2 = \Delta I^2$ of the speckle can be shown to be

$$\Delta I^2 = \langle I^2 \rangle - \langle I \rangle^2 = 2N^2 a^4 - (Na^2)^2 = Na^2 = \langle I \rangle^2 \tag{2.30}$$

for a speckle pattern which exhibits a statistical Rayleigh distribution of intensity. The Rayleigh distribution of intensities can be shown to exhibit a negative exponential dependence where the mean is equal to the standard deviation:

$$P(I) = \frac{1}{\langle I \rangle} e^{\frac{I}{\langle I \rangle}} \tag{2.31}$$

The effect of polarisation dependence is an important factor when determining the statistical representation of the speckle if there is significant depolarisation upon scattering and if there is polarisation dependence in the detection (78).

Chapter 3

Static Optical Characterisation of Strongly Scattering Disordered Media

3.1 Introduction

In this Section a number of established experimental techniques are used to characterise the properties of the samples used in the optical pump probe experiments. These parameters are required to give an accurate calculation of the scattering properties measured in chapter 4.

The experiments include total transmission and reflection measurements, to determine the absorption properties of the samples, and coherent backscatter spectroscopy (CBS), thus determining the transport mean free path. The absorption of GaP nanowires has been measured before using nanowire samples of various lengths, showing an expected fall in the transmission. These experiments then look to corroborate these measurements and provide an exact value for the samples to be measured in this thesis. The same is true for the CBS measurements, the transport mean free path determined in these experiments should agree with previous experiments, which showed very strong scattering in the nanowire mats.

The experiments are also performed on two depositions of mono-disperse strongly scattering Titania nanospheres, in order to validate the results. Experimental methodologies are presented, followed by the characterisation of the Titania nanospheres and then the gallium phosphide nanowires.

3.2 Experimental Methodologies

3.2.1 Total Transmission and Reflection Experimental Set Up

The total transmission and reflection measurements are achieved using a broadband supercontinuum pulsed laser source. This produces a coherent source of light over a wavelength range of 400 nm to 1750 nm. The light is focused through a plano-convex lens of focal length 100 *mm* onto the sample at an angle of approximately 8 degrees to the normal of the surface. The angle of incidence is chosen such that in the reflection geometry, the specular reflection is captured within the sphere. taking the beam width at the lens to be 5 mm, the numerical aperture of the lens is found to be approximately 0.03, making the acceptance angle at the surface of the sample 3.4 degrees. Since $\cos(8+3.4) \approx 0.98$ it is safe to calculate the extrapolation lengths as though the angle of incidence were normal to the surface. The spot size and focal length of the beam at the surface of the sample is also subject to chromatic dispersion across the visible and near-infrared. The size of the spot is largely irrelevant in measuring the total transmission, given that the spot size is large enough to average over a number of transmission channels, thus averaging any spectral speckle. The variation in the focal length of the lens due to the chromatic dispersion of the lens is small enough that it does not significantly impact the angle of incidence of the light onto the sample.

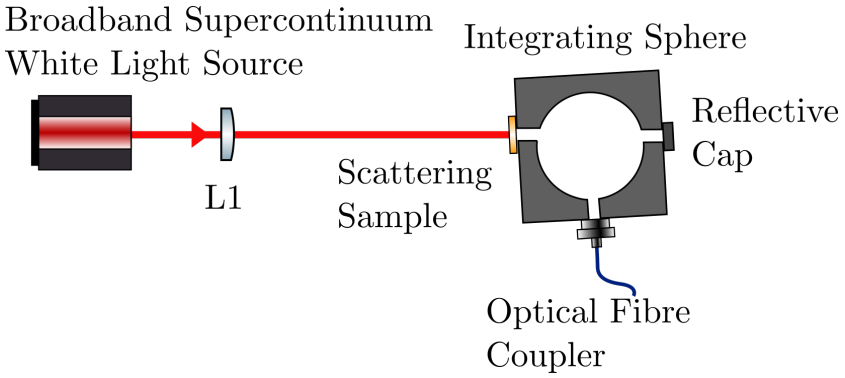

FIGURE 3.1: Experimental set up for measuring the total transmission. A coherent white light laser source is focused onto the surface of the sample using a 10cm focal length convex lens. The transmitted light is then collected using an integrating sphere. An optical fibre collects the scattered light from the integrating sphere and this is passed to a visible and an infrared spectrometer.

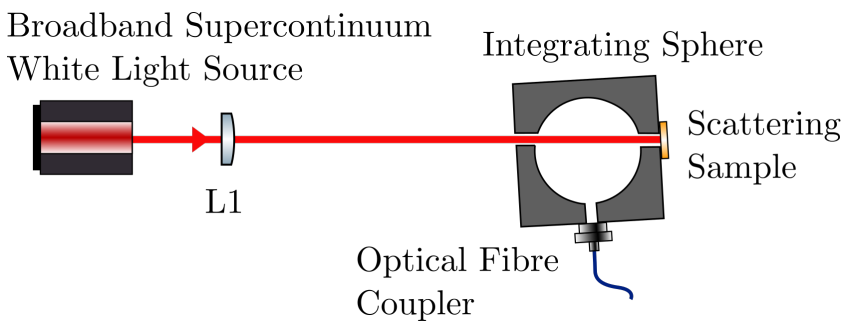

FIGURE 3.2: Experimental set up for measuring the total reflection. A coherent white light laser source is focused onto the surface of the sample using a 10cm focal length convex lens. The sample is placed at the rear aperture of an integrating sphere. The incident light is at an approximately 8 degree angle such that the specular reflection is incident on the internal surface of the integrating sphere. An optical fibre collects the scattered light from the integrating sphere and this is passed to a visible and an infrared spectrometer.

The transmitted and reflected light are collected using an integrating sphere as shown in figures 3.1 and 3.2. This is then split via a dual output multimode optical fiber to two spectrometers, an *Andor iDus* InGaAs infrared spectrometer and an *Andor iDus* CCD visible spectrometer. This allows simultaneous measurement of the visible and infrared transmission or reflection over a range from 400 nm to 1750 nm. A reference measurement is taken for both transmission and reflection measurements by closing the rear aperture of the sphere and measuring the total incident intensity from the laser without a sample in place. A dark measurement without illumination from the coherent white light source serves as a background, accounting for spectrometer noise and ambient light, which is subtracted from both sample and reference measurements.

3.2.2 Coherent Backscatter Spectroscopy Experimental Set Up

The coherent backscatter (CBS) spectroscopy experiment utilises the same *Fianium* broadband laser source and *Andor* spectrometers as the total transmission and reflection measurements. This allows for measurement of the CBS cone over the same wavelength range of ∼400 nm to ∼1750 nm. The high intensity coherent white light source is reflected by a glass slide beamsplitter onto the surface of the sample which is angled such that the specular beam reflection is directed away from the detector. The sample is placed on a rotating stage which radially averages the coherent backscatter and thus removes the speckle effect. The backscatter is measured using a multimode dual output optical fiber which is mounted on a rotating arm such that the point of illumination of the sample is on the central axis of rotation. An optical diffuser and linear polariser are used in the detection arm to improve signal capture by the optical fibre while reducing background. The optical diffuser was incorporated to remove an experimental artifact due to the focusing of the light into the multimode fiber, leading to unequal splitting of

the optical intensity between the visible and infra-red spectrometers. The experimental set-up is shown in Figure 3.3:

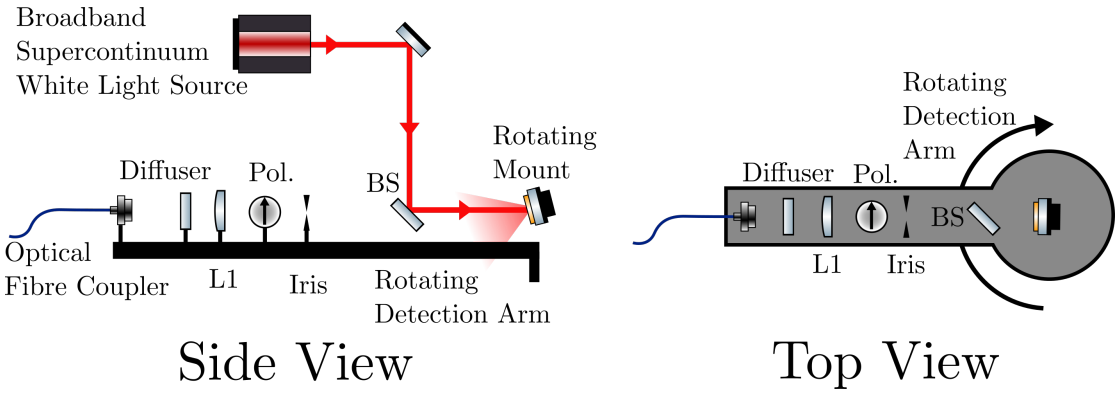

FIGURE 3.3: Coherent backscatter (CBS) spectroscopy experimental set up. Light from a pulsed Fianium supercontinuum white light source is directed onto the sample and the diffuse reflected visible and infrared light is measured across a wide range of angles using an optical fibre mounted on a rotating arm. An iris and polariser are used in the detection arm to eliminate sources of noise, and a $f = 1.5\,cm$ focal length plano-convex lens (L1) is used to focus the light into the multimode, dual output optical fibre coupler. A ground glass diffuser is used to optimise collection into the multimode fibre. The beam splitter and laser source are fixed in their angle of incidence to the sample.

Fringe-like behaviour is seen in the infra-red for the GaP nanowire samples. Several possible causes for this behaviour were investigated including Fabry-Perot type interference in the substrate of the sample, wavelength dependence of transmission and reflection of the beamsplitter or polarisers, or the reference sample used. All of these suggestions have been discounted, several different beamsplitters have been trialled and samples with a variety of substrate thicknesses have been measured. Using polarisation channels to differentiate the signal from the background or using various thicknesses of PTFE reference material also have no effect. The overall trend of the CBS spectrum reflects that expected from the total transmission and reflection measurements, it is therefor determined that the oscillations are an experimental artifact and are not representative of a true material property.

3.3 Titania Nanospheres

3.3.1 Total Transmission and Reflection

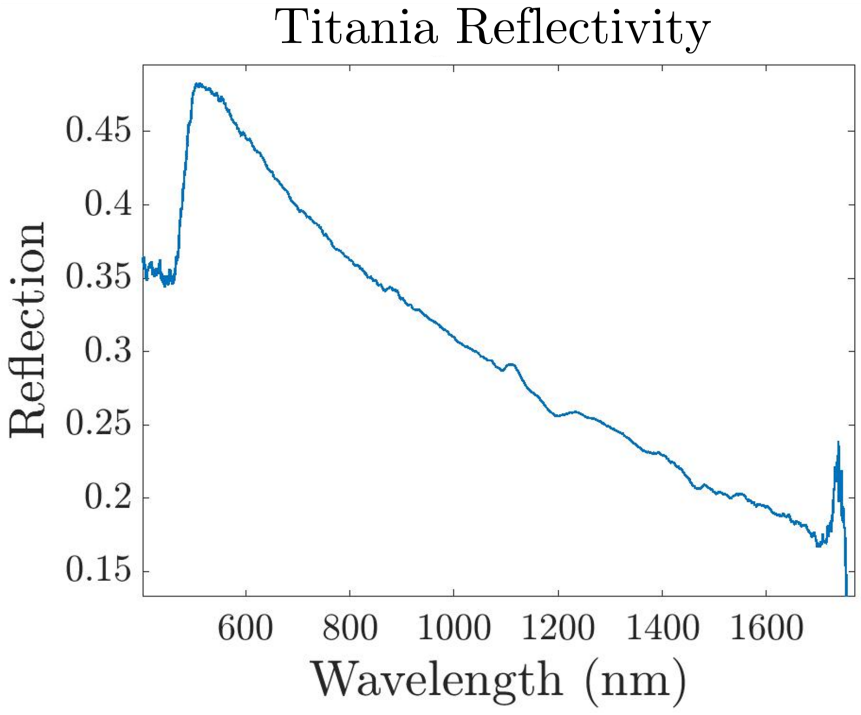

FIGURE 3.4: Reflectivity of a thin slab of mono-disperse 1 μm diameter TiO_2 nanospheres, of thickness L = 11 μm.

The total reflection measurement for a thin slab of the titania nanospheres is shown in Figure 3.4. The measurement shows a high reflectivity in the visible region, decreasing linearly towards the near infrared. This corroborates previous studies of titania nanoparticles (79), which are shown to be strongly scattering in the visible region.

3.3.2 Coherent Backscatter Spectroscopy

By measuring the coherent backscatter across a wide range of angles the transport mean free path can be determined following equation 2.2.

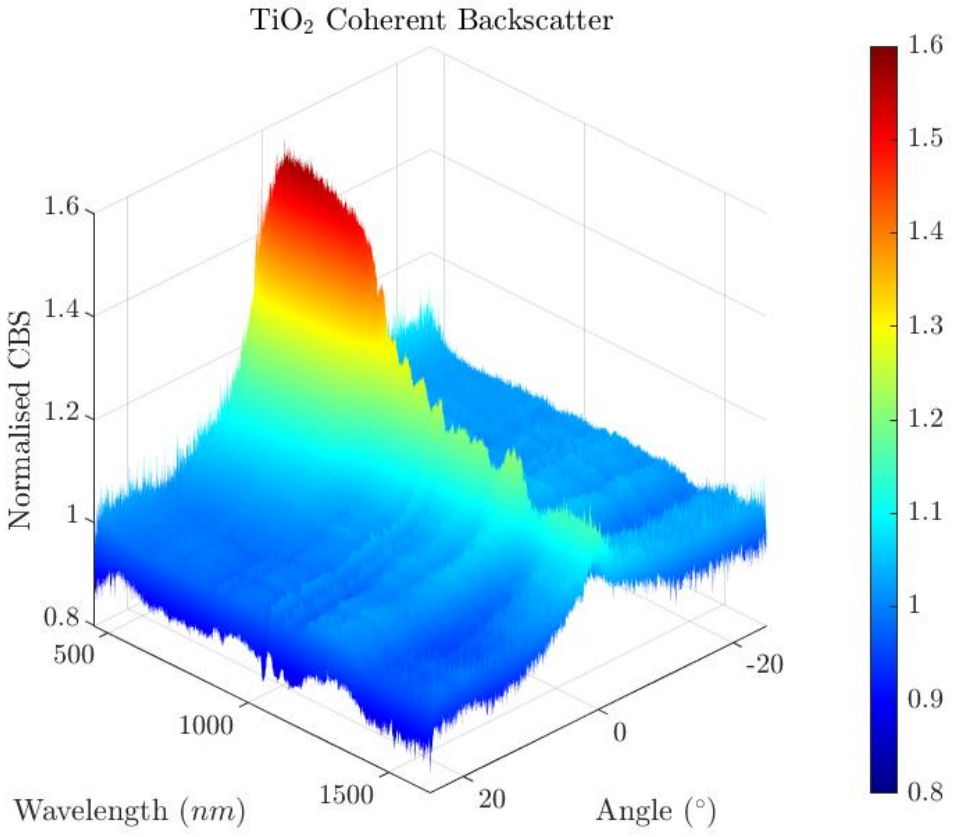

FIGURE 3.5: Titanium dioxide coherent backscatter (CBS) cone normalised to a PTFE reference sample. The enhancement factor is reduced by half due to the polariser eliminating half of all the time reversed paths which would contribute to the backscattering cone. The wavelengths have been plotted in reverse to more clearly show the profile of the cone as it extends to the near infrared. Colour bar indicates CBS con enhancement factor.

The CBS cone for a dropcast sample of titania nanospheres is given in Figure 3.5. In this figure the fringe like behaviour is visible in the infrared wavelengths. The plot has been reversed (moving from longer wavelengths in the foreground to shorter wavelengths) so that the fringe pattern can be seen more clearly. The enhancement factor also reaches a maximum of 1.5 in the visible region as is expected from our experimental constraints discussed in Section 3.2.2. The enhancement factor reduces steadily as the cone progresses into the infrared, likely due to the finite size of the sample. The sample thickness as measured is approximately 30 microns in thickness, however light of longer wavelengths are more likely to reach the rear surface of the sample, thus reducing the number of available longer light paths and thereby the enhancement factor.

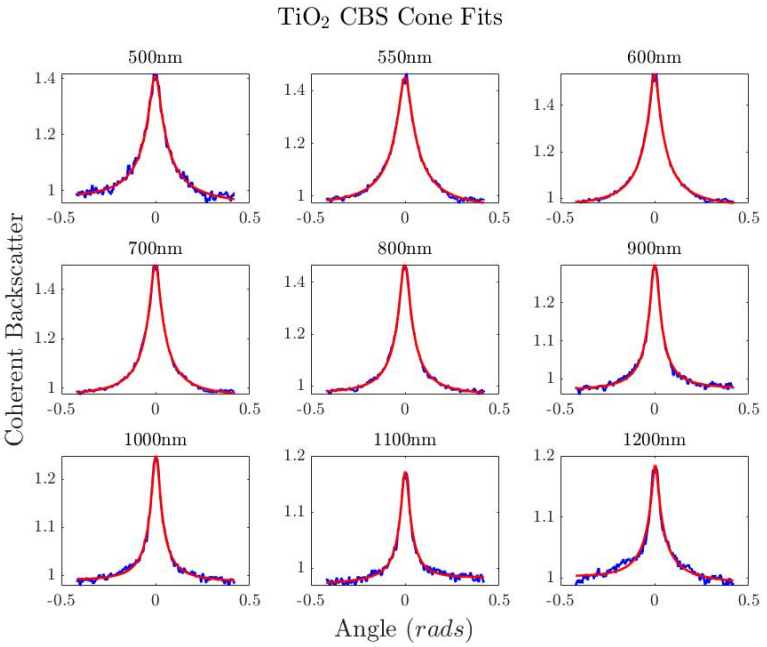

FIGURE 3.6: Plots of the fitting of titanium dioxide coherent backscatter (CBS) cone normalised to a PTFE reference sample for a dropcast of TiO_2 nanospheres. The plots show the theoretical fits of the experimentally obtained CBS cone over a range of wavelengths. Here the angle is given in radians.

An example set of CBS cone fits are given in Figure 3.6. The CBS cones are shown to reduce both in their width and relative height towards larger wavelengths.

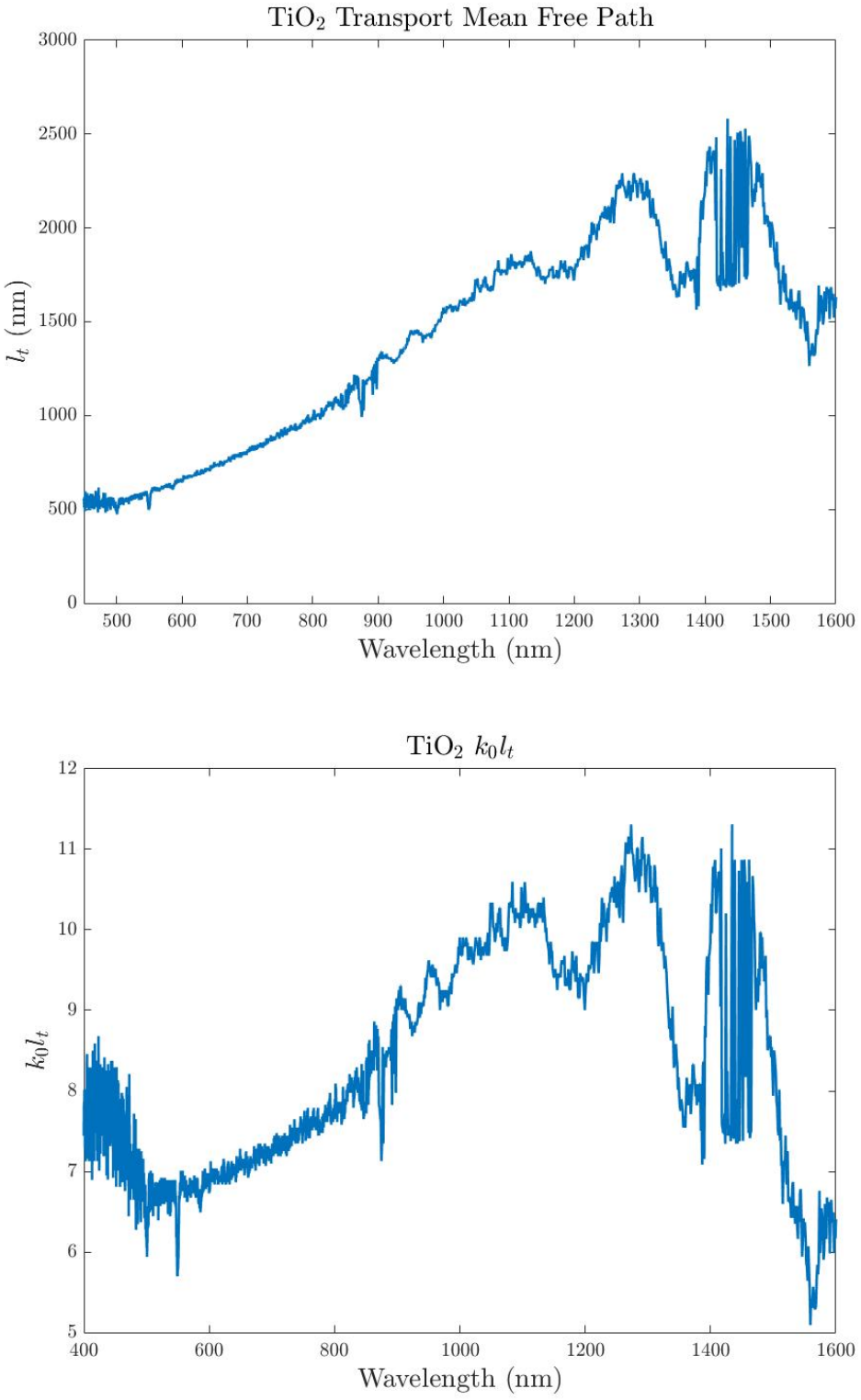

FIGURE 3.7: a) The wavelength dependence of the transport mean free path, l_t, for a dropcast of TiO_2 nanospheres calculated using the CBS measurement and b) the photonic strength denoted kl, the product of the transport mean free path l, and the wavenumber k.

In Figure 3.7, in particular the transport mean free path measurement, the resonant scattering from the titania particles becomes visible at longer wavelengths ($\lambda >\sim 1200\,nm$). At wavelengths shorter than this there is a power law dependence which is fitted in Figure 3.8. The fit to the transport mean free path in the range $450\,nm \leq \lambda \leq 1100\,nm$ follows the equation $l_t = 2.86 \times 10^{-5}(\lambda)^{2.54} + 331$. The value for the exponent matches other non-resonant multiply scattering materials (35) being in the range 2-2.5.

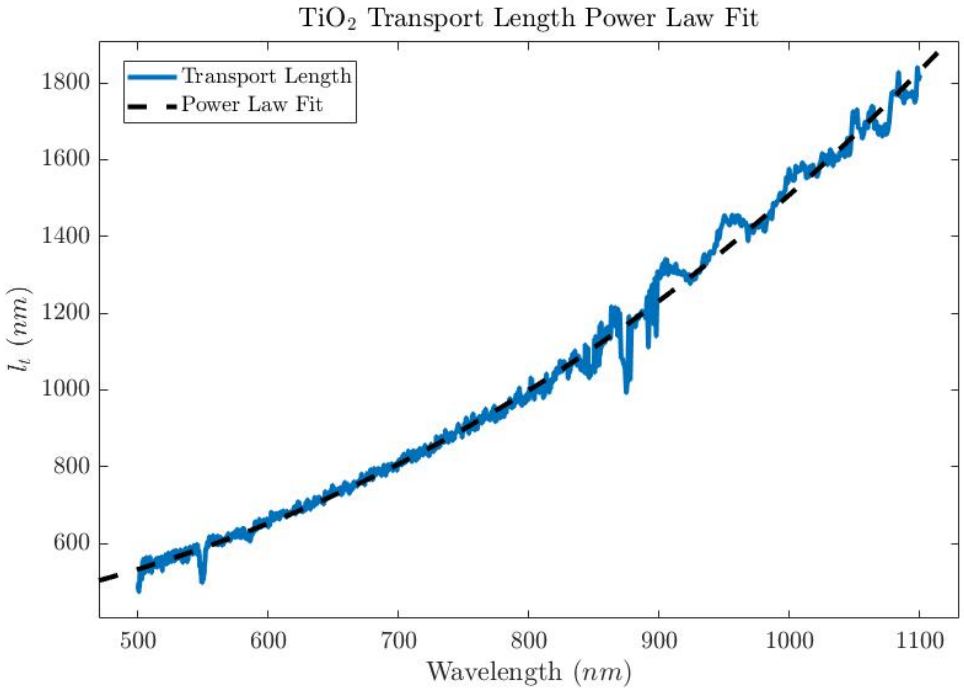

FIGURE 3.8: Power law fit of the mean free path obtained for titanium dioxide nanospheres from coherent backscatter (CBS) cone normalised to a PTFE reference. The plot shows the theoretical fit to the mean free path in the range before the fringe like behaviour becomes apparent at $\lambda >$1200 nm . The theoretical fit is a power law of the form $y = ax^b + c$ where $a = 2.86 \times 10^{-5}$, $b = 2.54$ and $c = 331$.

3.3.3 Dark Field Spectroscopy

Dark field spectroscopy allows for the measurement of the relative scattering strength of a sample, in the case of a single scatterer, giving a representation of the scattering cross-Section in a solid angle in the forward or backward scattering direction. This is achieved by detecting only the scattered light from a sample in a range of angles subtended by the detection apparatus, and rejecting light which is directly transmitted or reflected. In traditional microscopy, absorption of light or the scattering of light outside of the solid angle of detection results in a lowering of the intensity, giving rise to a bright field image. In this case, the opposite is true, whereby the directly transmitted light is blocked and the light scattered in the forwards direction is collected, thus giving intensity only where there is scattering. A diffuse light source can give an image of

the scatterers in the dark field and a coherent white light source can be used to give polarisation dependent spectroscopic measurements of the scattering strength.

This experiment does not lend itself to large slab-like geometries such as the GaP nanowires, since multiple scattering leads to a loss of the careful alignment required to obstruct the transmitted light. However, it can be used to probe the scattering profile of single nanoparticles, such as the titania nanospheres whose scattering cross Section can be modelled effectively using Mie theory. It is then possible to compare the scattering strength obtained through dark-field spectroscopy and the mean free path obtained through CBS spectroscopy.

The dark field spectroscopic measurement allows an indication of the relative strength of the forward scattering of single scatterers, integrated over a solid angle encompassed by the collection objective numerical aperture. In the case of this experiment, a 100x infrared microscope objective is used with focal length, $f = 2\,\text{mm}$ and numerical aperture, $NA = 0.5$.

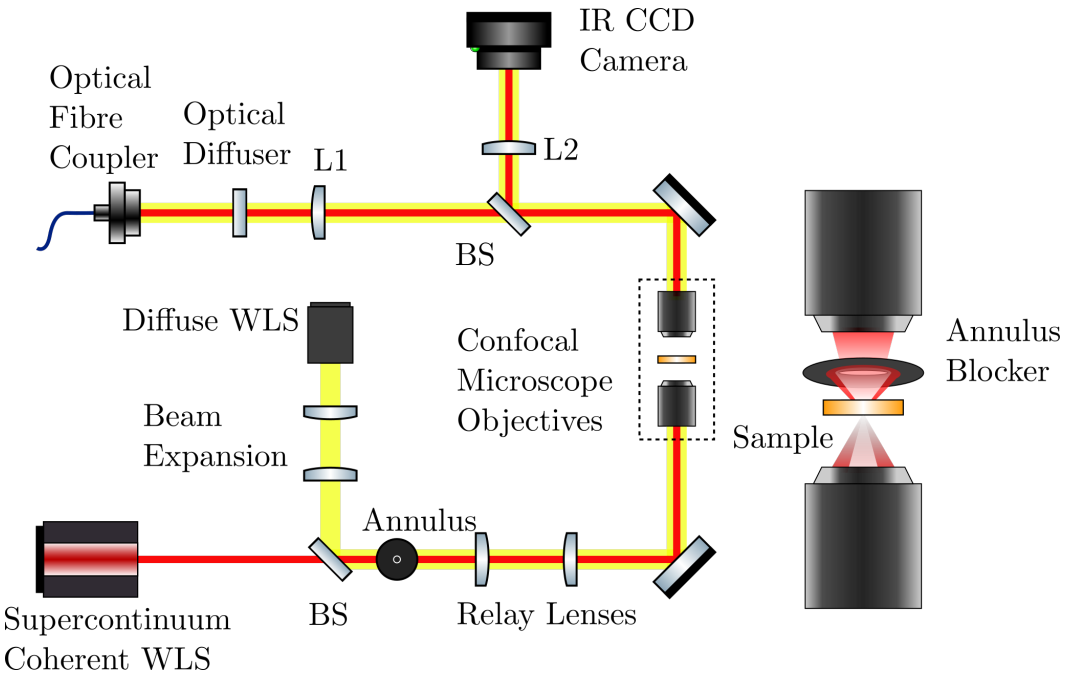

FIGURE 3.9: Simplified experimental diagram of the dark field spectroscopy measurement, showing the diffuse white light source (WLS), super-continuum laser source (*Fianium*), confocal objectives which direct light onto the sample and then collect the transmitted or reflected light. Images are then taken using an infrared camera and spectroscopic information is collected using a visible and an infrared spectrometer in the wavelength range of 450 nm to 1700 nm. Dark field images and forward scattering coefficients are measured by using a spatial filter to create an annulus of light which is focused onto the sample. The scattered light is then measured by blocking the ballistically transmitted light.

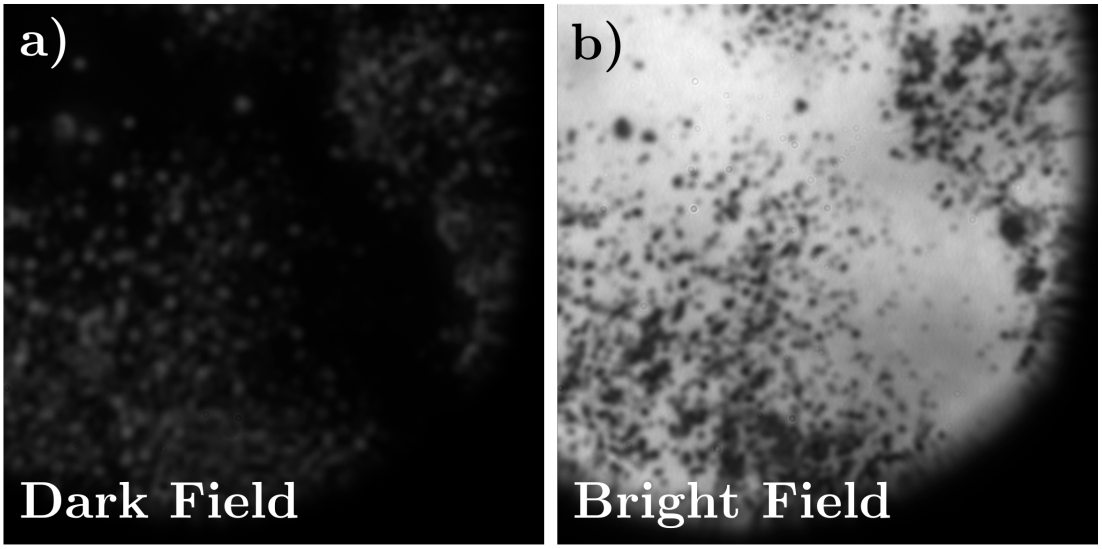

FIGURE 3.10: Bright (a) and dark (b) field image of the R900 TiO_2 nanoparticles taken using the dark-field spectroscopic apparatus using a diffuse white light source illumination. A reference scale is unavailable.

Using the diffuse white light source allows imaging of the sample to be measured and identification of single scatterers.

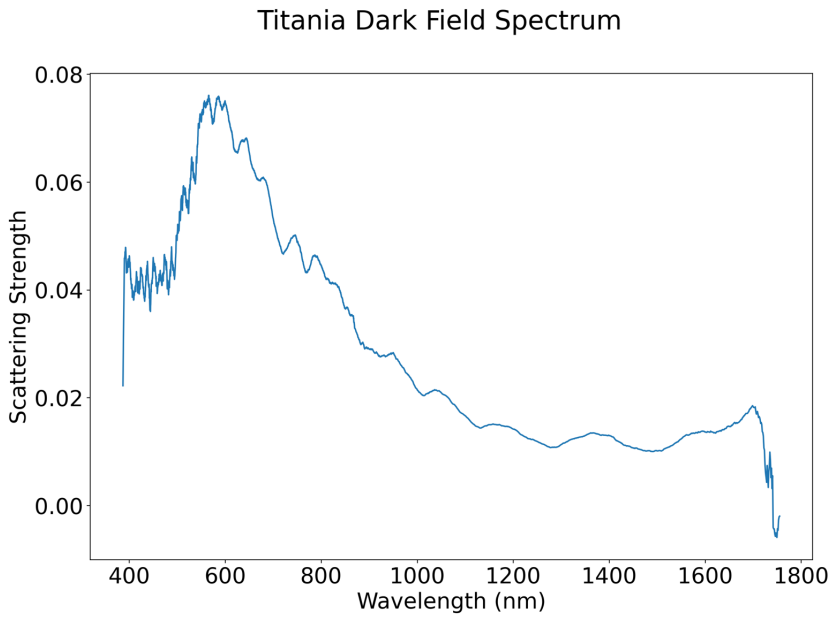

FIGURE 3.11: Spectroscopic measurement of the forward scattering strength of a single TiO_2 nanosphere of $\sim 1\,\mu$m diameter. detected forward scattering is integrated over the solid angle presented by an infrared microscope objective, NA 0.5. A similarity to the reflectivity and coherent backscattering characteristics of the bulk material is observed.

The spectral measurement gives an indication of the scattering cross-section of the individual particle to be measured. This scattering cross Section is in the forward direction and does not encompass the large scattering angles or backscatter. The scattering strength is shown to be highest in the visible region, decreasing towards the infrared. This is in line with what is expected following the coherent backscattering measurements, where the mean free path in the visible region is shown to be lower.

3.4 Gallium Phosphide Nanowires

The gallium phosphide nanowires measured in this thesis were grown using metal-organic vapour phase epitaxy several years ago, produced as part of a collaboration with the group of Professor Erik Bakkers of the University of Eindhoven. A large number of nanowire samples were developed of various lengths and diameters. Previous studies of the strongly scattering nanowires included total transmission and coherent backscatter spectroscopy, as well as spectral and spatial correlation statistics for characterisation of the scattering strengths of the materials. Dynamic measurements have shown that the nanowires induce an ultra-fast de-phasing response in the presence of high power optical pumping. This results in an optical switching like behaviour whereby wavefront shaping can be used to generate a focused intensity distribution in transmission through the nanowires, and a pump pulse may be used to destroy the constructive interference resulting in a defocusing of the intensity.

Previous experiments focused on the thinner nanowire mats which exhibited strong scattering in the visible and near infrared regions of the light spectrum. The following results explore the scattering produced by the thicker nanowire mats which were not studied in depth until now. The longer nanowires enable the detection of the longer time of flight light paths in the multiply scattered transmission, as seen in equation 2.18. Possible aging of the materials cannot be ruled out due to the lack of information regarding the oxidation of the nanowires, however current total transmission measurements show good agreement with those measured near to the time of fabrication.

3.4.1 SEM Imaging

Previously, scanning electron microscopy (SEM) images have been taken to determine the nanowire growth orientation, thickness, and width. These images are reproduced in figures 3.12 and 3.13.

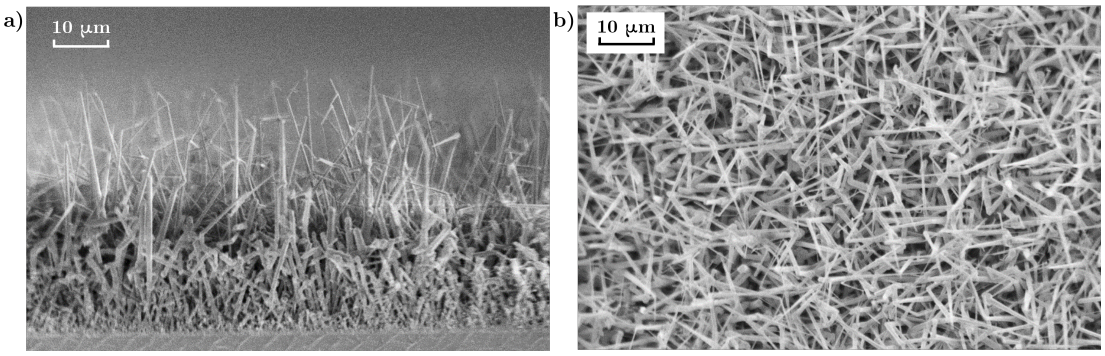

FIGURE 3.12: Cross-sectional (a) and top view (b) SEM images of the uncrushed 100 crystal lattice substrate nanowires, showing some preferential vertical growth in the longest nanowires, but a generally very amorphous system.

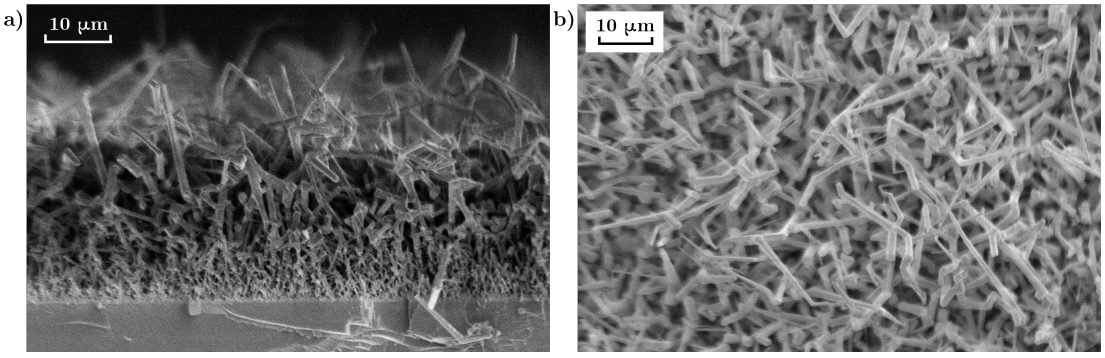

FIGURE 3.13: Cross-sectional (a) and top view (b) SEM images of the uncrushed 111 crystal lattice substrate nanowires.

The images show that despite some preferential growth perpendicular to the substrate for the 111 sample, the bulk of the medium is largely disordered. This would lead us to expect some difference in the transport of light in the direction that is normal to the substrate, but likely little difference in the propagation in the directions parallel to the plane of the surface. The nanowire sample thickness in both cases is taken to be approximately $30\,\mu m$.

3.4.2 Coherent Backscatter Spectroscopy

The coherent back-scatter (CBS) spectroscopy experiment allows measurement of the transport mean free path by fitting the cone of enhanced backscatter relative to the diffuse background. This can be found either by using a reference sample with a vary narrow (or close to negligible) CBS cone, or by using polarisation dependent measurements, i.e. using a polarised source and then selecting the parallel or orthogonal polarisations for the detection channel as described in Section 2.2.2. In the experiments conducted below the former method was taken using a PTFE cap approximately three

millimetres in thickness. One polarisation channel was chosen in the detection using a broadband linear polariser.

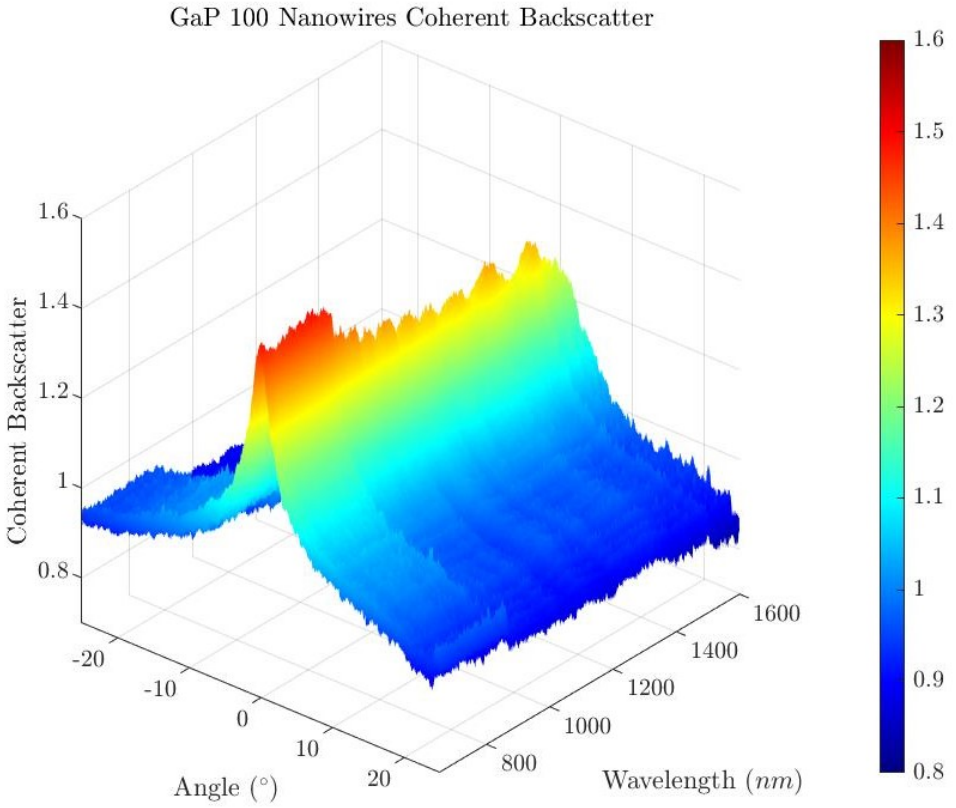

FIGURE 3.14: GaP sample coherent backscatter (CBS) cone normalised to a PTFE reference sample. The sharp peak at 500 nm is due to the onset of a normalisation error with the PTFE reference as the signal begins to drop <500 nm .

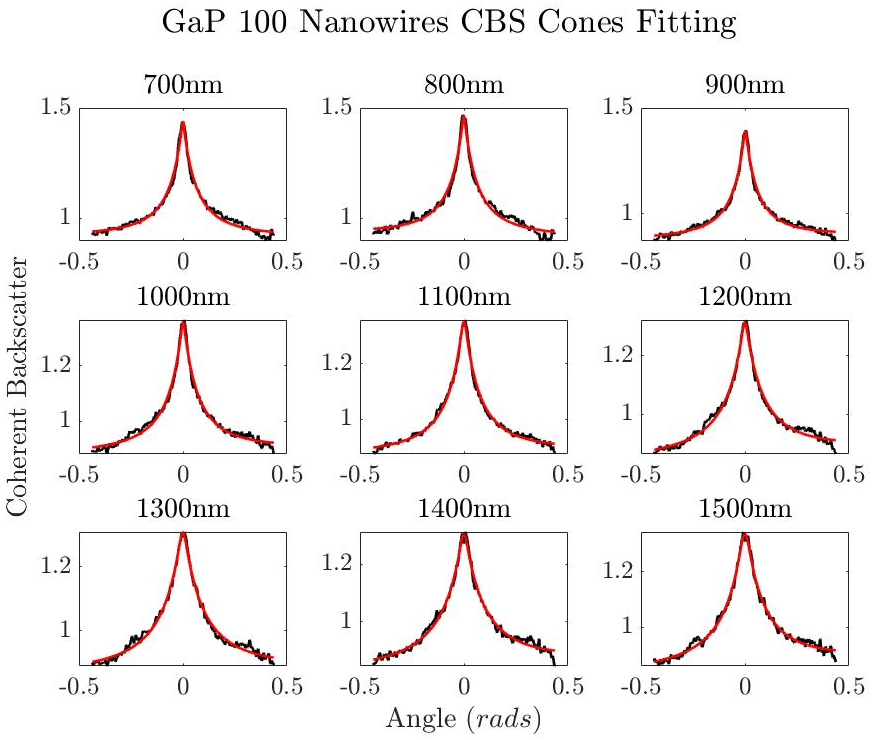

FIGURE 3.15: Cross sections of the coherent backscatter cone of the GaP nanowire 100 sample as shown in Figure 3.14. Red lines are fits to the enhanced backscatter.

Cross sections of the CBS cone can be seen in Figure 3.15 along with fits shown in red. From the fits to the measured CBS cone, the transport mean free path is calculated as a function of the incident wavelength. The limited enhancement factor exhibited is a result of the reduced signal detected in a single polarisation channel.

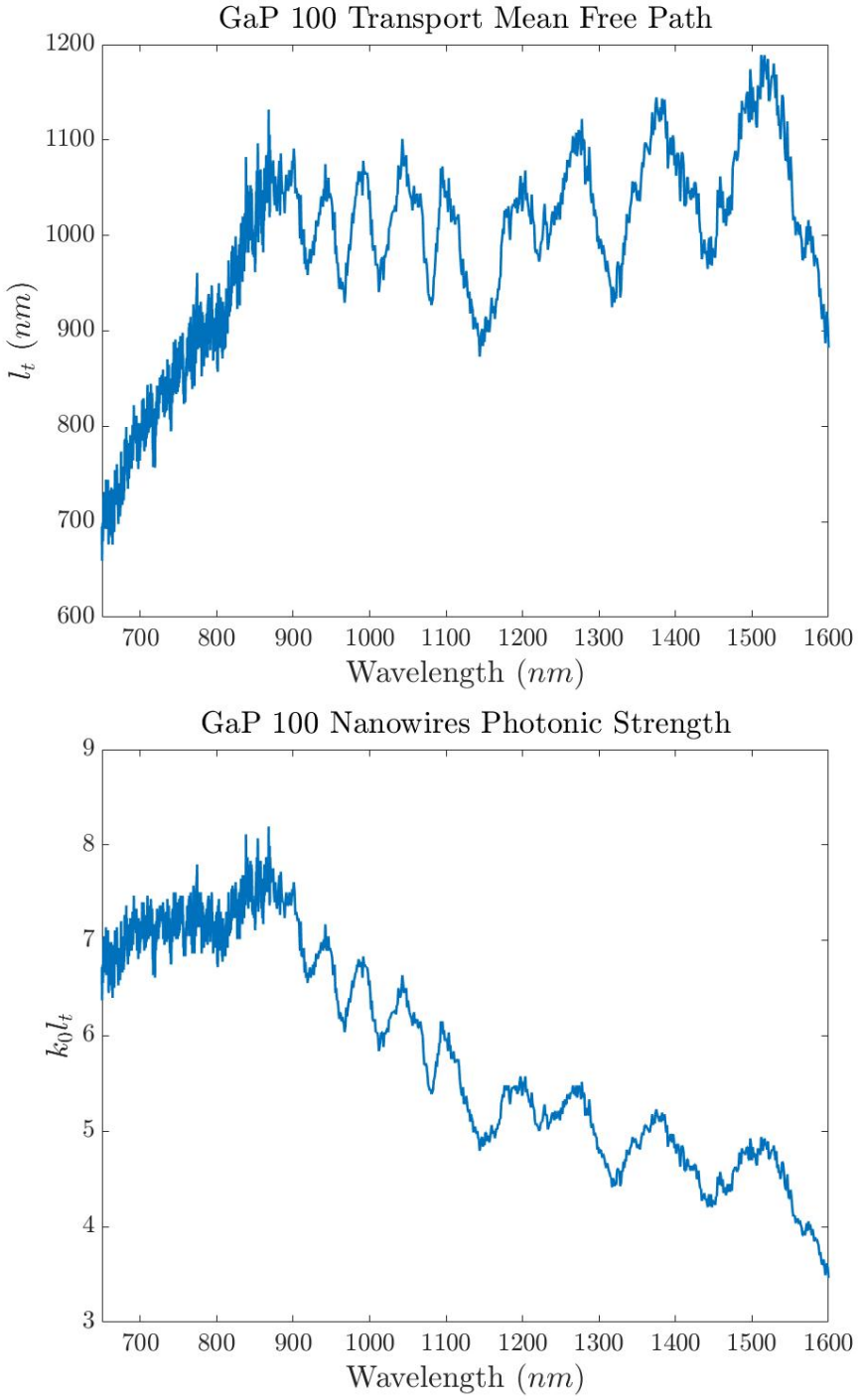

FIGURE 3.16: a) Transport mean free path calculated using the CBS measurement for GaP sample 11779 and b) the photonic strength denoted kl, the product of the transport mean free path l, and the wavenumber k.

The transport mean free path shown in Figure 3.16 shows a strong resonant behaviour in the infrared region, above 900 nm, which would indicate that the light is undergoing resonant scattering. The value of the photonic strength kl continually decreases in the infrared to a minimum value of ≈ 3.5 at the edge of the detection window.

3.4.3 Total Transmission and Reflection Measurements

The total transmission spectra of gallium phosphide nanowire samples are shown in figures 3.17 and 3.18.

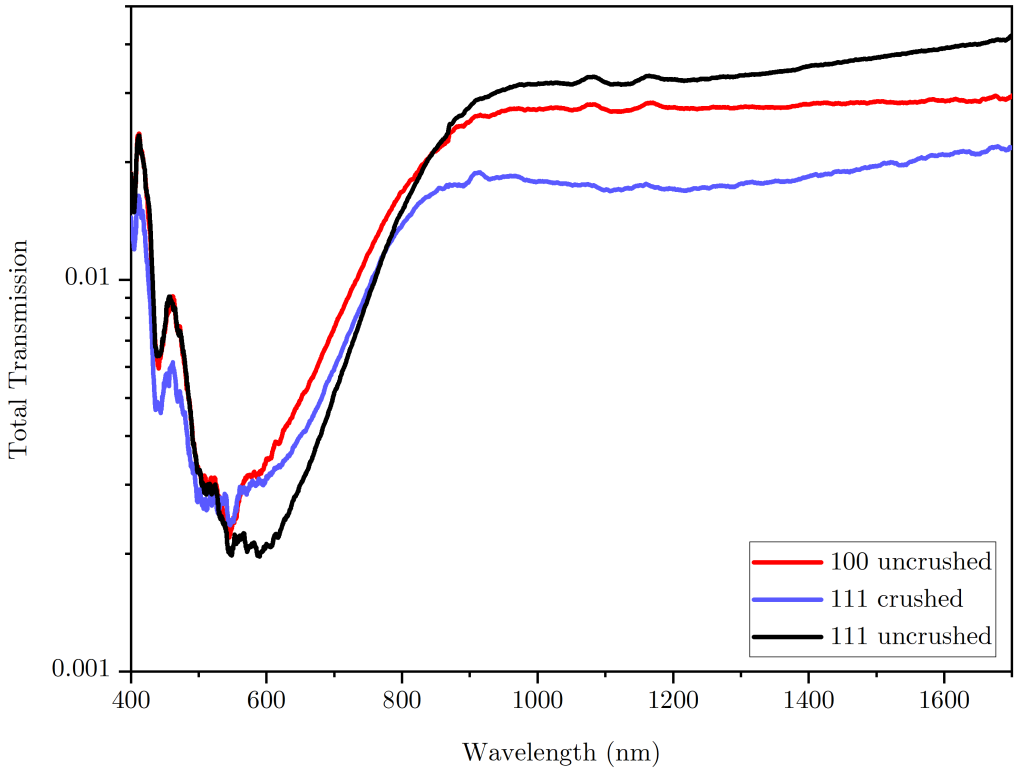

FIGURE 3.17: GaP nanowire samples total transmission measurement. The flattening of the spectrum above 900 nm is indicative of strong scattering. The features at 1100 nm and 1150 nm are experimental artifacts due to large laser powers.

The total transmission measurements corroborate previous measurements of the transmission of GaP nanowires of varying length and radial thickness. The transmission in the near infra-red is used along with the thickness of the nanowire mat to estimate the absorption length in the nanowire layer.

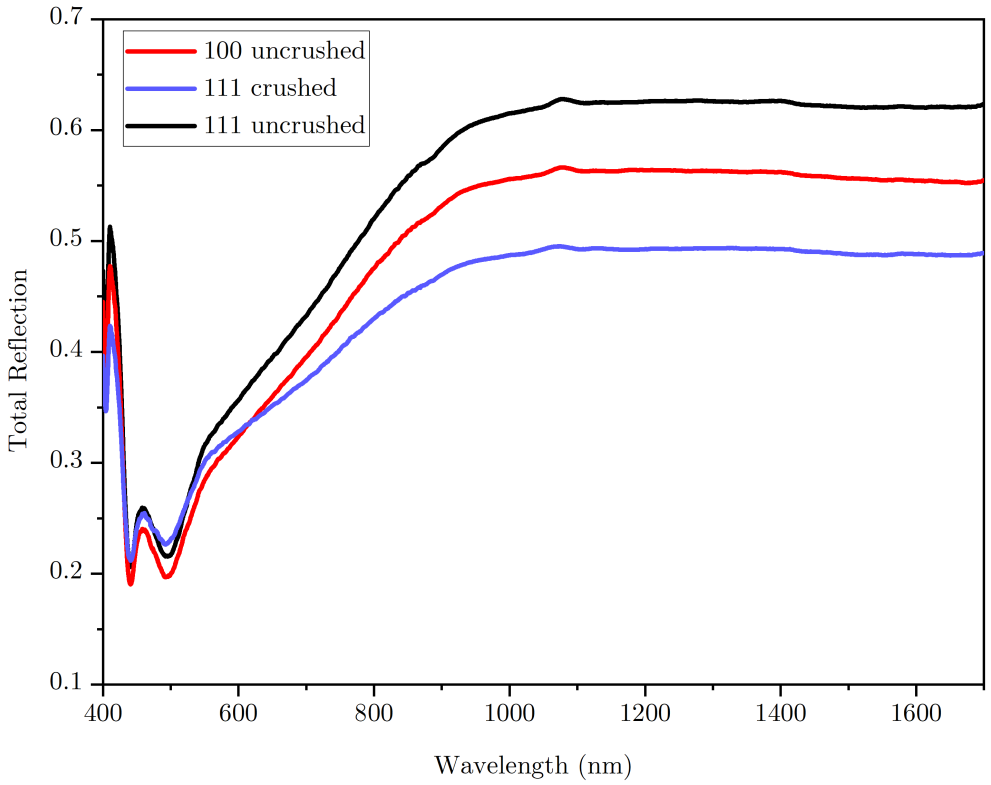

FIGURE 3.18: GaP nanowire samples total reflection measurement. The flattening of the spectrum above 900 nm is indicative of strong scattering.

The reflectivity of the nanowires is shown to be very high for all samples. The total reflection measurement is dependent on the separation of the sample from the rear aperture of the integrating sphere. A significant proportion of the scattered light is lost due to scattering at high angles when the distance between the sample and the rear surface is large. The integrating sphere itself is composed of a white scattering interior with a finite thickness, estimated to be approximately 5 *mm* thick.

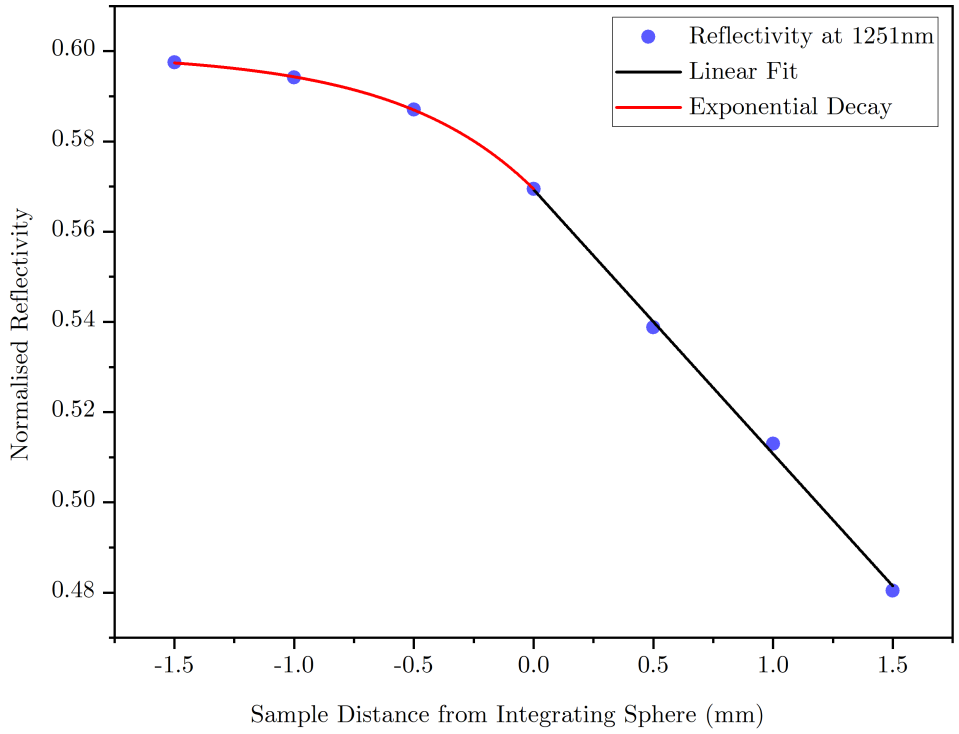

FIGURE 3.19: Measurement of the reflectivity (blue dots) of a sample as a function of the sample distance from the rear surface of the integrating sphere. A linear relationship (black line) is shown up to the point where the sample passes into the aperture, following the increasing solid angle encompassed by the projection of the diffuse reflectivity of the sample. An exponential decay is then seen (red line) which trends asymptotically towards 60% reflection.

The reflectivity is shown to have a linear trend up until it passes the opening of the aperture and begins to enter the integrating sphere, at which point the reflectivity is measured as 0.57. The total reflectivity of the sample then tends towards a value of 0.6 as the sample is passed inside the aperture, shown using an exponential fit. This could indicate that some of the light which is multiply scattered inside the sphere is able to exit the sphere via the rear aperture, and that as the sample holder begins to block the rear aperture its escape is stopped. This is possible since the sample is smaller than the rear aperture, however the sample holder is closer in diameter. Ultimately this measurement indicates that there is a minimum of 3% uncertainty in the reflectivity of the samples, since not all the samples are small enough to pass into the sphere, and since there is an uncertainty in the precise placement of the sample surface relative to the aperture.

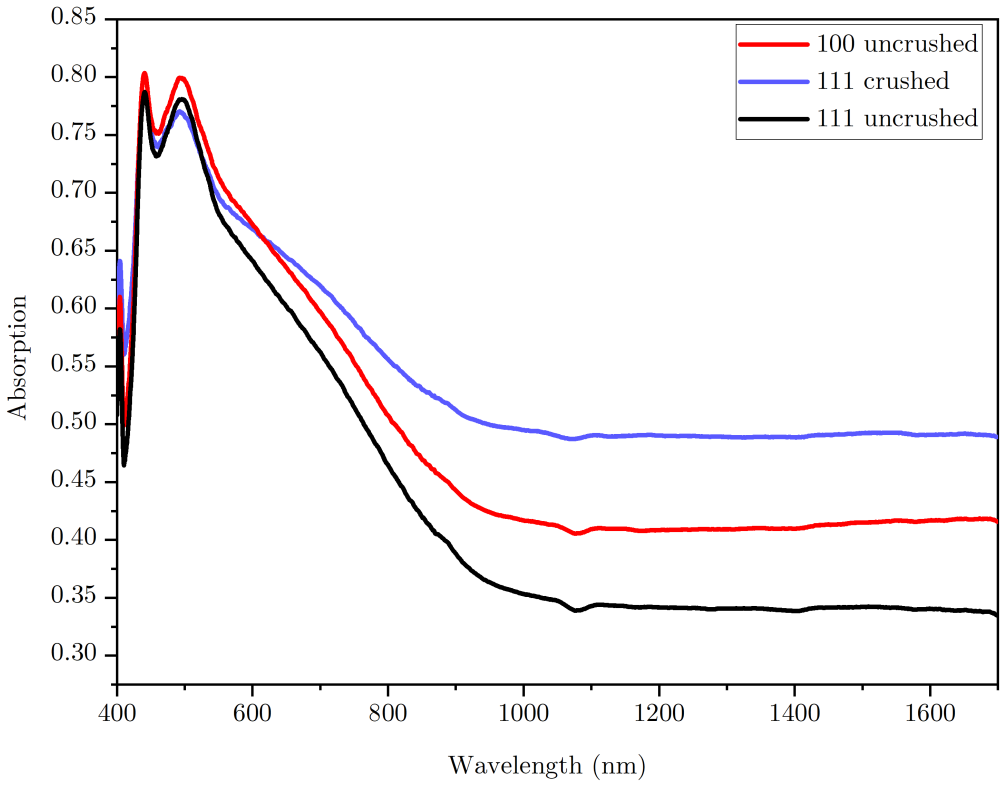

FIGURE 3.20: GaP nanowire samples total absorption, calculated as $A = 1 - T - R$. The large absorption peak at $\sim 570\,nm$ caused by the GaP bandgap can be seen.

The total absorption is given in Figure 3.20 and is calculated using the previous total transmission and reflection measurements. It shows the strong absorption peak due to absorption across the gallium phosphide electronic bandgap at $\sim 580\,nm$.

3.4.4 Estimation of the Absorption Length

Taking the refractive index of GaP at λ=1200 nm as 3.1, and assuming a fill fraction of ~50%, an effective refractive index n_{eff} is approximated to be 1.5. This is calculated using an average of the birefringent refractive index calculated parallel and perpendicular to the nanowire growth following the methodology presented in reference (80). The disordered orientations of the nanowires in the thick scattering slab enables this multiple averaging. The value obtained is reasonable in comparison to similar GaP samples of a lower density (81).

We can calculate the extrapolation length $z_{e_{1,2}}$ at the front and back interface of the nanowires using equations 2.3, taking the front surface to be the air-nanowire interface and the rear to be the nanowire-substrate, and using the Fresnel equations, along with equation 2.4, to calculate the reflectivity at each. The transport mean free path,

$l_t = 1\,\mu m$ is taken to be that measured using the coherent backscattering spectroscopy measurement. The extrapolation lengths at the front and back surfaces are then found to be $z_{e_1} = 0.89\,\mu m$ and $z_{e_2} = 1.9\,\mu m$.

The thickness of the nanowires is taken from previous SEM images and information, given as $L = 30\,\mu$m. In literature, the injection depth z_p is generally approximated to be equal to the extrapolation length at the front surface of the slab, on the order of the transport mean free path of the sample. In the case of the theoretical plots shown in Figure 3.22, z_p is fixed to a value of $1\,\mu m$.

Due to the long length of the nanowires and their very small transport mean free path there is a minimal ballistic component at the exit surface of the sample, indicating that the majority of the light is converted into diffusive propagation.

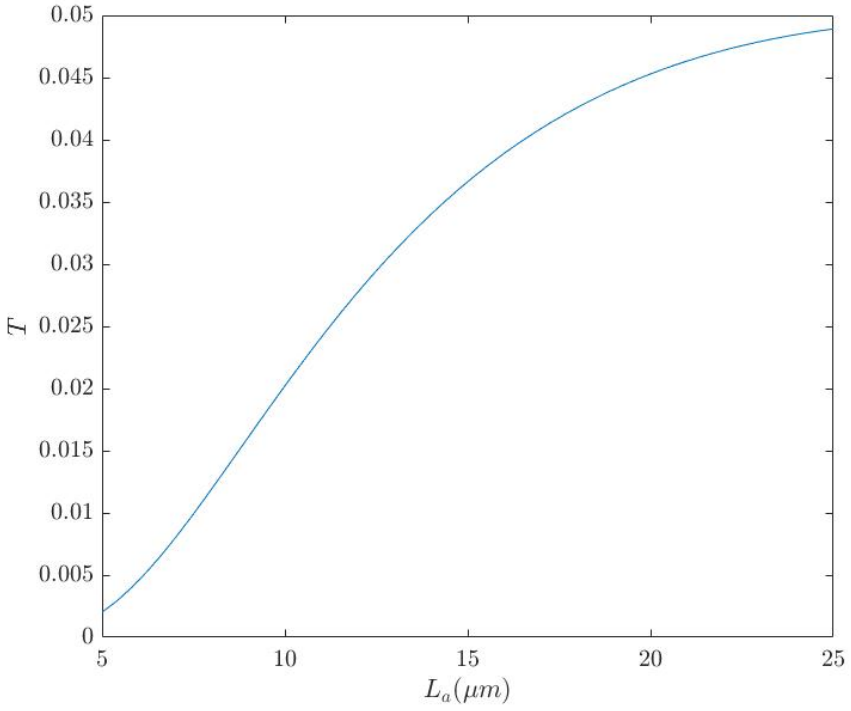

FIGURE 3.21: Total transmission, T, through the diffuse slab of nanowires as a function of the absorption length L_a following equation 2.10. The transport mean free path, l_t, is taken to be $1\,\mu m$, as measured in Section 3.4.2.

A numerical solution is found by plotting the relation between the total transmission, $T = T_{bal} + T_d$ and the absorption length, L_a, given by equation 2.7. As mentioned, the ballistic component of the transmitted light is of the order e^{-30}, making it negligible in comparison to the diffusive transmission, however it is still included in the plot. Using the mean total transmission value at 1200 nm we can find the diffuse absorption length of the nanowires to be $L_a \approx 12\,\mu m$. Using equation 2.5, this translates to an elastic absorption length, l_a, of $432\,\mu m$ in a sample that is approximately $30\,\mu m$ thick.

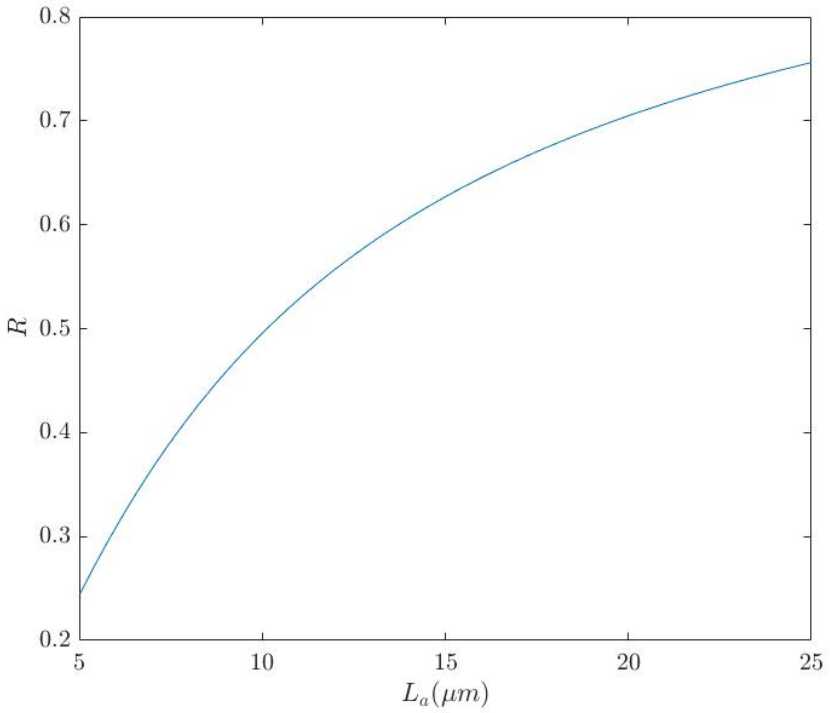

FIGURE 3.22: Total reflectivity, R, through the diffuse slab of nanowires as a function of the absorption length L_a following equation 2.11.

The total reflection, R, is calculated using the diffusive reflectance which is given by equation 2.11, accounting for reflections at the rear surface of the sample, as well as total internal reflection in the substrate.

3.5 Conclusion

In conclusion, a number of static optical characterisation techniques have been used to determine parameters describing the transport of light through the nanowire samples of interest. The effective refractive index is calculated as a function of the filling fraction of the material ($\sim 50\%$) and the refractive index at $1200\,nm$, ~ 3.1.

The coherent backscatter measurement is used to determine the transport mean free path, $l_t = 1\,\mu m$ at $1200\,nm$, also providing spectral information in the range of interest and showing the photonic strength of the sample, $kl \sim 5.5$. Though still far from the expected transition from purely diffusive to partially localised light transport, it is nonetheless an indication of very strong scattering. The value obtained for l_t is the mean value for the vector transport mean free path which describes the propagation in an anisotropic sample. This is due to the radial averaging of cone by rotating the sample, thus reducing the angular speckle intensity.

The total transmission and reflection measurements are used to estimate the absorption length of the material, using a diffusive model of light propagation through a thick, multiply scattering slab, giving an absorption length $L_a = 12\,\mu m$. This measurement is strongly dependent on the transport mean free path. The total reflection measurements were shown to underestimate the reflectivity of a sample in the visible region of approximately 20%, accounting for which there is reasonable agreement between the static reflectivity predicted by the diffusion approximation, and the experimental results obtained.

Chapter 4

Ultra-fast Pump Probe Measurement for Direct Determination of the Anisotropic Diffusion Constant

4.1 Introduction

The pump probe method for temporal measurement allows for the capture of ultrafast processes which occur on the picosecond to femtosecond timescales. This is achieved using two separate short pulses from a coherent light source which arrive at the sample at a variable time delay. Initially a probe pulse is incident on the sample and is measured by a detector. Then a second pulse, commonly referred to as the pump pulse, perturbs the system. Another probe pulse is then transmitted through the sample after a short time and the changes to the sample caused by the pump pulse are encoded in the properties of this second probe pulse. This provides what can be described as a snapshot of the sample at the time, t, given by the separation of the two pulses. By varying the time delay between the two pulses a description develops of the temporal evolution of the system, the resolution of which is determined by: the accuracy to which one can control the separation of the two pulses, the duration of the pulses, and the limit of the detection of the signal from the background.

For the case presented in this report, the system interrogated is a strongly scattering finite slab which is perturbed by absorption of the pump pulse. The pump pulse is at an energy above the bandgap of the material and causes changes to the real and imaginary part of the refractive index of the material; the real part of which, we assume has a minimal effect on the transmission of the probe. The absorption leads to a localised increase in the free carrier charge density, leading to a very sharp increase in the absorption coefficient (82). This has been demonstrated using dense layers of nanowires in time resolved experiments (83), which show that the relaxation time of the electrons

is of the order of tens of picoseconds. This change to the imaginary refractive index means that the probe pulse, which remains at an energy below the band-gap of the material, can now be absorbed through transient absorption in the pumped region. In a finite slab of dielectric material it is assumed that the absorption of the pump happens over a time scale much shorter than the length of the pump pulse, and that it occurs at, or near to, the surface of the scattering region.

In the case of a strongly multiple scattering sample this process could be used to determine the diffusion constant of light through the sample by measuring the transmitted intensity. The measured intensity reveals the relative path length distribution of the material, or equivalently the distribution of path diffusion times, t_{dif}. This can be envisioned quite clearly by fixing the time of incidence of the probe at time $t = t_0$ and varying the time of incidence of the pump, t. If we consider the evolution of the probe pulse according to this time difference, $t_0 - t$, at positive times ($t_0 > t$) the probe is incident after the pump. Due to the long relaxation times of the excited electrons in the sample, the probe is absorbed leading to a change in the measured intensity of the transmitted probe. At negative times the probe is incident before the pump ($t_0 < t$) and thus is transmitted freely through the material until the pump is incident. Only the long scattering paths persist in the material long enough to arrive at the exit surface at the same time as the pump in the negative time domain.

The measured time trail in such an experiment is in fact an integral of the diffuse transmission, again due to the relatively long relaxation time of the electrons in the sample. This can be shown analytically as at a given negative time, $t_0 - t < 0$, the probe has progressed through the sample such that the short time trails $t_{dif} \ll t$ have escaped the exit surface. At time t the pump is then incident on the surface of the sample and due to the long relaxation time of the material any light paths which arrive after this time will be absorbed. The total change in the transmitted pulse is an integral of the transmission through the slab given in equation 2.18,

$$\begin{aligned} T(x,y,t) = \int_0^t \frac{S_0}{16\pi^{\frac{3}{2}} t^{\frac{5}{2}} \sqrt{D_z D_r^2}} \exp\left(-\frac{r^2}{4D_r t}\right) \exp\left(-\frac{(2D_r + D_z)t}{3L_a^2}\right) \\ \times \sum_{m=-\infty}^{\infty} \left[A'(m) \exp\left(-\frac{A'(m)^2}{4D_z t}\right) - B'(m) \exp\left(-\frac{B'(m)^2}{4D_z t}\right) \right] dt, \end{aligned} \tag{4.1}$$

where $A'(m) \equiv (2m+1)(L + 2z_e) - 2l_t z_e$ and $B'(m) \equiv (2m+1)(L + 2z_e) + l_t$. The extrapolation length z_e given here is measured as the mean of the front and rear extrapolation lengths $z_{e_{1,2}}$ and the diffuse injection source is replaced with a Dirac delta function, S_0.

The transmission at a given time, t, is given as the integrand of equation 4.1, and can be found experimentally by differentiating the experimental data. The first component

of the integral describes the temporal evolution of the transmitted diffuse intensity as a function of time. The first exponential term describes the spatial extent of the transmitted intensity as a function of time and is therefor a function of D_r. The second exponential term represents absorption in the sample and is thus a function of the absorption length, L_a, and the diffusion in all three spatial dimensions. The infinite sum incorporates the recurrent total internal reflection of the diffuse intensity at the front and back surfaces of the sample.

Measurement of the transmitted probe beam can be analysed using lock-in detection, i.e. measuring the response of the probe pulse at the frequency of the pump pulse, and then comparing this with the unperturbed probe pulse. The pulse repetition rate is at a much higher frequency ($\approx$ 80 MHz) than the laser noise bandwidth, allowing pulse to pulse comparison.

By combining this temporal measurement with spatial mapping, it is possible to explore the diffusion of light simultaneously across three independent variables, x, y and t, in a single measurement. This mapping can be achieved by keeping the position of the probe fixed on the sample and translating the pump in space across the surface. The diffusion of the probe through the sample to a given point can then be measured for a series of points in space and time to develop a three dimensional description of the light propagation.

4.2 Ultra-fast Pump Probe Time of Flight Experimental Set Up

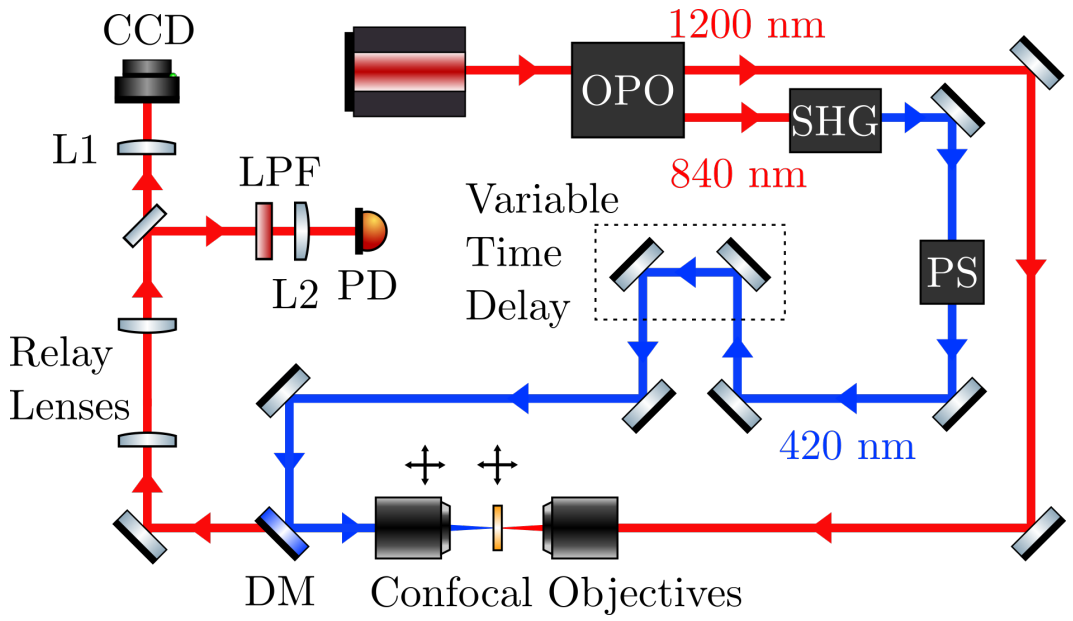

FIGURE 4.1: Experimental set up diagram of the pump probe measurement. Light from a pulsed laser source is passed through an Optical Parametric Oscillator (OPO). The input beam to the OPO, the pump pulse (dark blue), is then frequency doubled in a Second Harmonic Generator (SHG) before being passed through a pulse select (PS), an acousto-optical modulating Bragg cell is used to reduce the repetition rate of the pump laser from 80 MHz to 10 MHz. The pump pulse is directed onto the sample surface through a dichroic mirror (DM) and an objective lens. The second OPO output, the probe pulse (red), is incident on the sample via a second objective lens. The two beams can be observed by focusing the image of the transmitted and reflected spots onto a CCD camera (CCD) using a focusing lens (L1). The probe beam passes through the dichroic mirror to an avalanche photo-diode (PD) via a focusing lens (L2) and a long pass filter (LPF).

In order to observe the ultra-fast dynamics of light propagation on a microscopic scale we utilise a pump probe detection method and measure transmission fluctuations using a lock-in amplifier. The experiment is carried out using a tunable pulsed Ti:Sapphire *Coherent* Chameleon Ultra II laser, with a repetition rate of 80MHz and set to a wavelength of 800 nm . This is fed into a *Coherent* Compact Optical Parametric Oscillator (OPO) which is tunable in the wavelength range of 1000 nm to 1600 nm . This OPO outputs both the 800 nm input beam as well as a down-converted beam, preserving the repetition rate of the input beam in both. The 800 nm output is then passed through an *APE* Harmonixx second harmonic generator (SHG) which outputs at 400 nm . This is then passed through an acousto-optic-modulator (AOM) which is driven by a function generator at 10 MHz, allowing for the control of the repetition rate of the pulse from the SHG output. The first order diffraction from the AOM is then used as the pump pulse, and is directed using the convex lens L1. This is passed through a time delay line stage which allows the time of incidence on the nanowires to be varied. The pump beam is

then passed through a 50x objective with NA 0.55. The probe pulse meanwhile passes through an extended fixed time delay such that it is coincident with the pump pulse on the sample at a time t_0. This too is passed through a 100x objective with NA 0.50.

The probe pulse then travels through the sample and the objective placed on the pump side. It then passes through a dichroic mirror (DM), a focusing lens (L2) and a set of long pass filters (LPF). The use of the dichroic mirror is to allow the pump pulse to be directed onto the sample while simultaneously measuring the probe pulse using an InGaAs avalanche photo-diode detector (PD). The long pass filters and the dichroic mirror reduce the detection of any reflections of the pump pulse from the surface of the sample. The alignment of the incident beams can be checked in real time using the CCD cameras shown in Figure 4.1. Using these cameras we can check the focus of both beams as well as their relative positions. The photo-diode is connected to a *Zurich Instruments* UHFLI 600 MHz Lock-in Amplifier which measures both the transmission of the unperturbed pulse at a frequency of 80MHz and the perturbed pulse at 10MHz. By subtracting the 10MHz signal from the 80MHz signal, we obtain ΔT, a measure of the change in transmission incurred by the pump pulse. To account for any drift in the laser power this is then normalised to the transmission of the unperturbed probe.

Since the photo-luminescence caused by the excitation of electrons in the GaP nanowires will have decay times typically on the scale of nanoseconds, the impact on the measurement will be minimal since the time of flight for the light to transit the sample should be on the order of picoseconds (84).

4.2.1 Thermal Background Excitation

One of the issues with this method of measurement is that a large portion of the energy imparted into the scattering structure will be converted into thermal energy as it dissipates through the inelastic scattering of excited electrons. This relaxation will lead to a thermal signal, as the slow reduction in the amount of excited electrons causes a gradual decrease in the change in transmission of the probe (85). This thermal signal will also have a temporal frequency matching that of the pump pulse which means its effect on the probe will be detectable when using lock-in detection.

The thermal background becomes a significant problem when the effect of the initial pump pulse on the probe signal is very small (i.e. at long negative times where only the longer paths of the probe are present). Due to the time delay of this thermal effect from the initial pump pulse, it is possible to isolate this thermal effect into a separate channel by carefully choosing the phase of the desired signal relative to the unpumped signal. This however cannot be done continually throughout the spatial mapping process, and so to overcome this two possible solutions are presented in Section 4.2.1.

Two different methods were investigated to try and reduce the effect of the thermal background noise. The first involved focusing the probe signal through a pinhole which isolates the area of the probe constrained within the pump pulse profile. This negates the outer area of the pump where the inelastic transfer of energy can cause thermal excitation, and hence absorption of the probe pulse. This method has a key drawback however, since it is not easily adaptable for spatial mapping in the current set up. Since the pump pulse is scanned across the surface of the sample by translating the pump objective, as the sample is scanned the transmission through the pinhole would be constantly changing due to the small variation in the projected image of the probe. Without the pinhole this effect is negligible due to the relatively large detection area afforded by the photodiode and focusing lens, however when the pinhole is introduced the measured area is reduced significantly.

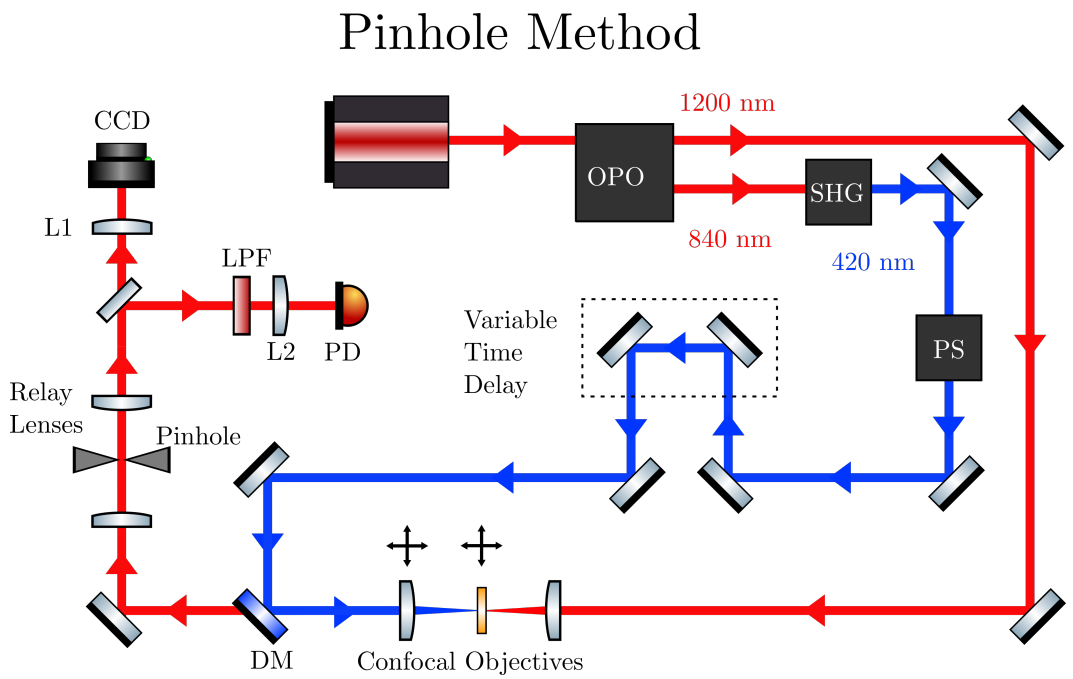

FIGURE 4.2: Experimental set up diagram of the pump probe measurement featuring the pinhole thermal background removal method. The experimental method is as described in Figure 4.1, with the added inclusion of a pinhole at the foci of the relay lenses in the detection path. This has the effect of removing the higher order spatial frequencies from the detected signal, reducing the detection region to a small point at the centre of the pumped region.

The second method investigated was to recombine the zero order output of the acousto-optic modulator (AOM) with the first order pump pulse at a given time delay. The thermal excitation would then occur at a repetition rate of almost 80MHz, with a mis-step where the recombination occurs. By controlling the intensity of the zero order component it was postulated that the thermal excitation could be maintained at a semi-constant level and rather than oscillating at the sensitive detection frequency at 10MHz, the thermal background could be shifted to the laser frequency. In order to recombine

the two beams such that they are coincident on the sample at the same angle and position, a polarising beamsplitter is used. The intensity of the zero order can be controlled by varying the orientation of the half wave plate. This experimental set up is shown in Figure 4.3.

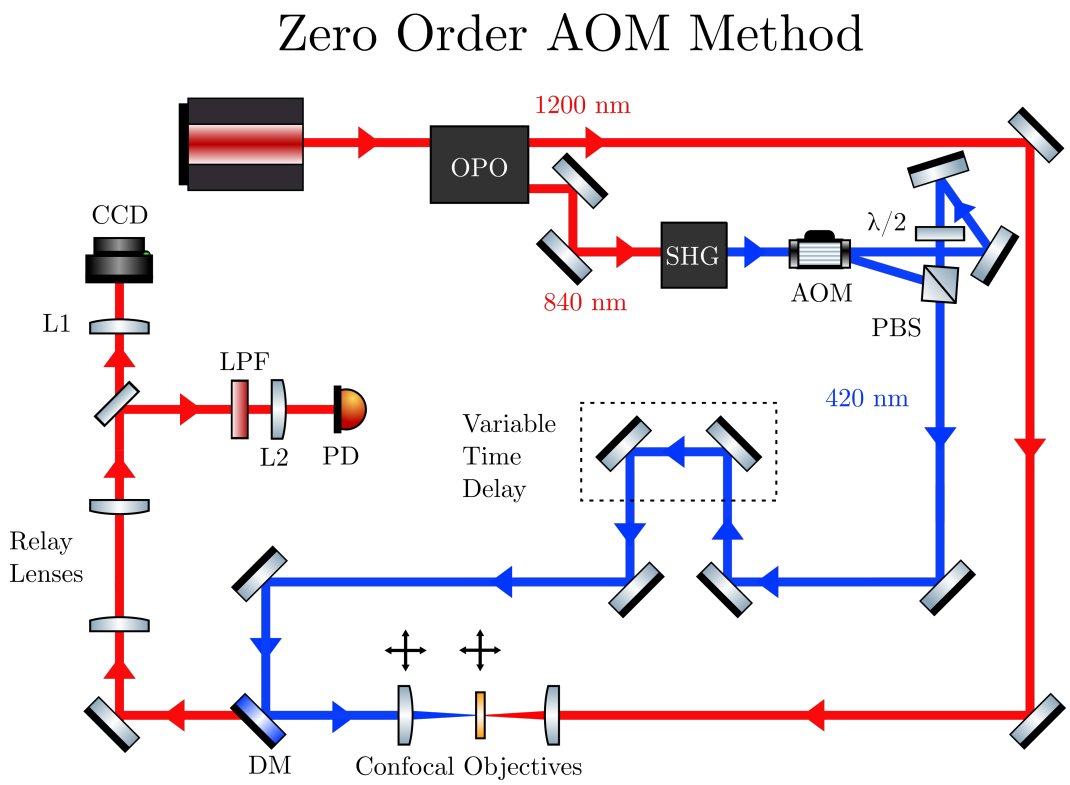

FIGURE 4.3: Experimental set up diagram of the pump probe measurement featuring the AOM thermal background removal method. The experimental method is as described in Figure 4.1 however the pump beam is periodically diffracted in an Acousto-Optic-Modulator (AOM). The zero order from the AOM (light blue) is then recombined with the first order using a half wave plate ($\lambda/2$) and a polarising beam-splitter (PBS). The pump pulse train is directed onto the sample surface through a dichroic mirror (DM) and an objective lens. The second OPO output, the probe pulse (red), is incident on the sample via a beam-splitter (BS) and a second objective lens. The same detection apparatus is used as in Fig. 4.1

Shown in Figure 4.4 are the time traces for the two methods of thermal background reduction and the raw time trace. All are taken from the same position such that the pulse and probe are overlapping and all have constant phase between the measured signal and the thermal background, i.e. the phase has not been adjusted to shift the thermal signal to the perpendicular channel. It can be seen that the raw signal tends to a background measurement of 3×10^{-5} whereas the time trace for the two scans using the background reduction method tend to zero.

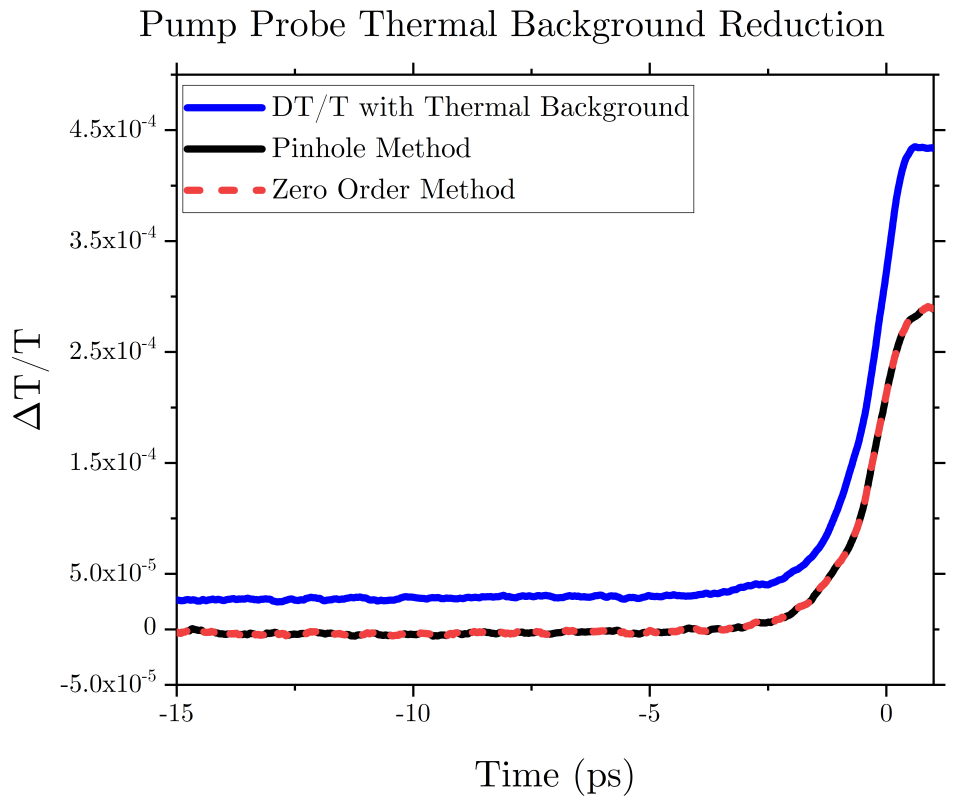

FIGURE 4.4: Pump Probe time traces for the different thermal background reduction techniques, the pinhole method (black), and zero order method (red dashed) show very good agreement with each other and both show significant reduction of the background from the original signal (blue) at long negative times.

There is very good agreement between the pinhole and zero order measurements, with both having nearly identical time traces. The absolute value of the background drops to zero in the long-time trace, indicating a negation of the thermal contribution; however, neither technique appears to reduce the inherent noise in the long time trace. The mean and standard deviation in the region of 5 to 20 *ps* is given for the three methods below.

Method	Mean (10^{-6})	Standard Deviation (10^{-6})
Spatial Filter	-2.76	2.68
Acousto-Optic Modulator	-2.76	5.08
No Reduction Method	0	2.10

TABLE 4.1: The mean and standard deviation in the long time background between 5 and 20 *ps* for two methods of reducing the thermal background contribution, compared with the normalised signal. The mean value of the background signal is subtracted before normalisation for the unmodulated signal (No Reduction Method).

By subtracting the mean of the thermal background before normalisation, as would be done when analysing the time resolved transmission experiment, a comparison of

the relative noise in the long time tails may be made. The standard deviations are calculated over 15 *ps* and show that although the methods shown do reduce the thermal background contribution to the signal, the noise is not improved and in fact, in the case of the acousto-optic modulator, doubled when compared with the raw signal. It is therefore reasonable not to implement these methods, since the measurement of the decay of the long light paths is the key interest in the pump probe experiment.

4.2.2 Boxcar Lock-in Measurement

The boxcar integration method reduces the noise in the measurement due to frequencies outside the signal trace. The signal from the avalanche photodiode is typically $\sim 15\,ns$ long and oscillates as shown in Figure 4.5. When measuring a signal at a specific frequency it can be useful to look at the region encompassed only by a single trace element within the region of interest and disregard background noise in the time outside of the pulse region. This is achieved by convoluting the signal with a square wave function of the desired frequency and with a chosen duty cycle and phase to optimise the signal output.

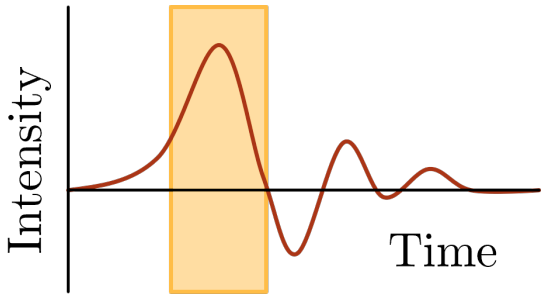

FIGURE 4.5: An example illustration of the boxcar region imposed around the avalanche photodiode detector time trace. The orange region depicts the region over which the signal is integrated.

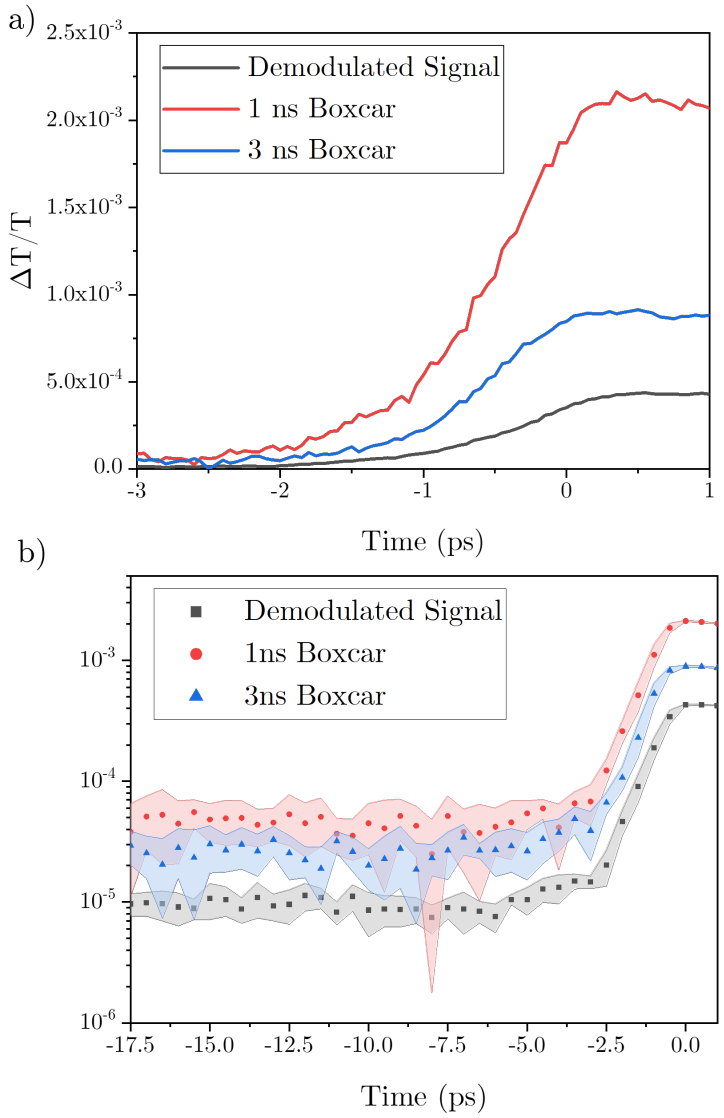

FIGURE 4.6: The pump probe time traces for two different boxcar integration times compared to the raw signal plotted on a) a linear scale and b) a logarithmic scale. It can be seen that as the boxcar interval becomes smaller, no boxcar $>$ 3 ns $>$ 1 ns, both the signal and background noise increase.

A measurement of the pump probe response of GaP nanowires was taken for a single point of zero separation of pump and probe, using two different boxcar settings and once with no boxcar integration. The time traces of these measurements are given in Figure 4.6 and statistical analysis is then used to determine the effectiveness of the boxcar integration method.

By taking the standard deviation in the background noise region of -5ps to -3ps, we are able to find the signal to noise as a ratio of the increase in signal, thus gaining a measure for the effectiveness of this method.

Boxcar Envelope (ns)	Background	$\sigma_{Background}$	Maximum Signal	SNR	SBR
No Boxcar	2.99×10^{-6}	9.80×10^{-6}	4.38×10^{-4}	146.4	44.71
1	2.15×10^{-5}	4.60×10^{-5}	2.2×10^{-3}	100.55	46.98
3	1.16×10^{-5}	2.75×10^{-5}	9.18×10^{-4}	79.05	33.38

TABLE 4.2: Comparison of the background noise in the region of -20ps to -5ps to the maximum signal measured for two different boxcar integration times as well as for the raw pump probe signal. The Signal to Noise Ratio (SNR) is the ratio of the maximum signal to the standard deviation in the background. The Signal to Background Ratio (SBR) is the ratio of the maximum signal to the average value of the background noise.

This method of analysis indicates that while the boxcar integration does increase the signal acquired, it also increases the sensitivity of the measurement to noise in the background. When considering both the signal to noise ratios and the signal to background ratios outlined in table 4.2, it seems that the boxcar did not have a positive effect on the pump probe measurement. However it is important to note that this measurement was only carried out for a single time trace, averaging over many scans should reduce the standard deviation in the background both with and without the boxcar. This becomes significant when we consider the objective of the boxcar measurement. With the boxcar we aim to see further back into the negative time domain, thus we need a large signal to background ratio. In this respect the boxcar has provided some improvement and, although it is difficult to say with certainty after a single measurement, with further optimisation this may prove to be valuable for future measurements.

4.3 Temporal Response and Time of Flight Distribution

By differentiating the data temporally it is possible to obtain the transmission as a function of time and radial separation. This is done with a simple point to point differential. Noise is reduced by oversampling the experiment and then performing a moving average of the measured data. It is important to note that the resolution of each measurement of the change in transmission is limited by the temporal extent of the pump and probe, corresponding to a convolution with two pulses which are 150 fs at minimum, disregarding any dispersive effects induced by the SHG or other optics. This should be considered when sampling the data and in each case the measurement is smoothed by a moving average of 3 points, corresponding to a timescale of 150 fs.

In order to fit the data we must consider that the measured data is for the change in transmission induced in the probe, not for the absolute value of the transmission predicted by equation 4.1. This, coupled with experimental losses such as through beamsplitters, means that we must normalise our theoretical fits to our data in order to get an accurate comparison of the temporal and spatial diffusion. This is achieved using a variable fitting parameter representing the amplitude, a, as a normalisation coefficient.

The exact timing of incidence of the probe pulse into the rear of the scattering sample is unknown in the experiment. The peak of the change in transmission due to the pump pulse occurs at a time when there is maximal temporal and spatial overlap of the pump and probe pulse, which according to the assumptions that the pump does not penetrate deeply into the scattering sample before absorption, would mean that this peak indicates the peak of the probe pulse intensity is overlapped with that of the probe. In other words, if the probe arrived any earlier at the surface of the sample, electronic relaxation would mean a lower number of excited states were available to induce absorption of the probe, leading to a reduction in the change in transmission; any later and the leading edge of the probe pulse would have passed through the sample entirely before the excitation of electronic states at the surface could induce absorption, thus also leading to a reduction of the measured signal. It is possible therefore, when looking at the differential of the measured signal, to take the zero time, t_0, at an early time where the gradient is relatively close to 0.

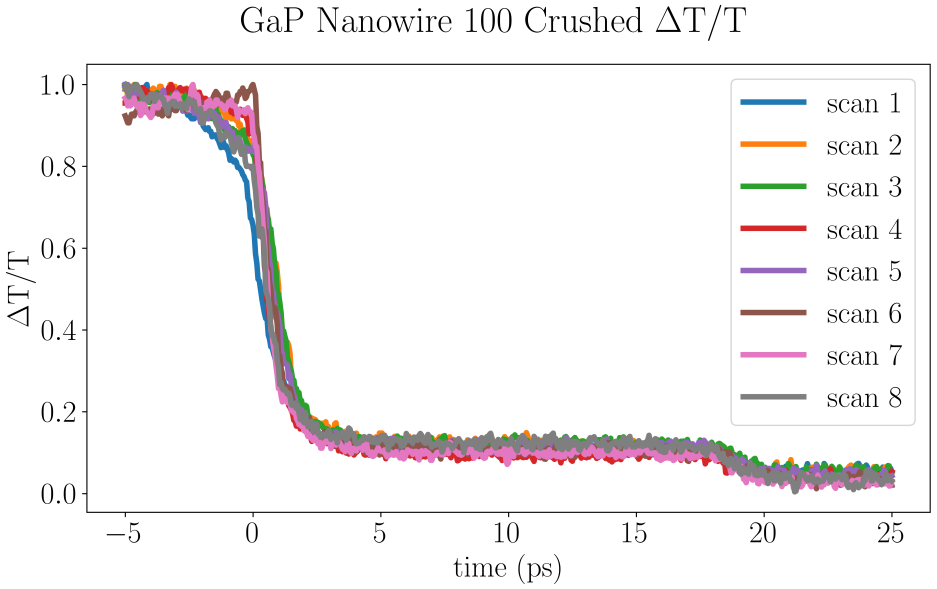

FIGURE 4.7: An example of the measured signal for the 100 orientation crushed gallium phosphide nanowire sample for several scans over different sample positions. By moving over several sample positions, the temporal speckle is averaged and the diffuse intensity may be measured. The measurement highlights the problem of finding the exact the zero time without having a reference for the time of incidence. The peak measured intensity is normalised to 1 across all samples.

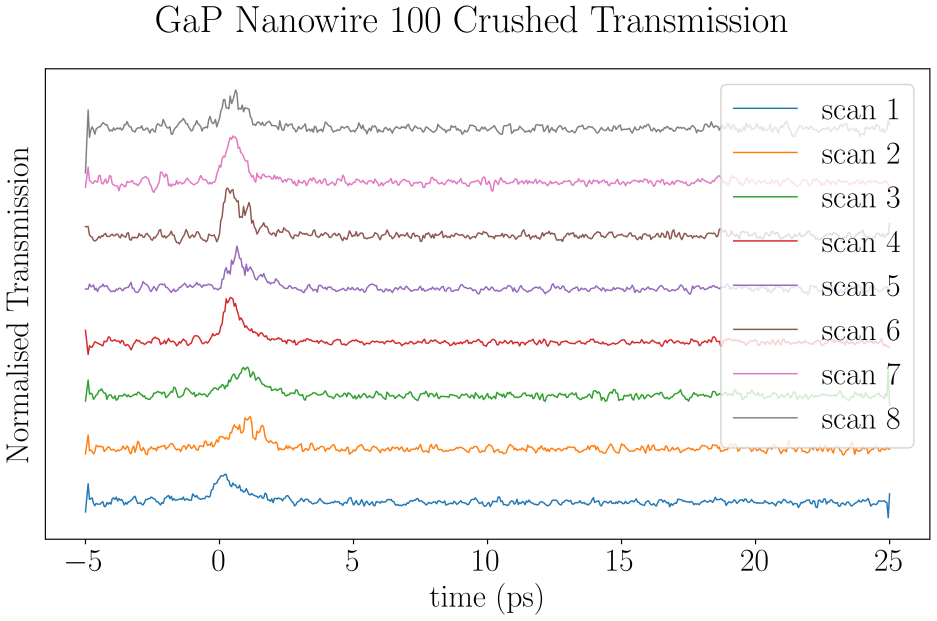

FIGURE 4.8: An example of the normalised transmission, measured as the differential of the measured $\Delta T/T$ signal for the 100 orientation crushed gallium phosphide nanowire sample for several scans. The $\Delta T/T$ signal is normalised prior to differentiation, leading to the normalised transmission shown. The The pump probe signal is seen as a peak at $t = 0\,ps$.

.

When measuring the time dependence the fitting function uses a variable parameter, t_c, added to the time value, which allows closer fitting to the experimental data due to the uncertainty in the exact position of the zero time. This variable parameter is of the order of 10s of femtoseconds and leads only to a linear shift in the theoretical fit to the data in time.

When measuring the transmission, we make the distinction of redefining the long time trail from the negative times for $\Delta T/T$, to the positive for the differential of $\Delta T/T$. Thus the data describes the transmission as a function of time from the moment of incidence of the source.

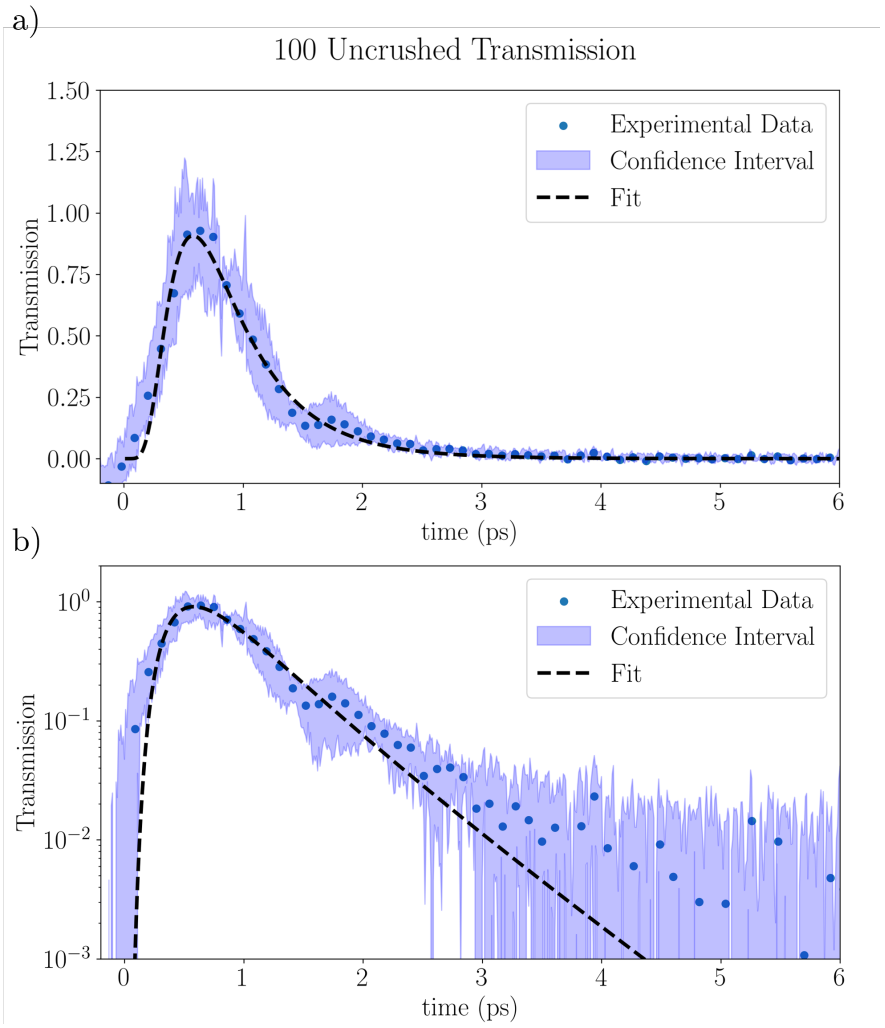

FIGURE 4.9: Time of Flight measurement for the 100 uncrushed nanowire sample at the central position ($r = 0\,\mu m$), shown on (a) a linear and (b) a logarithmic scale. Solid blue circles indicate an 11 point moving average to the data, corresponding to a 110 fs window. Light blue shaded region shows the standard deviation across 6 different sample positions. Dashed black line shows the theoretical fit to the data with a diffusion constant of $D_z = 92 \pm 1\, m^2 s^{-1}$

.

The transmission measurement for the uncrushed 100 nanowires sample is taken using a much higher temporal resolution than the subsequent measurements, which leads to a much lower uncertainty due to the variance of the intensity over the larger number of time steps.

A sharp dip in the transmission is seen at a time of 1.5 ps for the 100 uncrushed sample. This reduction is not seen in any of the other samples. This represents physically a lower than expected change in the transmission of the probe in the experiment. A number of possible non-linear effects can lead to a negative impact on the detected change in transmission of the probe pulse. An overview of the nonlinear photo-electronic interactions which cause the pump probe signal is given in (86). In order to correctly

attribute this phenomenon a more detailed description of the dynamics of the non-linear processes involved in the experiment is required which goes beyond the scope of this thesis.

It is also of note that we are not including effects on the diffusion constant due to localisation or band edge transitions such as a renormalised, time or space dependent diffusion constant. This is supported by the fact that we remain outside well outside the Ioffe-Regel criterion for localisation ($k_0 l_t \sim 5.5$).

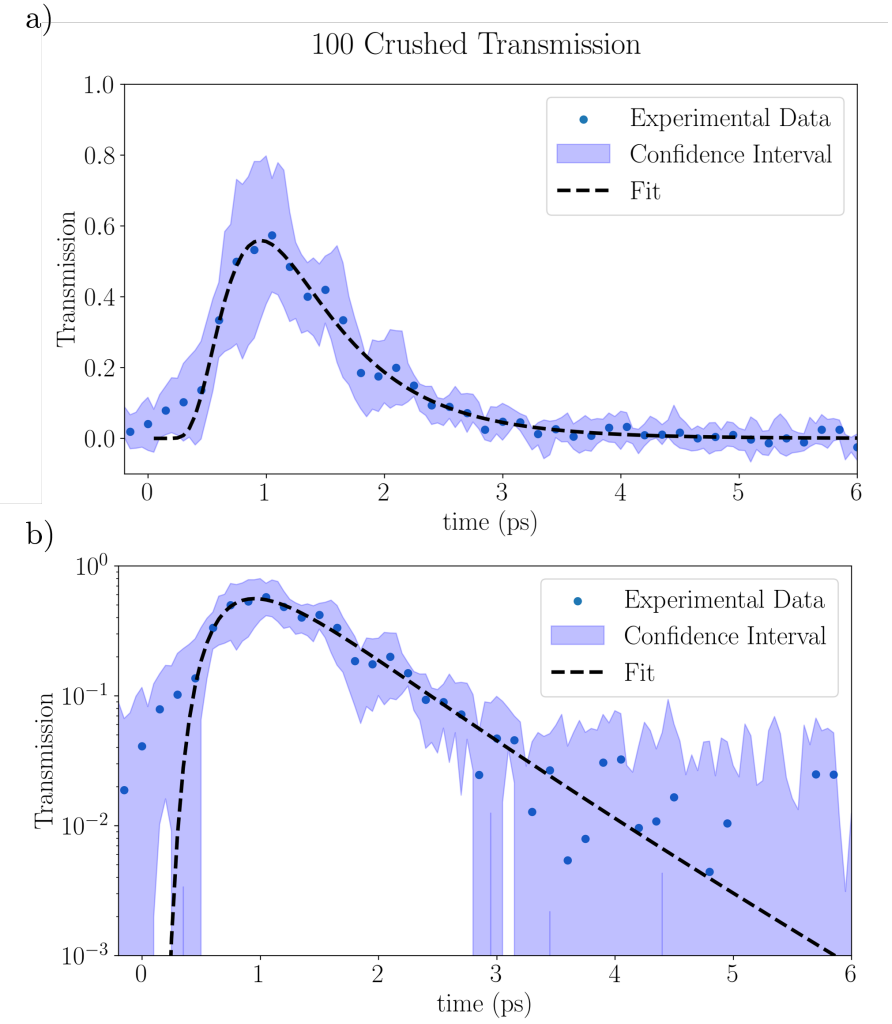

FIGURE 4.10: Time of Flight measurement for the 100 crushed nanowire sample at the central position ($r = 0\,\mu m$), shown on (a) a linear and (b) a logarithmic scale. Solid blue circles indicate a 3 point moving average to the data, corresponding to a 100 fs window. Light blue shaded region shows the standard deviation across 8 different sample positions. Dashed black line shows the theoretical fit to the data with a diffusion constant of $D_z = 71 \pm 3\, m^2 s^{-1}$

.

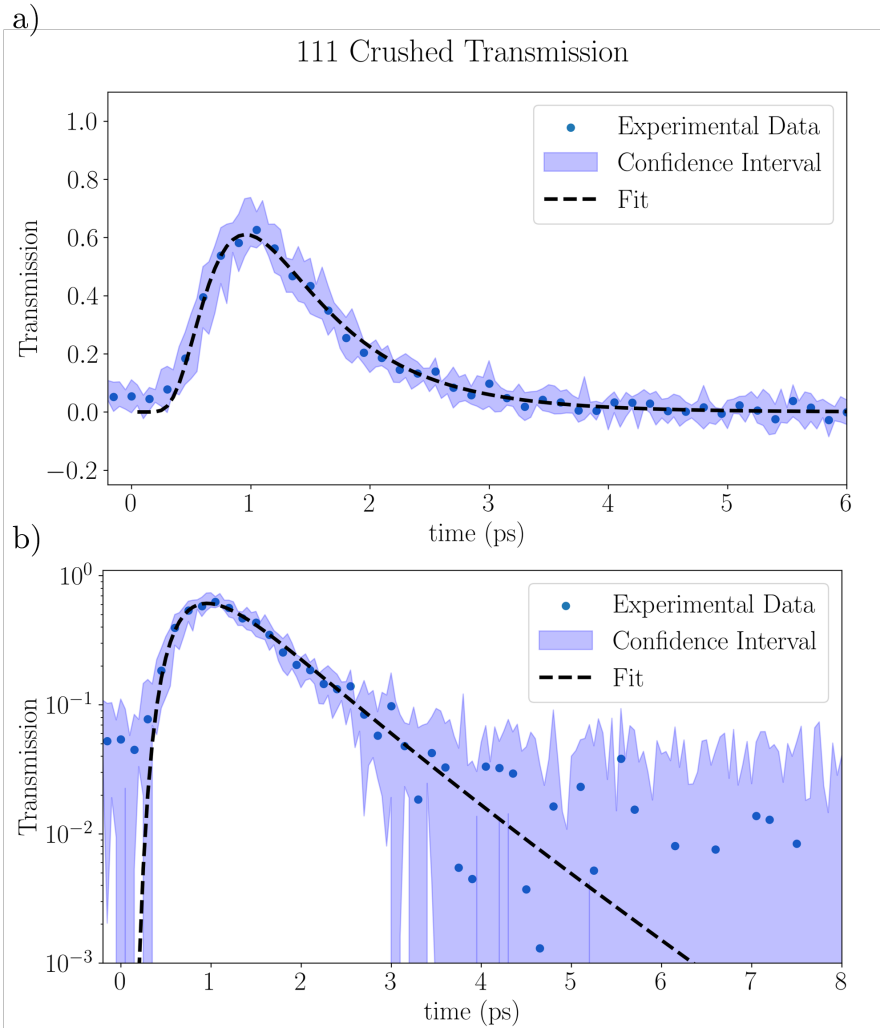

FIGURE 4.11: Time of Flight measurement for the 111 crushed nanowire sample at the central position ($r = 0\,\mu m$), shown on (a) a linear and (b) a logarithmic scale. Solid blue circles indicate a 3 point moving average to the data, corresponding to a $100\,fs$ window. Light blue shaded region shows the standard deviation across 8 different sample positions. Dashed black line shows the theoretical fit to the data with a diffusion constant of $D_z = 63 \pm 3\,m^2 s^{-1}$

.

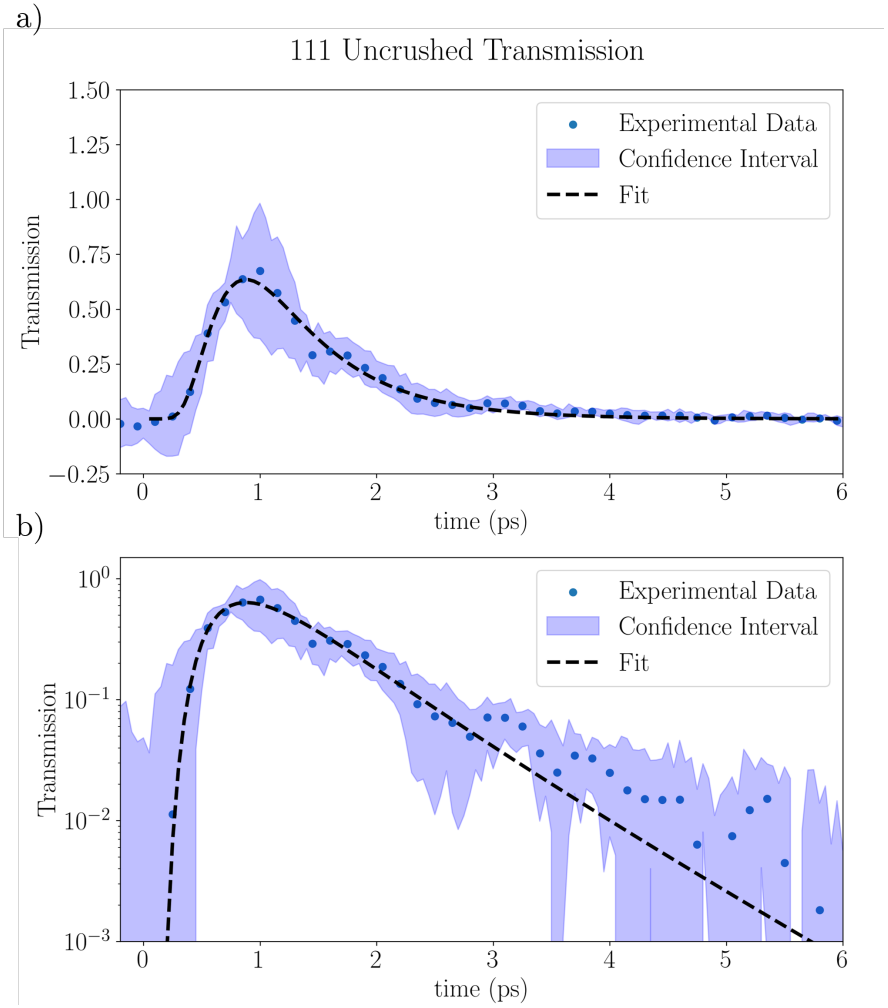

FIGURE 4.12: Time of Flight measurement for the 111 uncrushed nanowire sample at the central position ($r = 0\,\mu m$), shown on (a) a linear and (b) a logarithmic scale. Solid blue circles indicate a 3 point moving average to the data, corresponding to a 100 fs window. Light blue shaded region shows the standard deviation across 8 different sample positions. Dashed black line shows the theoretical fit to the data with a diffusion constant of $D_z = 72 \pm 2\,m^2 s^{-1}$

.

By carrying through the assumptions that only a small region ($D \approx 1\mu m$) is probed in a single spatial point by the pump at the exit surface, it can be inferred that the shorter time paths are measured more accurately, since longer paths have a greater chance to explore a wider range of the sample. In this case the diffusion along all dimensions would need to be accounted for, which is not well described by the analysis method employed. For this reason the measured values given here for D_z will need to be directly compared with the values measured simultaneously with the radial diffusion constant D_r in Section 4.4. The results of Section 4.3 are summarised in table 4.3.

4.4 Spatial Mapping and the Transverse Diffusion Constants

The pump probe measurement gives a four dimensional parameter space, as we measure the normalised change in transmission over time as a function of separation in both the x and y directions. In order to better visualise the data and reduce the effect of the background noise we will simplify the spatial coordinates (x, y) into radial separation, r, an example of which is shown in Figure 4.13.

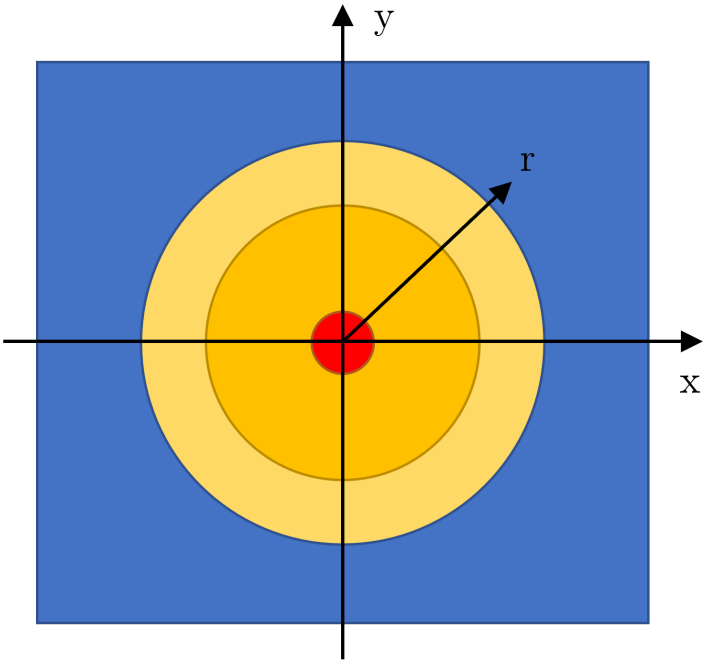

FIGURE 4.13: Example illustration of the pump probe measurement surface plot showing the measured separation r from the centre of the probe pulse, shown in red.

Although radially averaging the pump probe response allows the data to be depicted more succinctly and increases the accuracy of the longer time trails, it also means we are unable to differentiate the diffusion constants D_x and D_y. These too become averaged into a radial diffusion constant D_r, thus we lose any information on the anisotropy of the sample in the direction perpendicular to the light propagation.

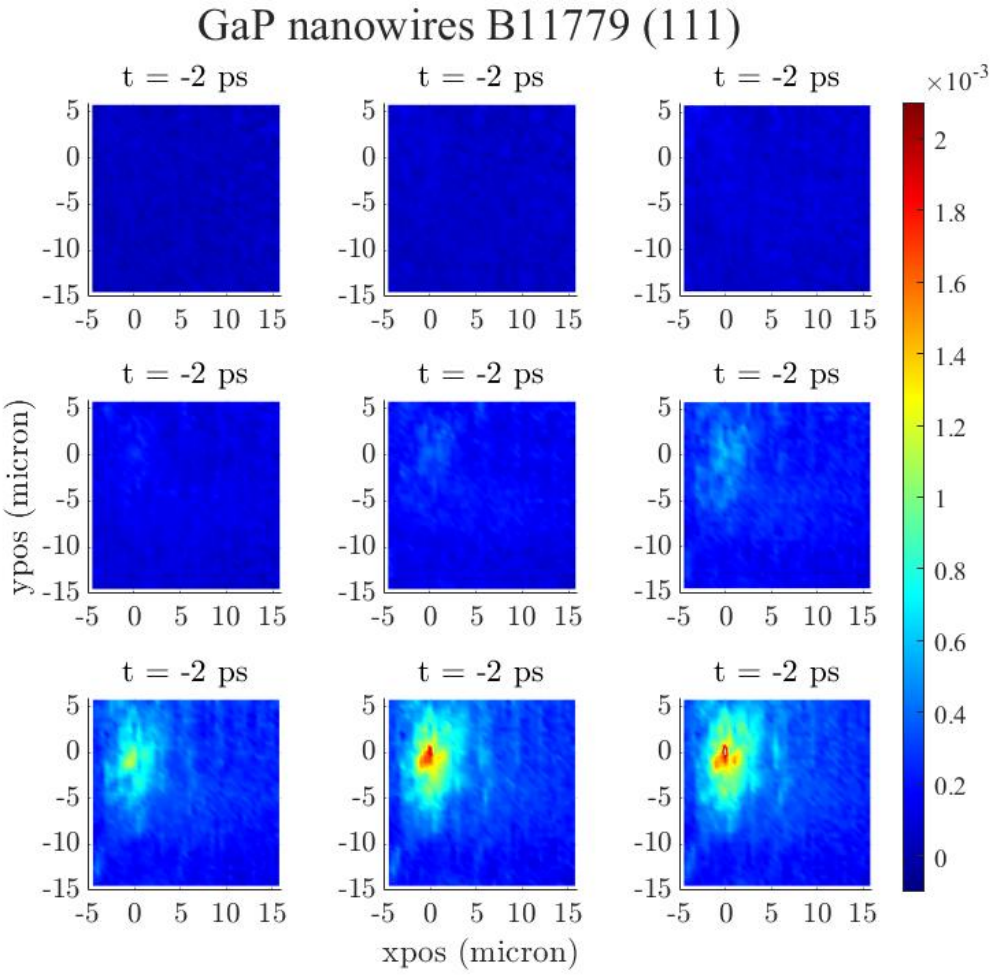

FIGURE 4.14: Measurements of the pump probe signal ($\Delta T/T$) (colour-scale) across the surface of a sample of GaP nanowires for a range of pump times t. The average background signal over all separations from time $t = -10$ to $-8\,ps$ has been subtracted. In the plot we see that the position of the centre of the peak measured intensity is taken as the origin of the incident probe pulse.

Several example surface plots are shown in Figure 4.14 for different time delays between the pump and probe. The plots give a sense of the shape of the probe at the exit face of the nanowires. Due to the detector being placed in the far field a speckle pattern can be observed, this is especially clear at large separations r and longer times. Through radial averaging, the effect of the speckle is somewhat diminished.

There are two approaches that can be taken to fitting the spatial mapping of the diffusion of the light. The temporal response measured in Section 4.3 giving the transmission diffusion constant, D_z, for each sample can be used as a fixed parameter in the diffuse transmission equation. In this case the transverse diffusion D_r is left as a variable parameter to fit the experimental data, alongside an amplitude coefficient, a.

The second approach leaves the diffusion constant D_z as a variable parameter in the fitting function. In both cases it is important that the time constant t_c, which was included in the previous measurement in Section 4.3 as a variable parameter, be kept as a constant between the two fitting method. To this end, a series of initial fits were run using a variable time constant, and a variable diffusion constant in both the transverse directions and the direction of transmission. The initial values for the time constant were then subtracted from the times to give $t = t - t_0 - t_c$, a value for the time which would allow for the fitting of the data without the time constant as a variable. This allows for the two fitting techniques to be used and compared without the relative shift in the absolute time causing unnecessary discrepancy.

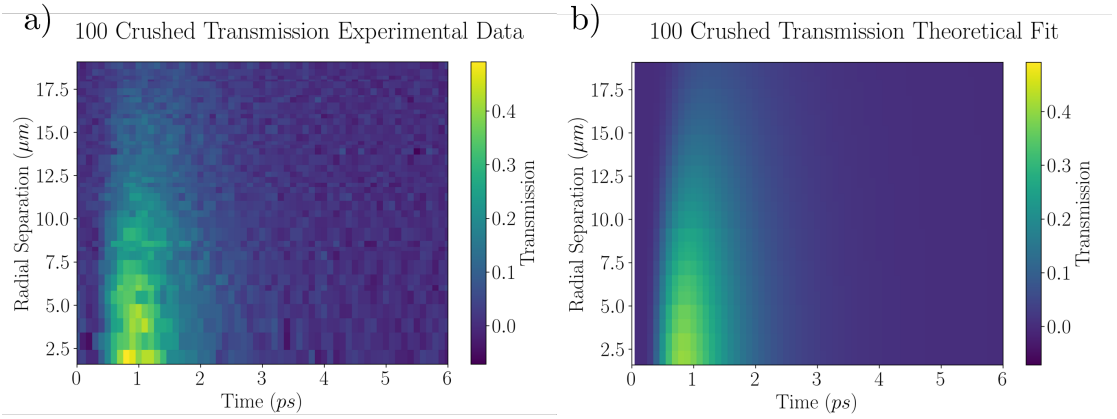

FIGURE 4.15: a) Transmission through the crushed 100 GaP nanowires as a function of both time, t, and radial separation from the source, r compared to b) theoretical fit from equation 4.1, giving diffusion constants D_z=74 m^2s^{-1} and D_r=44 m^2s^{-1}.

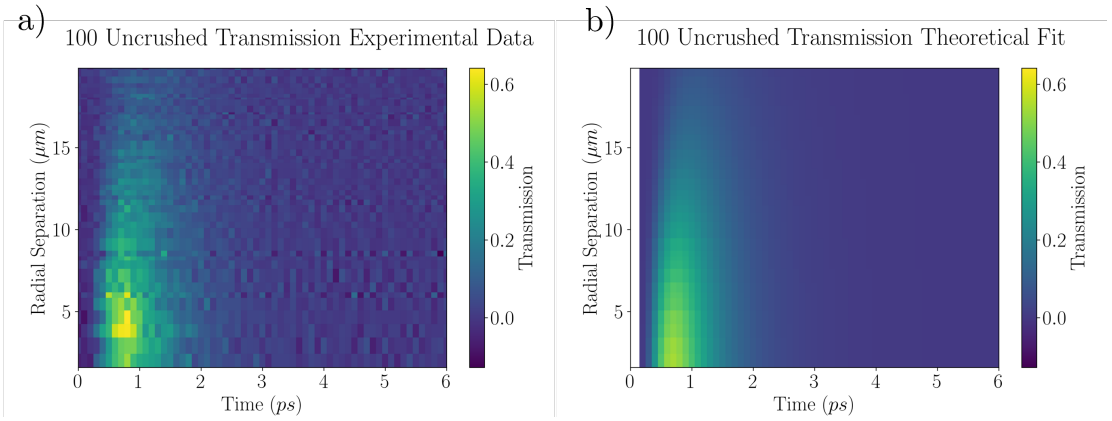

FIGURE 4.16: a) Transmission through the uncrushed 100 GaP nanowires as a function of both time, t, and radial separation from the source, r compared to b) theoretical fit from equation 4.1, giving diffusion constants D_z=87 m^2s^{-1} and D_r=56 m^2s^{-1}.

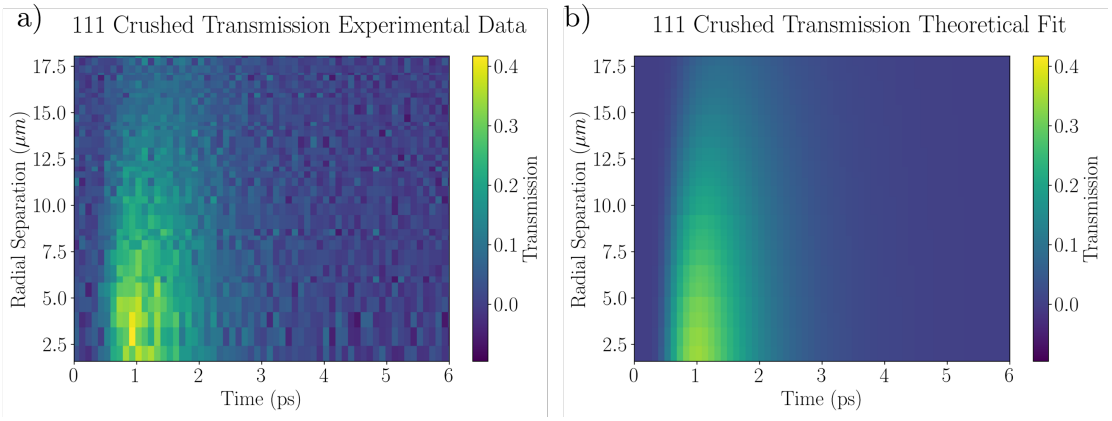

FIGURE 4.17: a) Transmission through the crushed 111 GaP nanowires as a function of both time, t, and radial separation from the source, r compared to b) theoretical fit from equation 4.1, giving diffusion constants D_z=65 m^2s^{-1} and D_r=44 m^2s^{-1}.

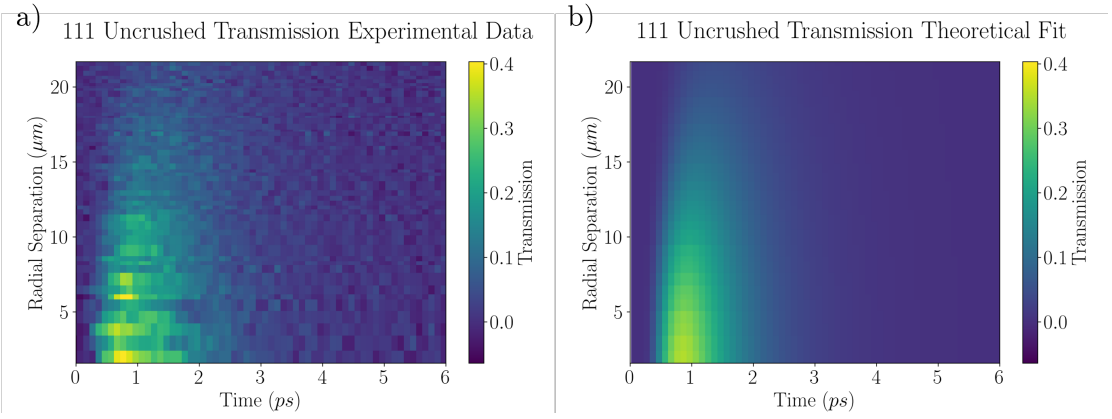

FIGURE 4.18: a) Transmission through the uncrushed 111 GaP nanowires as a function of both time, t, and radial separation from the source, r compared to b) theoretical fit from equation 4.1, giving diffusion constants D_z=69 m^2s^{-1} and D_r=50 m^2s^{-1}.

The figures 4.15-4.18 show the theoretical fits to the transmission at the back surface of the samples as a function of time and radial separation from the injection source. These are obtained using least squares fitting method to the equation 2.18. The fits shown utilise both D_z and D_r as variable parameters. There is little visible difference between the fits shown and the fits where D_z is fixed at the values measured in Section 4.3.

The residual of the pump probe experiment fit to theory are calculated as the subtraction of the theoretical fit from the data values, $r(x,y) = I(x,y)_{exp} - I(x,y)_{fit}$. The sum of squares of residuals is then simply

$$SS_{res} = \sum_{x,y} r(x,y)^2. \tag{4.2}$$

The total sum of squares from the experimental data is taken as sum of the variance of the values for each point,

$$SS_{tot} = \sum_{x,y} [I(x,y) - \bar{I}(x,y)]^2 \tag{4.3}$$

The R^2 coefficient of determination is then calculated as

$$R^2 = 1 - \frac{SS_{res}}{SS_{tot}}. \tag{4.4}$$

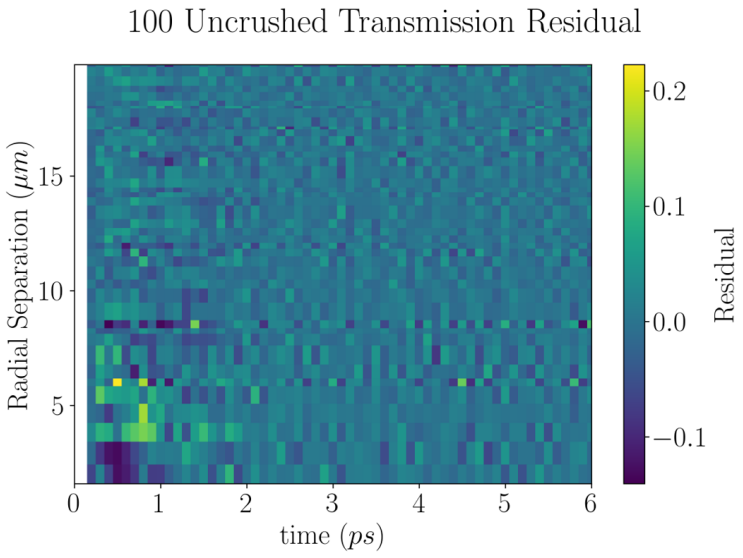

FIGURE 4.19: Residual plot for the 100 uncrushed GaP nanowire sample fit to the diffusion theory of propagation of light in disordered scattering media.

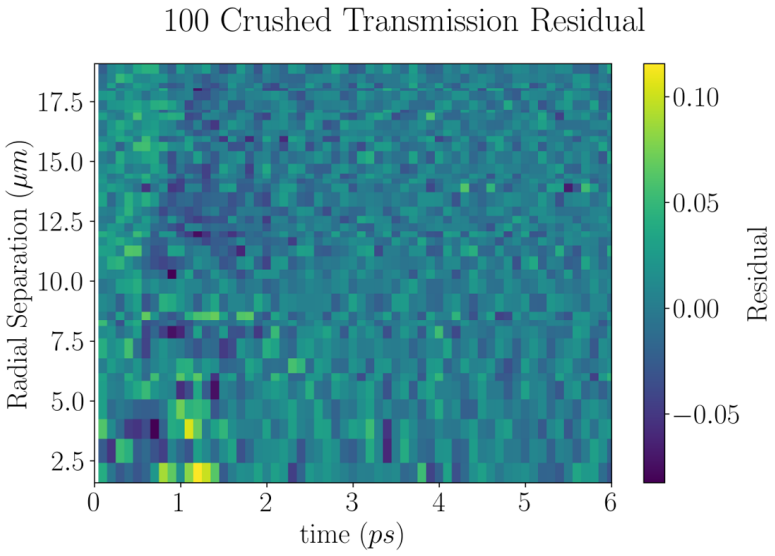

FIGURE 4.20: Residual plot for the 100 crushed GaP nanowire sample fit to the diffusion theory of propagation of light in disordered scattering media.

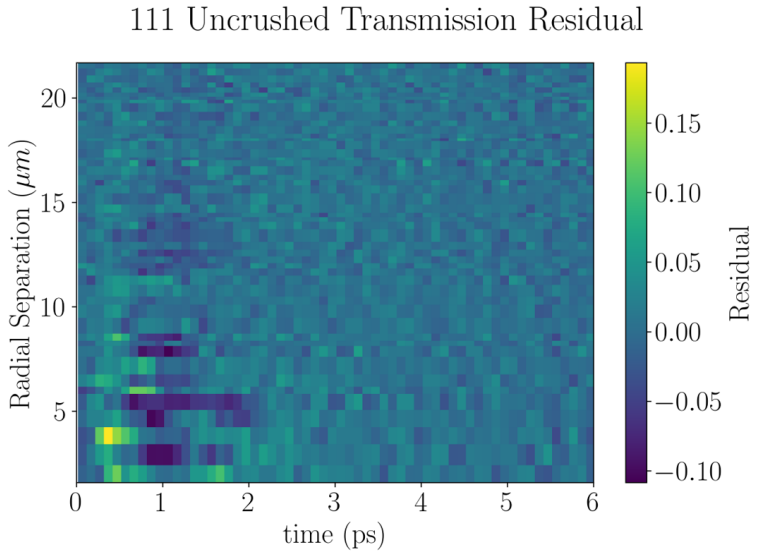

FIGURE 4.21: Residual plot for the 1 uncrushed GaP nanowire sample fit to the diffusion theory of propagation of light in disordered scattering media.

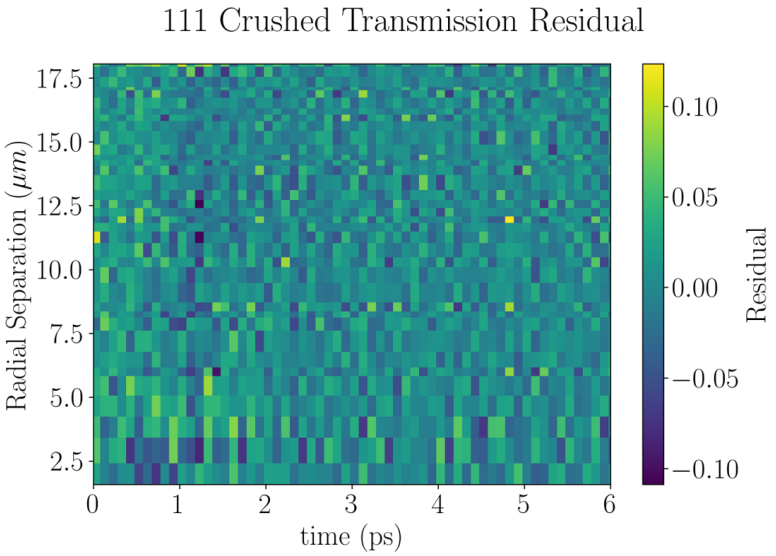

FIGURE 4.22: Residual plot for the 111 crushed GaP nanowire sample fit to the diffusion theory of propagation of light in disordered scattering media.

The residual plots show that across all the measured samples, there is a background noise contribution due to low speckle averaging. This is also seen in the higher intensity transmission period around $t \approx 1\,ns$, whereby the noise scales with the transmission intensity. This is similar to the results shown in the time trace measurements, however more statistical averaging would be required to determine with certainty whether this is solely due to limited speckle averaging or is an inherent experimental limitation.

Measured Diffusion Constants						
	Fixed D_z			Variable D_z		
Sample Name	D_z (m^2s^{-1})	D_r (m^2s^{-1})	R^2	D_z (m^2s^{-1})	D_r (m^2s^{-1})	R^2
100 Crushed	71 ±3	43	0.9	70	45	0.9
100 Unrushed	92 ±1	56	0.92	91	57	0.92
111 Crushed	63 ±3	43	0.9	67	44	0.91
111 Uncrushed	72 ±2	49	0.85	70	53	0.93

TABLE 4.3: Experimental D_z and D_r values obtained using the optical pump probe experiment. Associated errors due to the fitting procedure are presented for the D_z values measured using the single point time scans. R^2 values are given for the corresponding fits using both fixed and variable D_z values to indicate their relative accuracy.

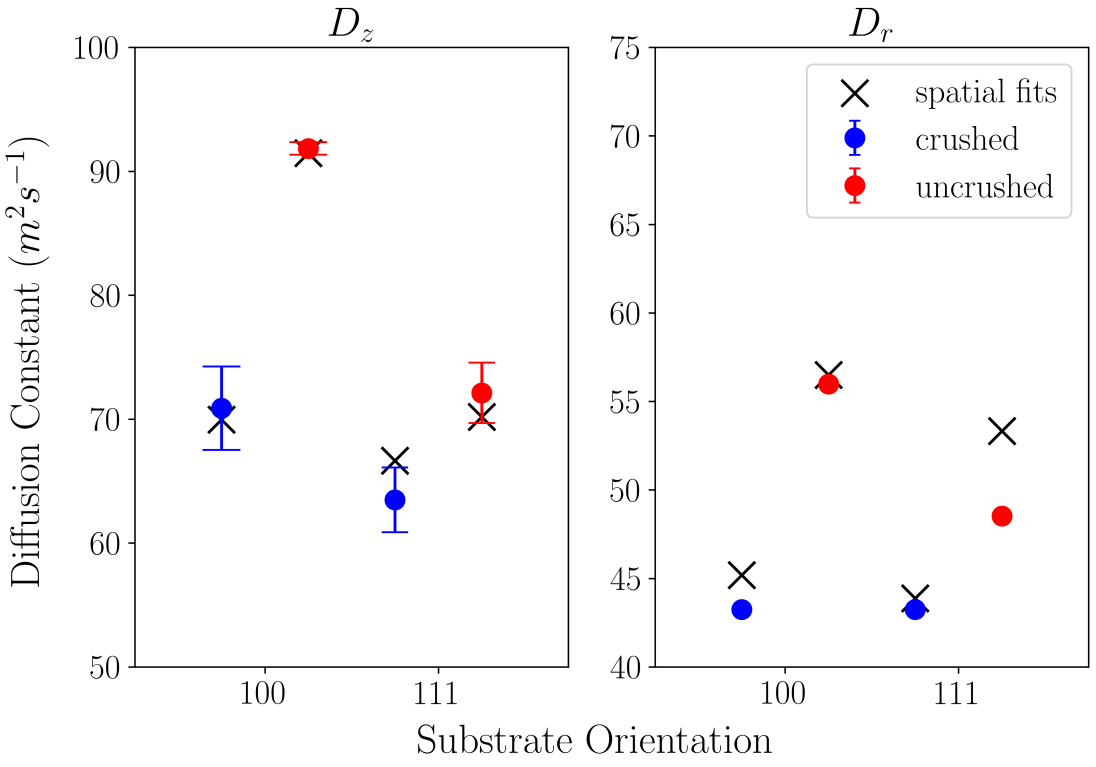

FIGURE 4.23: Summary of the diffusion constants, D_z and D_r, obtained using the fits to the transmission profiles of the 4 samples. Solid circles are results obtained using the single position scans at r = 0, with fixed values for D_z then used to obtain D_r from the spatial mapping. Crosses are fits obtained with both D_z and D_r as variable fitting parameters.

The fits shown in figures 4.15-4.18 yield the diffusion constants given in Table 4.3. The results are summarised in Figure 4.23 and show that for both substrates the diffusion constant decreases in both the direction of propagation and the transverse direction when the nanowires are crushed. It is not possible to compare the samples by substrate crystal lattice structure since the nanowire growth orientation is not consistent over

Sample Name	$\overline{D}$ fixed z ($m^2 s^{-1}$)	v_e/c
100 crushed	53 $\pm$3	0.53 $\pm$ 0.03
100 uncrushed	68 $\pm$1	0.68 $\pm$ 0.01
111 crushed	50 $\pm$3	0.50 $\pm$ 0.03
111 uncrushed	56 $\pm$2	0.58 $\pm$ 0.02

TABLE 4.4: Calculated energy transport velocity as a ratio of the speed of light, v_e/c, for the nanowire samples, showing a reduction in the energy transport velocity for the compressed nanowire mats. Values for the diffusion constant, $\overline{D}$, are calculated using the results in table 4.3. Energy transport velocities are calculated using the average of the two methods used to fit the pump probe data.

such long growth periods, and the exact geometries of the nanowires are not known for the measured sample locations. It is likely that some remnant of the structure exists since the diffusion constants are different for the two substrates before compression, but are the same after compression, within error. That said, without supporting information such as an optical cross-sectional image of the exact regions to identify the length, orientation, and thickness of the nanowires, or an independent measurement of the diffusion constants and transport mean free paths in both directions, it is not possible to state definitively that their disparity is caused solely by the orientation of the nanowires.

The anisotropy of the samples, measured D_z/D_r, is measured to be 1.65 ± 0.07, 1.65 ± 0.02 for the 100 crushed and uncrushed nanowires respectively, and 1.47 ± 0.07 and 1.47 ± 0.04 for the 111 crushed and uncrushed nanowires respectively. These results indicate that although the nanowire compression reduces the overall diffusion constant in both directions, the scattering strength appears to increase in both the longitudinal and the transverse directions.

Using equation 2.16 it is possible to calculate the energy transport velocity v_E of light within the sample using the measured diffusion constants and the isotropic transport mean free path, l_t measured in Section 3.4.2.

Comparing this result with previous studies of similar GaP nanowire structures (87)(11), shown in Figure 4.24, we see the diffusion constant we have measured and energy velocity we have calculated agrees well within the wavelength range probed in our experiments.

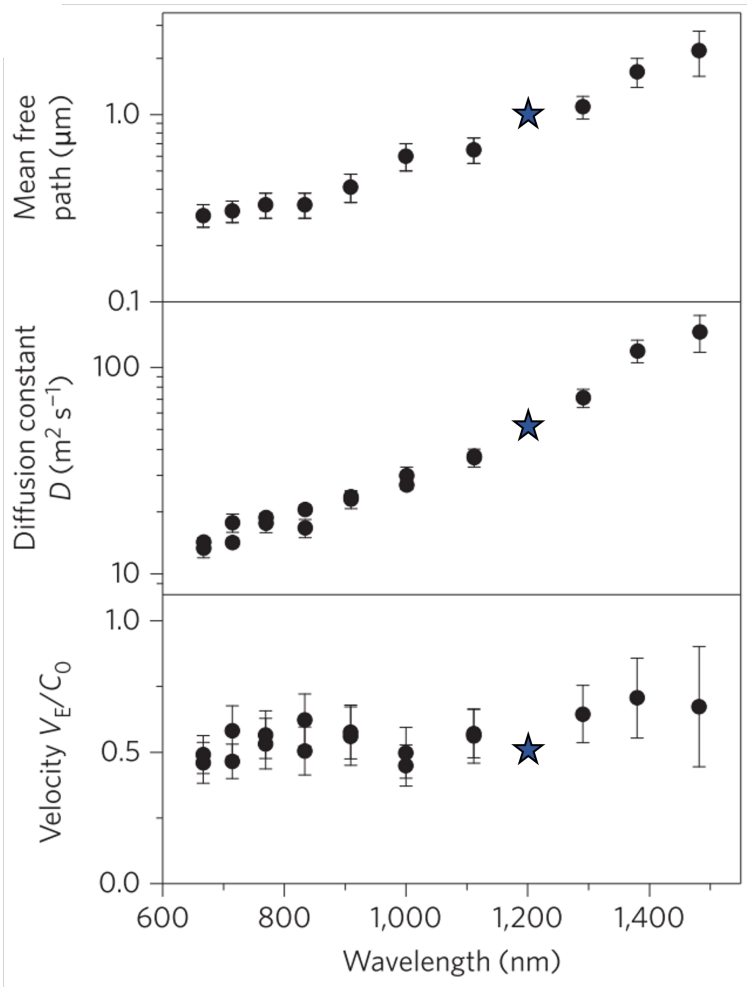

FIGURE 4.24: Previous results obtained for gallium phosphide nanowire slabs of thickness $L \approx 5\,\mu$m, showing the wavelength dependence of the transport mean free path, l_t, the diffusion constant through the slab, D (equivalent to D_z in our measurement) and the energy velocity, v_E. Figure reproduced from reference (11).

The results shown in Figure 4.24 are measured using short range correlation of the frequency speckle in the steady state, taken in a static transmission experiment(87). The static diffusion constant measured in this experiment is dependent upon the absorption of the sample in the detection region, as shown by (88). This is not the case for the dynamic diffusion constant measured in the time of flight optical pump probe experiment.

4.5 Conclusion

Utilising a new method of pump probe detection, anisotropic behaviour of strongly scattering materials has been measured. The effect of thermal background contribution to signal noise has been investigated and a number of mitigation techniques have been trialled. In summation these techniques led to a reduction in the signal to noise ratio and it was found that it was not necessary to implement these changes in the finalised experiment.

The spatial mapping of time of flight distributions of a number of samples has shown the diffusive model of light propagation to accurately describe the transport of light through these disordered nanowire samples, and results obtained agree with previous measurements made using independent methods. The reduction of the diffusion constant has been demonstrated under mechanical compression in both the transverse and longitudinal directions, resulting in a reduction of the energy transport velocity for all samples measured. The results of this experiment confirm that the ultra-fast pump probe technique can be used to differentiate the scattering strength of a material in the transverse and longitudinal directions, thus investigating the anisotropy of the scattering system. In slabs of isotropic strong scatterers it is predicted that strong localisation could manifest as the reduction of lateral expansion of the beam at the exit surface of the sample, thus the methods shown in this chapter present an opportunity for direct measurement of such a phenomenon. The system is applied to a semiconducting gallium phosphide nanowire mat however the process should be applicable wherever a significant transmission contrast can be incurred through photo-induced transient absorption.

The measurements shown would benefit significantly from further measurement of the speckle in a statistical averaging over several sample positions. This in combination with samples known to be asymmetrical in the orthogonal transverse directions would allow a separation of D_r into D_x and D_y. This would be especially useful if a characterisation of the vector dependence of $\mathbf{l_t}$ could be established, allowing a full description of the energy transport velocity in all dimensions. This experiment could therefore be combined with interferometric and spectroscopic measurements to help characterise the localisation band edge in three dimensional photonic materials, exploring the deviation from the diffusive regime.

Chapter 5

Time Reverse Optical Memory Effect

5.1 Introduction

This chapter aims to develop an experimental investigation of the phase dependence of the time reverse optical memory effect. The optical memory effect refers to the correlation of an output speckle when undergoing a small change in angle or position of incidence, or in it's spectral frequency. In a geometry in which two counter propagating waves would be Lorentz-reciprocal (i.e. symmetric under time reversal), there is a contribution to the correlation which is termed the time reverse optical memory effect.

The motivation for this investigation arises from previous works which used a Sagnac interferometer geometry to detect the three dimensional spatial information of a target object through a multiply scattering medium. Seemingly opaque scattering medium, such as rain, fog, bodily tissue or clouds, present significant environmental challenges for object detection and imaging. The system produced in reference (89) utilises the phase conservation under multiple scattering, and fast scanning of both beams of a Sagnac interferometer, to measure the round trip path length across a number of points thus mapping the spatial extent and depth profile of the target. We aimed to develop this process to incorporate direct measurement of the time of flight of a pulsed light source using a single photon counting detection method which would enable a large increase in the detection efficiency. This led to the question of the phase stability of the spatial speckle correlation function under multiple scattering in the time reverse optical memory effect. In the time reverse geometry, the counter-propagating beams produce mirrored speckle patterns which retain their phase information from prior to the multiple scattering process. This may be exploited to produce a target specific signal which is stable under small perturbations to the environment which may result in changes to the relative phase of the time reverse beams.

The experiments included within this chapter are associated with work which was completed working as part of an external project, the nature of which is sensitive. It is therefor noted that some of the aspects of the research, such as possible applications or avenues of investigation were omitted in the interest of discretion and security.

Initial measurements aim to confirm the previous results of effective ranging of a target signal in a time reverse geometry through a multiply scattering medium using phase modulation in a fiberised pulsed system. This is then translated to a free space pulsed optical regime which demonstrates the principle in a time of flight sensitive measurement. A more thorough experimental investigation is then carried out using a free space optical set up, in which the speckles of the two beams of the Sagnac interferometer are measured independently, and then combined in a Mach-Zehnder interferometer in order to characterise the phase dependence of the system.

5.2 Phase Modulation of the Sagnac Interferometer for Non-Line of Sight Detection and Ranging

5.2.1 Fiberised Pulsed Laser Source Experimental Set Up

The experiment comprises a modified Sagnac interferometer which utilises a Mach-Zehnder interferometer in the detection of the counter-propagating beams. A continuous wave telecom laser pumps a 1 Watt Er-doped optical fibre amplifier, resulting in a 1550nm wavelength fiberised laser output of variable intensity. This fibre is first passed through a high-power faraday isolator to prevent any damaging back reflections from reaching the OFA. The beam is then split using a 75:25 fiberised splitter and the 25% output is passed through the electro-optic modulator.

Both beams are then projected using graded-index collimator outputs (OZ optics), transmitted through polarising beam splitters (PBS), where half-wave plates ($\lambda/2$) are used to optimise transmission through the beam splitters. The beams follow a common path through two telecom-grade quarter-wave plates ($\lambda/4$), which are aligned to rotate the polarisation by 90 degrees over a full roundtrip.

An oscillating phase modulation is introduced in the common path of the interferometer using an electro-optical modulator (EOM), creating a beat frequency due to constructive and deconstructive interference of the clockwise and anticlockwise beams at the detector. The frequency of the phase modulation may be swept using a driving voltage with variable frequency. A characteristic intensity modulation at a frequency corresponding to the round trip time of flight can be measured to indicate the time of flight of the detected signal.

The return signals are then reflected by the PBS. An arrangement using a non-polarising beam splitter (BS) is used to combine the beams and produce an interferometric signal onto an InGaAs SWIR camera and the resulting images are analysed on a PC workstation.

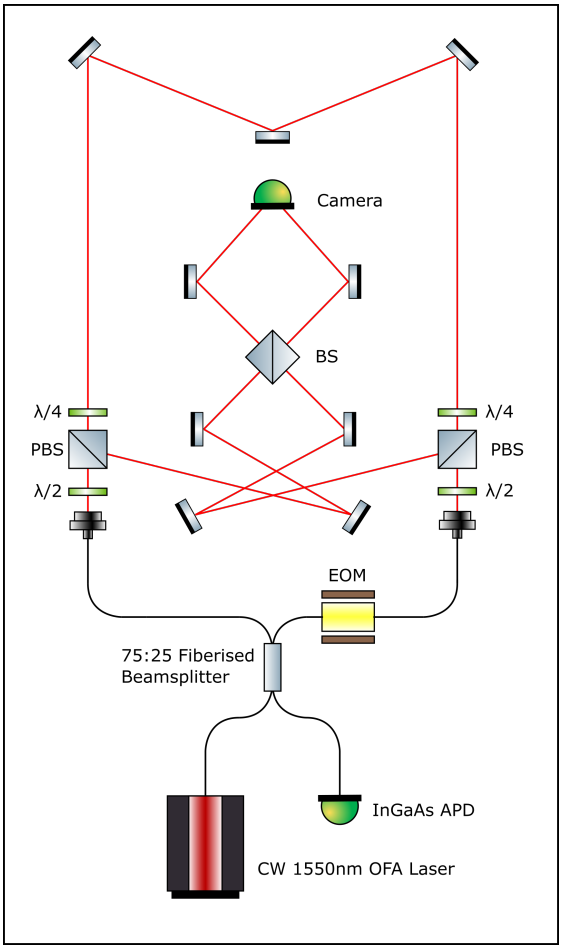

FIGURE 5.1: A continuous wave telecom laser is used to pump an optical fibre amplifier (OFA) to produce a 1550 nm laser output. A Faraday isolator (not shown) is used to prevent back-reflection into the fibre. A 75:25 beamsplitter divides the intensity along two output fibres. one of which passes through an electro-optical modulator (EOM). This is driven by a varying voltage output from a Zurich Instruments UHFLI600 Lock-in amplifier. The two beams are output using graded-index (GRIN) collimator outputs. Half-wave plates ($\lambda/2$) are used to optimise transmission through two polarising beam splitters (PBS). These then form a polarised Sagnac interferometer. Collection is facilitated through two quarter-wave plates ($\lambda/4$) which rotate the polarisation of the two beams by 90 degrees, allowing them to be reflected by the two PBS. The quarter wave plates may be removed to enable transmission at the PBS. The return signal as collected through the optical fibre is measured using an InGaAs infrared high frequency APD detector. The signal is passed to the lock in amplifier for demodulation with the driving frequency of the EOM.

5.2.2 Experimental Determination of the Round Trip Time Using Phase Modulation

Utilising the fiberised system, as shown in Figure 5.1, a measurement of the Round trip time is made by sweeping the frequency of the AC voltage supplied to the EOM. Interference between the two paths of the Sagnac interferometer is then detected using the InGaAs APD by demodulating the signal using a lock-in amplifier with the reference signal being equal to that supplied to the EOM. The EOM induces a π radians phase shift in both arms of the interferometer. The detected signal is modulated by the relative phase difference of the two paths at the detector, which is determined by the round trip time.

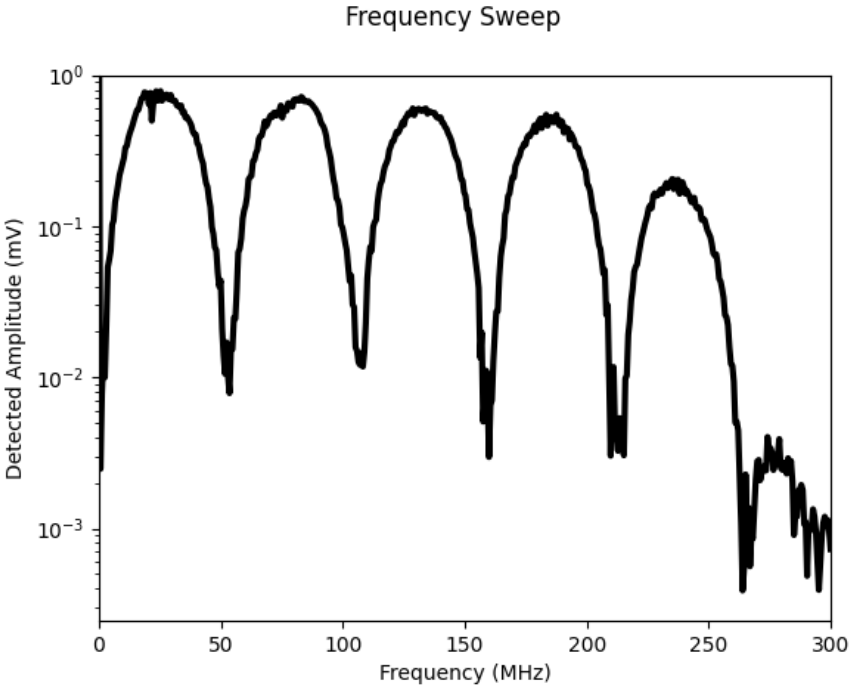

FIGURE 5.2: Frequency sweep of the EOM and lock-in detection frequency in the fiberised continuous wave set up, showing the round trip time of the set up of 18 ns without scattering medium, corresponding to a 5.4 m round trip distance.

The result presented in Figure 5.2 shows the round trip time of the common paths of 18 ns without scattering medium, corresponding to a 5.4 m round trip distance. This is inclusive of the length of the optical fibres used in the detection system, which is commonly known. These results demonstrate the use of phase modulation and interference in the continuous wave Sagnac interferometer to determine the range from the system to the object of interest and repeat results presented in reference (89).

5.3 Single Photon Counting and Time of Flight Detection

5.3.1 Free Space Pulsed Laser Source Experimental Set Up

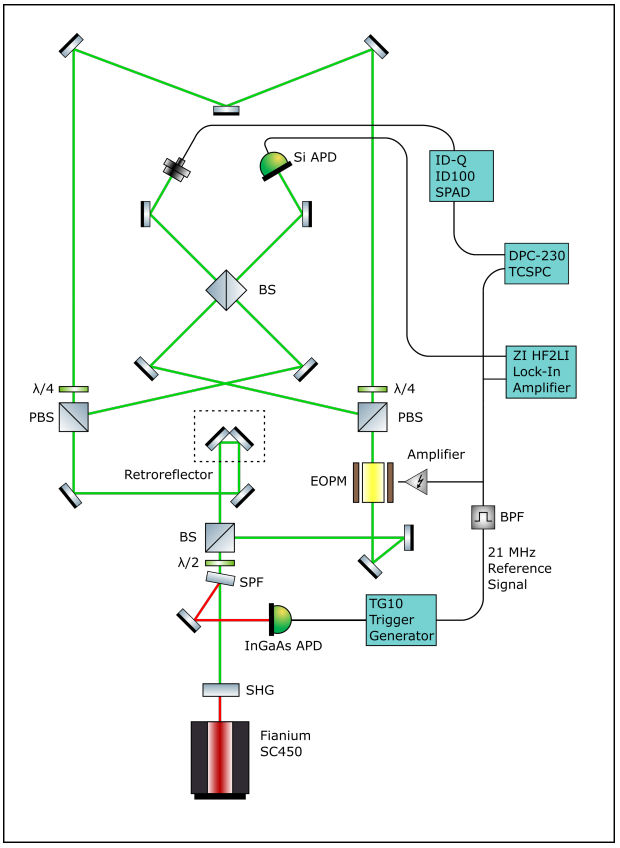

FIGURE 5.3: A Fianium SC450 pulsed laser source outputs a 1064 nm picosecond source. This is passed through a second harmonic generation (SHG) crystal to produce a frequency doubled 532 nm pulsed laser beam. A short pass filter is used to isolate the visible pulses and the reflected infrared pulses are measured using a high frequency InGaAs APD. This is passed to a trigger generator which produces a phase locked output voltage at double the laser output frequency. This is passed through a 21 MHz band pass filter (BPF) before being amplified in order to to drive a free space electro-optical modulator (EOM). The 42 MHz visible laser pulse train is then split using a non-polarising beam splitter before polarising beam splitters (PBS) to form a polarised Sagnac interferometer. Collection is facilitated through two quarter-wave plates ($\lambda/4$) which rotate the polarisation of the two beams by 90 degrees, allowing them to be reflected by the two PBS. They are then recombined to form a Mac-Zehnder interferometer in the detection arm. One of the detection arms is measured using an ID-Q ID100 single photon avalanche photodiode (SPAD). A single photon counting data acquisition card (TCSPC) is used to measure the output from the SPAD, using the frequency doubled trigger generator as the phase locked reference. The second arm uses a high frequency silicon APD. The photodiode output is passed to a Zurich Instruments UHFLI600 lock in amplifier for demodulation, utilising the same 21 MHz reference to detect the signal.

The single photon counting measurement uses a 42 MHz pulsed 1064nm picosecond light source and a SHG crystal to produce a 532nm visible pulse train. This is passed

through a 950nm short pass filter and the reflected 1064nm beam is used to trigger the Eksma TG10 Trigger Generator using an InGaAs APD detector. The TG10 trigger generator acts as a phase locked frequency divider outputting a 21MHz pulse train.

The frequency doubled trigger signal is passed through a 20-22 MHz band pass filter which converts this pulse train into a clean sinusoidal wave which is then used as the reference for both the lock-in amplifier and the Becker & Hickl DPC-230 single photon data acquisition card, as well as the driving voltage for the EOM. An electronic amplifier is used to control the voltage applied to the EOM which modulates one arm of the interferometer, changing the phase of every other pulse by 180°.

For pulses from the two arms to interfere they must be superposed in both space and time, therefore a micrometre travelling stage and retroreflector are used to ensure the path length of both arms of the interferometer are the same. Upon recombination at the final beam splitter, one beam is incident on a Si APD detector and this signal is relayed to the lock-in for demodulation, again using the trigger signal as a frequency matched reference.

The second detection arm is collected by an optical fibre and passed to the IDQ SPAD which allows for single photon detection. Quarter and half waveplates are used as before to optimise transmission and reflection at each of the polarising beam splitters.

To detect the interference of the pulses, the two paths must be of exactly the same length in order to arrive on the detector within a narrow time window set by the pulse duration. For the 12 ps pulsed laser, path lengths need to be matched to within a few millimetres. Note that this is only necessary for the paths that are not included in the Sagnac loop, as any path length within the polarizing beam splitters are by default exactly compensated. This is accounted for using the retroreflector shown in Figure 5.3.

5.3.2 Time of Flight Measurement of Speckle Interference in a Sagnac Interferometer Geometry

In this Section, experimental demonstration of the preservation of phase in the application of time of flight measurement detection to the time reverse interferometry geometry are shown using a single photon counting detector with a high resolution time binning acquisition card. Simultaneously, a lock-in detection apparatus is used to measure the target signal and the unmodulated laser source amplitude to examine signal stability over longer detection times.

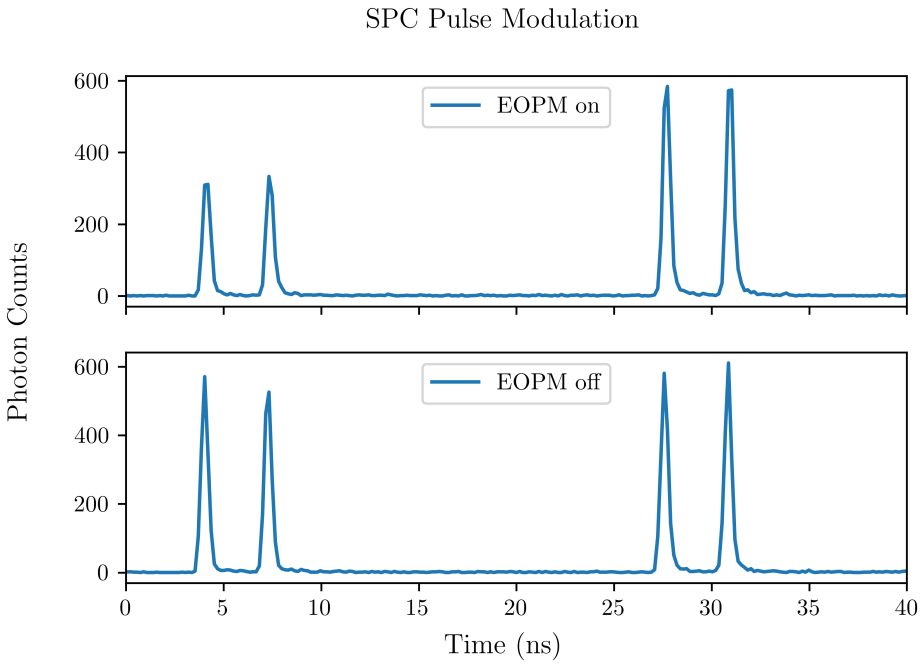

FIGURE 5.4: Time resolved demonstration of the pulse modulation in the reciprocal geometry caused by a change in phase of one arm of the Sagnac interferometer. The deconstructive interference caused by the flipping of the phase of one arm of the interferometer is realised at the zero order DC component of the spatial distribution of the reflected light, due to focusing into the optical collection fibre. An *iD-Q 1000* single photon detector is used to measure the intensity. A target signal and a spurious repetition of the signal is observed.

Modulation of the detected signal in the Mach-Zehnder geometry is shown in Figure 5.4. The focusing of the reflected light onto a collection fibre aperture isolates the zero order of the spatial component of the signal, or in the spatial frequency domain, the DC component. The time of flight of a single round trip is given by the time trace, measured against a reference pulse, giving a round trip distance of $\sim 1.35\,m$ for the target signal. The reference pulse is generated using second harmonic generation and is used to synchronise an electronic trigger generator. The electronic trigger is passed through a 21 MHz band pass filter to halve the frequency. This is then passed as a reference to the EOPM, the lock-in amplifier, and to a *DPC-230 TCSPC* photon correlating module.

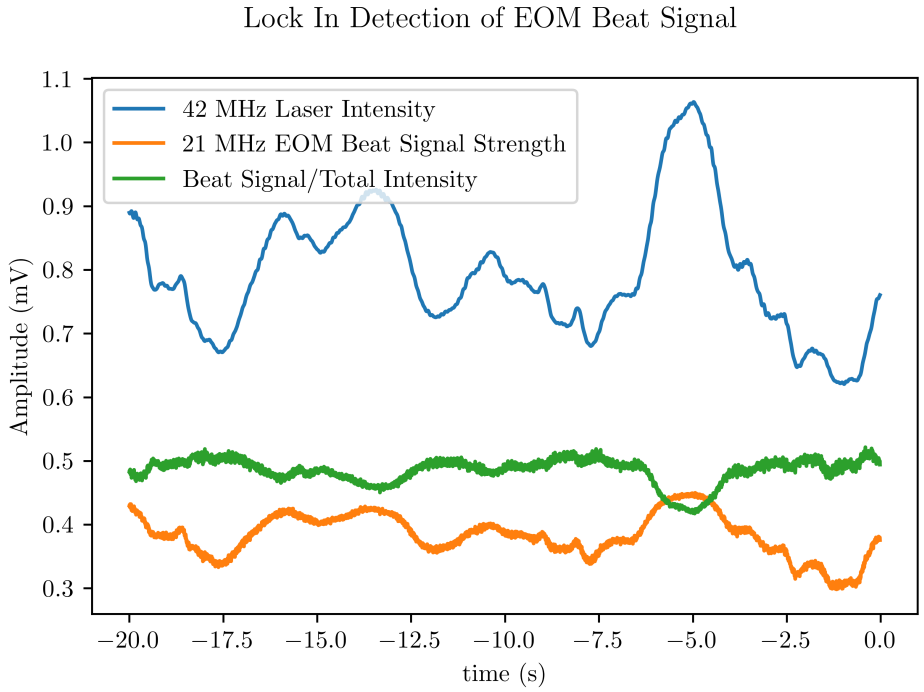

FIGURE 5.5: Lock-In detected signal demodulated from the reflection gathered using the time reverse geometry. The lower harmonic, EOM modulated beat signal strength (orange) is shown to oscillate with the laser intensity (blue). The normalised signal is shown in green.

The lock-in detected signal over a period of time is shown in Figure 5.5. The 42 MHz laser pulse intensity is shown to oscillate strongly over the measurement period of 20 s. Normalising the detected signal to this fluctuation increases signal stability. These changes in the detected intensity are common in real world environments such as body tissue, where motion of the sample may cause rapid de-phasing along the time-reverse path caused by changes in the refractive index. This methodology which makes use of the time reversal symmetry of the system, in conjunction with the active control of the phase shown in the later Sections, could enable improvements to the signal strength and stability in future measurements, as well as opening the door to quantum statistical measurements, if the photon counting detection limit can be brought down to single photon events.

5.4 Phase Dependence of the Spatial Correlation Function in the Time Reverse Optical Memory Effect

5.4.1 Free Space Continuous Wave TRME Experimental Set Up

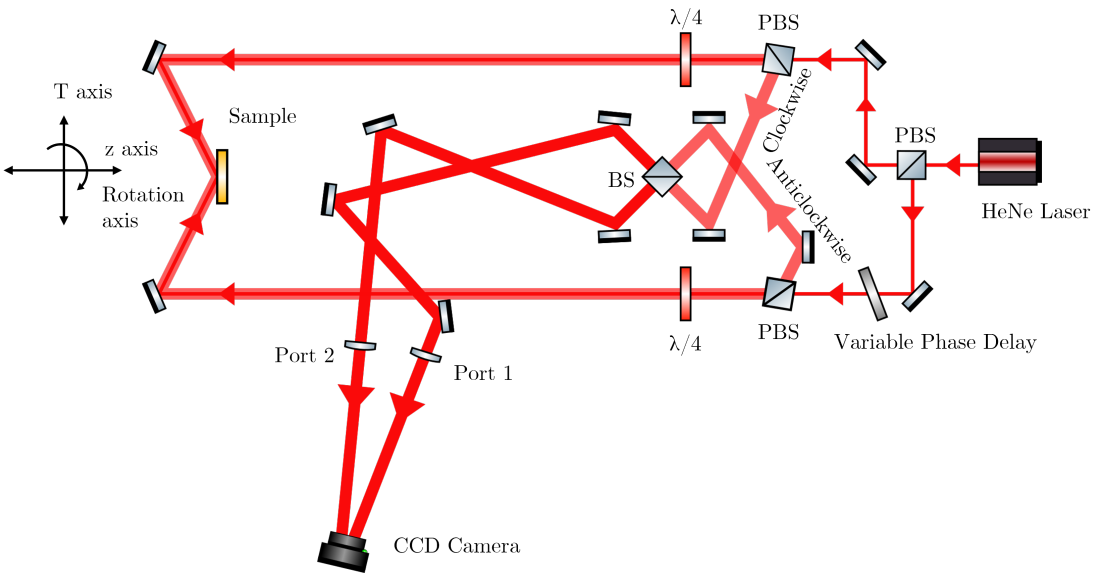

FIGURE 5.6: Experimental set up for measuring the phase dependence in the time reversal memory effect. A continuous wave HeNe laser output is separated into two beams using a polarising beam splitter (PBS). These two beams, denoted as clockwise and anticlockwise, form a Sagnac interferometer with a scattering sample in the common path. A phase delay is introduced into the clockwise beam before entering the common path, inducing a phase delay relative to the anticlockwise beam. The speckle produced is collected through polarisation selection using quarter wave plates ($\lambda/4$) and a pair of PBS. The beams are then recombined using a non-polarising beam splitter (BS) to form a Mach-Zehnder interferometer in the detection path. Extra bounces are introduced into the anticlockwise beam in order to align the speckles at recombination, and again for detection. Images are formed on a visible camera (CCD) by focusing using two 7.5 *cm* lenses. The axis of sample translation (T), displacement (z), and rotation (Rotation) are shown.

The experimental set up for the measurement of the optical memory effect comprised of a 633 nm HeNe laser used in a modified Sagnac interferometer geometry. The laser output is passed through an optical isolator (not shown in Figure 5.6) and a polarising beam splitter (PBS), which separates the beam into the horizontally and vertically polarised components. One of the beams is passed through a half waveplate, in order to rotate its polarisation 90 degrees; and a thin glass coverslip, which is removable for measurements which are insensitive to the relative phase of the beams. The beams are then each passed through a second PBS, aligned to transmit the beam. Each beam then passes through a quarter waveplate which is aligned at 45 degrees to the angle of polarisation of the beam, resulting in circularly polarised light.

Both beams are incident on the same point on the sample and the scattered light (or reflected, in the case of an alignment mirror) then follows the same return path as the beam travelling in the opposite direction. After passing through the second quarter waveplate, each beam returns to linear polarisation at an angle 90 degrees to its initial state. This allows it to be reflected at the PBS, instead of being transmitted back towards the laser source. upon returning to the PBS, the two beams are mirrors of each other. To accommodate this the clockwise beam is then reflected using an extra mirror.

The two input beams are recombined (spatially overlapped) using a non-polarising beam splitter into two mixed output signals which are detected on a CCD camera, in the same way as a Mach-Zehnder interferometer. The separate beams follow a shared path and it is therefore intuitive to describe these as clockwise and anticlockwise beams (as shown in Figure 5.6).

In the reflection geometry where the speckle produced by two scattered wavefronts are correlated due to the time reverse optical memory effect, the distribution of intensities as seen in the far field are mirror images of each other. If the speckles were to be recombined as in a Mach-Zehnder interferometric system, the speckles could be overlapped by introducing an extra reflection in one of the detection paths, and not the other. When recombined using a standard beam splitter, there is a π radians phase shift along the reflected path, this leads to the constructive and deconstructive interference seen along the two arms.

The output beams are spatially separated on the CCD camera, allowing the direct measurement of both outputs simultaneously, and minimising detection defects and aberrations that may come from using two cameras, but unfortunately reducing the image resolution for each beam. These are labelled as Port 1 and Port 2 to differentiate them. As in the case of the paths of the interferometer, the two outputs are mirrored and so for ease of analysis, an extra reflection is again introduced for one of the outputs. After recombination, both of the outputs (port 1 and port 2) are composed of both the clockwise and anticlockwise beams. The difference in the relative phase between the clockwise and anticlockwise beams in port 1 and port 2 is π radians due to the reflection during recombination. This leads to the intensities of port 1 and port 2 being anticorrelated. The angle of incidence of the light relative to the normal to the surface of the sample in the time reverse geometry is measured to be 54°, equivalent to 0.946 radians.

5.4.2 Wavefront Alignment and Speckle Interferometry

Using an alignment mirror instead of a scattering sample in the beam path produces Gaussian laser spots on the CCD output. By rotating the non polarising beamsplitter, the reflected and transmitted beam outputs may be separated spatially on the CCD as shown in Figure 5.7.

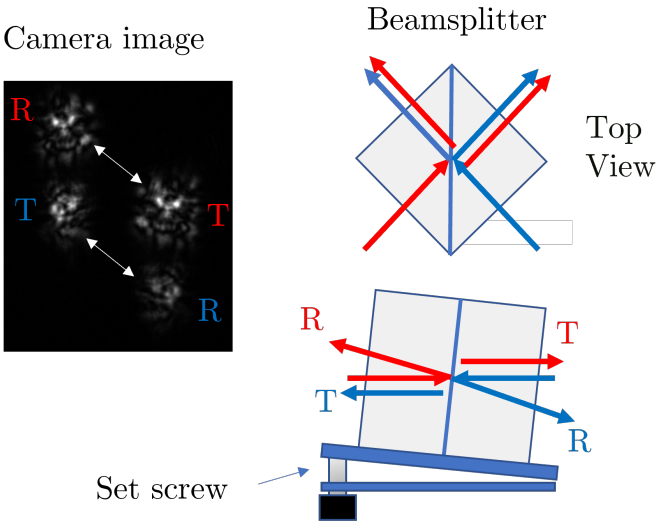

FIGURE 5.7: An example image of speckle patterns measured in the Mach-Zehnder interferometer when spatially separated due to the tilting of the beam splitter. This method can be used in alignment to identify regions of correlated speckle, thus indicating the time reverse geometry. NB the images shown do not exhibit a correlation, they are for demonstration only.

Through careful alignment it is possible to observe the interference of the recombined beams in both ports, and overlap them such that they are co-propagating and the wavefronts are coplanar, resulting in an "on-off" configuration where the intensities of the spots are anticorrelated. The interference signal at the Mach-Zehnder interferometer detection arms can also be altered, as shown in Section 5.4.7, using the phase modulation of one arm of the Sagnac interferometer to induce a phase shift in the two paths relative to one another.

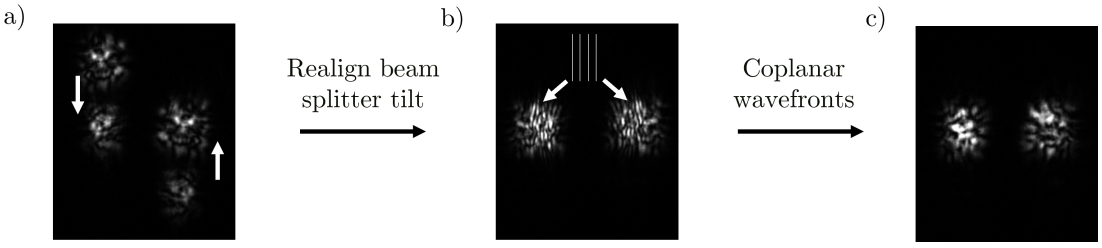

FIGURE 5.8: Measured speckles showing interference caused by a misalignment of the wavefronts. The interference is overlayed with the speckle intensity, in this case along the vertical axis.

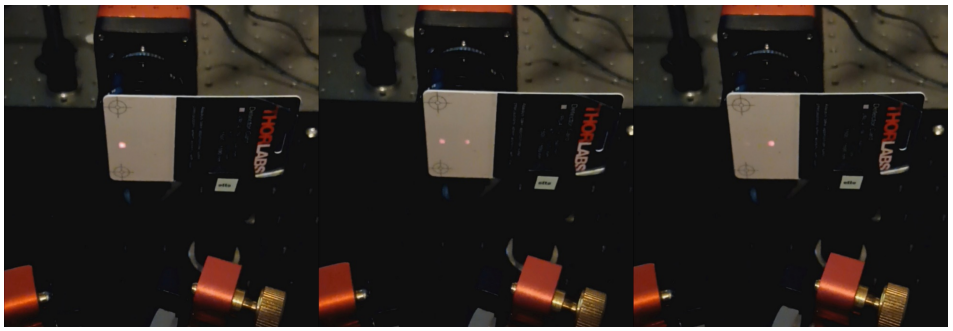

FIGURE 5.9: Illustration of the alignment of the wavefronts in the time-reverse geometry leading to constructive and deconstructive interference in the Mach-Zehnder interferometer geometry. The anti-correlated intensity in the two arms of the interferometer is preserved under multiple scattering. As the relative phase between the clockwise and anticlockwise beam paths changes, the intensity shifts from one output port to the other (shown in optical images from left to right).

The scattering sample investigated in the following Sections is a *Thorlabs NBK-7* 1500 grit optical diffuse reflector. This is a ground glass, silver coated optical diffuser with a substrate thickness of 2 mm and a reflectivity of unpolarised light of $\approx 96\%$ at 633 nm.

5.4.3 Speckle Patterns and the Spatial Correlation Function

The speckle pattern as discussed in this chapter refers to the far field image of an angular distribution of intensities produced by scattering of light from a disordered sample. The image of the speckle is generally measured over a limited aperture. Pixelation of the speckle pattern separates the intensity into small finite Sections, generally this is much smaller than the individual speckle as seen in Figure 5.10.

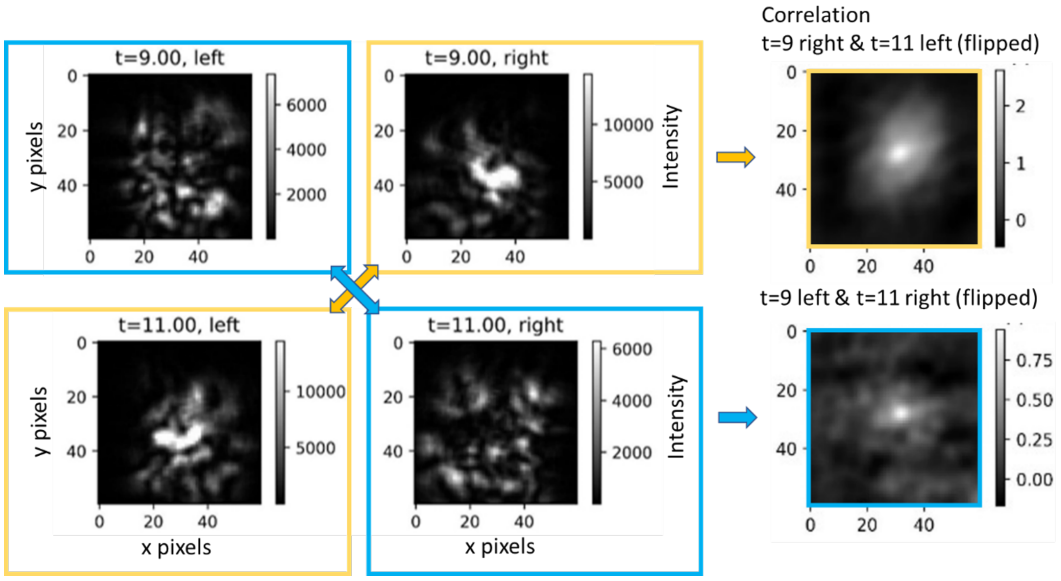

FIGURE 5.10: Example images of the speckle pattern of intensities and the cross correlation between them. Two different beams exhibiting time reversal symmetry are shown (left and right) for two different realisations of the speckle. In this case the phase shift between the two realisations is π radians. The cross correlation between the left and right images when they exhibit the same speckle is shown and exhibits a peak due to the time reverse optical memory effect.

The cross correlation between two 2-dimensional images can be simplistically described as how similar they appear. It is measured as the convolution of the images normalised to the product of the average of their intensities and as such the correlation function itself is a function of the same dimensionality of the initial images. An example of the speckle pattern and their convolution is shown in Figure 5.10.

The calculation of the cross correlation between two 2-dimensional intensity speckle patterns, $I_1(x,y)$ and $I_2(x,y)$, is calculated as:

$$C_{12} = \frac{\delta I_1 * \delta I_2}{\langle I_1 \rangle \langle I_2 \rangle}, \tag{5.1}$$

where

$$\begin{aligned} \delta I_1 &= I_1(x,y) - \langle I_1 \rangle, \\ \delta I_2 &= I_2(x,y) - \langle I_2 \rangle. \end{aligned} \tag{5.2}$$

The ensemble average of the intensity distribution is measured as the mean of several speckle patterns, denoted by $\langle I \rangle$. This is then subtracted from the given intensities of the two speckle images to be measured (equation 5.2). The convolution is then taken of the subtracted intensity speckle patterns, δI_1 and δI_2. In order to expedite this calculation, the convolution theorem is used. The speckle patterns undergo a two dimensional

fast Fourier transform (FFT) to produce the spectral intensity distribution, and the conjugate is taken of one of the two transforms:

$$\delta I(x,y) \xrightarrow{\mathcal{F}} \delta I(k_x,k_y) \tag{5.3}$$

It is then possible to take the correlation of the two images by calculating the inverse Fourier transform of their product.

$$C_{12}(x,y) = \frac{\mathcal{F}^{-1}\{\delta I_1(k_x,k_y)\cdot\delta I_2^*(k_x,k_y)\}}{\langle I_1\rangle\langle I_2\rangle} \tag{5.4}$$

The correlation is then normalised to the product of the ensemble average of the intensity distributions.

In a speckle produced by strong scattering, the average intensity of the speckle is equivalent to the standard deviation of the speckle intensity, as shown in equation 2.30. This substitution leads to the final calculation

$$C_{12}(x,y) = \frac{\mathcal{F}^{-1}\{\delta I_1(k_x,k_y)\cdot\delta I_2^*(k_x,k_y)\}}{\sigma_1\sigma_2 N_1 N_2} \tag{5.5}$$

where $N_{1,2}$ is the total number of elements in images 1 and 2 respectively.

In the case of the two speckle patterns being positively spatially correlated, a peak is seen in the correlation at the centre of the overlap of the two speckles. Any disparity between the two intensity patterns is shown as a reduction in this value for the correlation.

5.4.4 Spatial Speckle Correlation Function and the Rayleigh Distribution of Intensities

When a scattering sample is introduced into the common path of the Sagnac interferometer as depicted in Figure 5.6, a speckle pattern is produced in the far field and seen in the output ports, the intensities measured in port 1 and port 2 present the interference of the two speckle patterns. When the beams are aligned such that they are overlapped on the sample and the angle of incidence of one beam is equal to the angle of reflection of the opposing beam, the intensities of the speckle patterns is correlated according to the optical memory effect as shown in Section 2.3.

By blocking either beam path between the first and second PBS, it is possible to isolate either the clockwise or anticlockwise beam, eliminating any interference, and observing

only the light returned from the sample from one angle of incidence. This can be seen in figures 5.11 and 5.12. The images in figures 5.11 and 5.12 show the speckles detected along port 1 and port 2 for the clockwise and anticlockwise beams. The set up is aligned such that the clockwise and anticlockwise beam paths are coincident on the sample. Along each port, the intensity is correlated such that peaks in intensity are seen in the clockwise and anticlockwise speckles at the same points in the distribution.

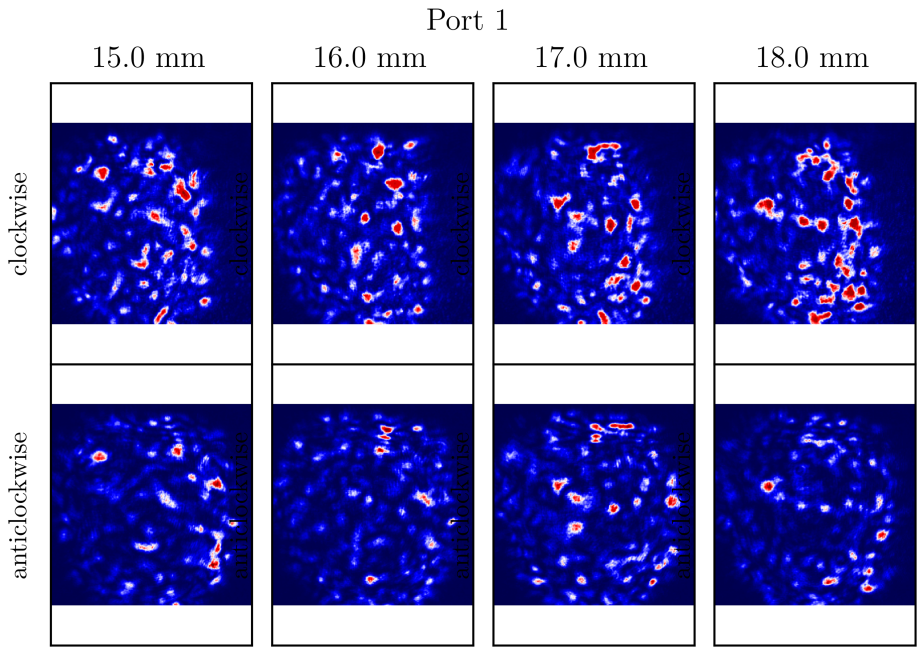

FIGURE 5.11: Example speckles for light scattered from an optical diffuser as a function of translation position across the sample for the clockwise and anticlockwise beam paths. The beams follow a common path in opposite directions in a Sagnac interferometer like geometry. They are then recombined in a Mach-Zehnder like detection path using a nonpolarising 50/50 beam splitter. The beams are isolated in this common detection path by blocking the beams before they enter the common beam path region.

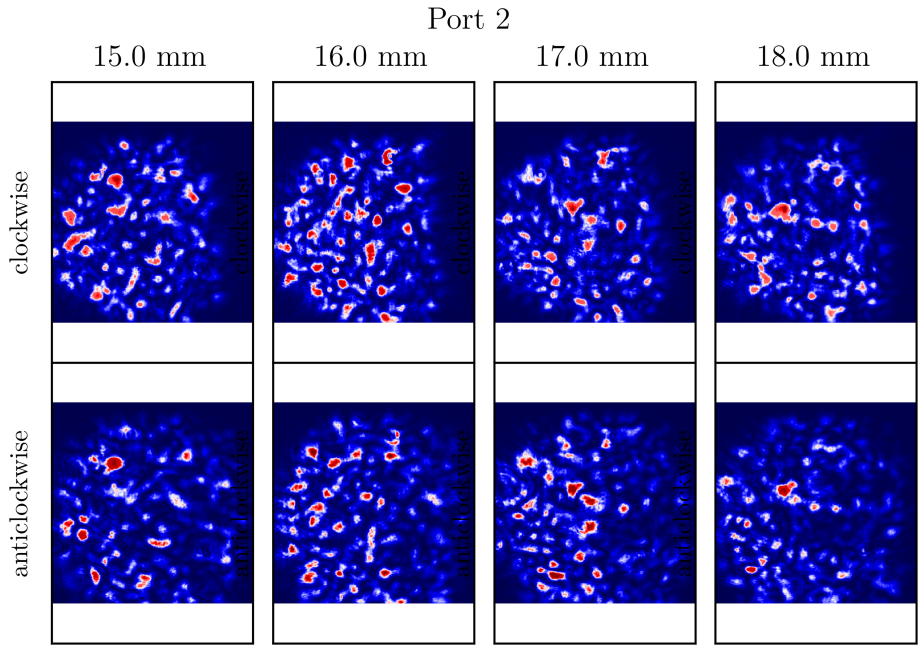

FIGURE 5.12: Example speckles for light scattered from an optical diffuser as a function of translation position across the sample for the clockwise and anticlockwise beam paths in Port 2.

The spatial correlation of the light that is scattered from the sample is seen in the visual similarity of the clockwise and anticlockwise speckle patterns. This is demonstrated as the sample is translated perpendicularly (along the T axis as shown in Figure 5.6), i.e. multiple realisations of the speckle may be interrogated without the loss of the coincident alignment. This requires careful alignment of the detection apparatus, since there is a relatively small detection aperture, in order to observe the exact same projection of the clockwise and anticlockwise scattered light. It is also seen in Section 5.4.5 that the spatial correlation is very sensitive to the relative depth of the sample, since a small displacement of the sample from the plane in which the two beams overlap causes a relatively large change in the relative positions of the two beams on the sample. This can be counteracted using spatial beam expansion to increase the beam width along the counter-propagating paths, however this also leads to strong back-reflections due to the lenses introduced, which significantly impacts the detection of the speckle patterns.

An example of the spatial correlation function is shown in 5.13. A peak is seen in the centre of the spatial correlation function, where the two speckle patterns are most correlated. By measuring the peak of this value within a small range, it is possible to account for slight misalignment of the intensity distributions due to the selection of the origin of the speckle images.

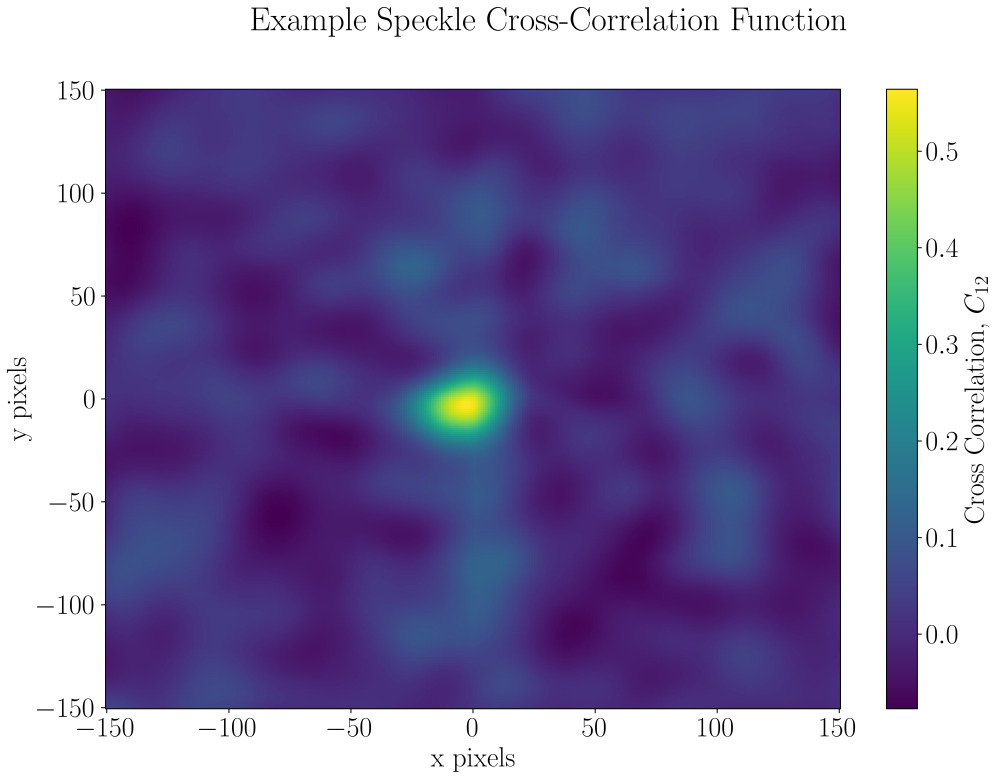

FIGURE 5.13: Example of the two dimensional cross correlation calculated using the Fourier transform of the speckle intensity patterns as presented in equation 5.5. As expected there is a sharp peak in the centre of the cross correlation, where there is maximum correlation in the speckle intensities. The measured cross correlation is taken using a single realisation of the speckle for the clockwise and anticlockwise beams along port 1 of the detection arm.

The speckle itself changes for the clockwise and anticlockwise beams as a function of their displacement across the surface of the sample, as well as from the change in angle from the sample illumination area to the detection point due to the translation of the point of incidence. It is the former which gives the larger contribution to the overall change in the correlation, since the change in scattering angle of the sample will be very small when measured at a significant distance from the detector.

The Rayleigh distribution of intensities in a given speckle predicts an intensity probability density profile as follows equation 2.31. This is shown in Figure 5.14 as a dashed line.

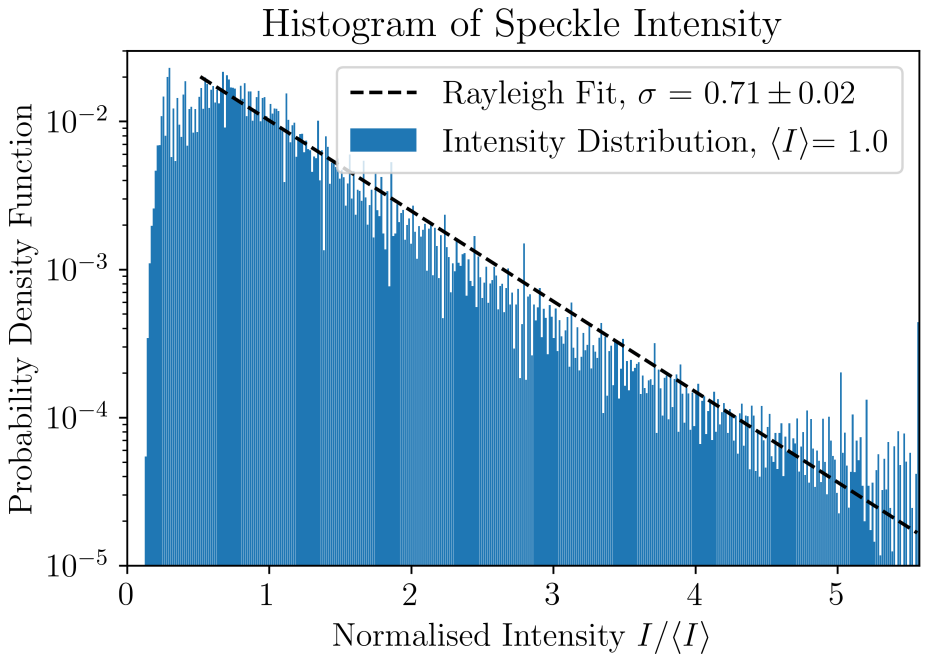

FIGURE 5.14: Probability density function for the measured intensity over an ensemble of 60 realisations of the speckle. The intensity is normalised to the mean intensity, measured for each speckle pattern. The distribution is fit using equation 2.31, exhibiting a variance, $\langle I \rangle$, of 0.71. This is in agreement with the expected value for an isolated polarisation channel for speckles which undergo depolarisation under multiple scattering.

An ensemble of 60 normalised speckles is measured in Figure 5.14 and the probability density function is fit to theory according to a Rayleigh distribution with a standard deviation, $\sigma = 0.71 \pm 0.02$. When normalised to the expected intensity, measured as the mean intensity over the ensemble average of the speckle patterns, a contrast $C = 0.71$ is shown. The reduction in the contrast from unity is not due to the finite pixelation of the image; as can be seen in figures 5.11 and 5.12, the individual speckle resolution is seen to be much smaller than the CCD pixelation(90). The major contribution to this reduction in the contrast is the depolarisation of light at the surface of the sample, since the speckle is in each case measured in an isolated polarisation channel parallel to it's input. The measured intensity contrast can therefore be expected to reduce by a factor of $1/\sqrt{2}$ or ~ 0.707 (91). This result is significant as it enables the substitution of the ensemble average intensity for the standard deviation of the speckles when calculating the cross correlation function (equation 5.5

5.4.5 Depth Detection Using Spatial Correlation

By measuring the spatial correlation function as a function of the sample displacement from the plane of overlap of the clockwise and counter-clockwise beams, it is possible

to show that the peak correlation occurs at the point of maximum overlap. The results of this measurement are shown in Figure 5.17. This is the equivalent of looking at the sample depth relative to the source(s) along the z axis, which runs along the line which bisects the incident beams (as shown in Figure 5.6). An illustration of the beam displacement, Δr is given in Figure 5.15. The total correlation between the samples is given by the double convolution of the beam profiles of the two sources with the correlation function for two sources at a given angle of incidence and reflection separated by a small distance, Δr, as described in equation 2.23.

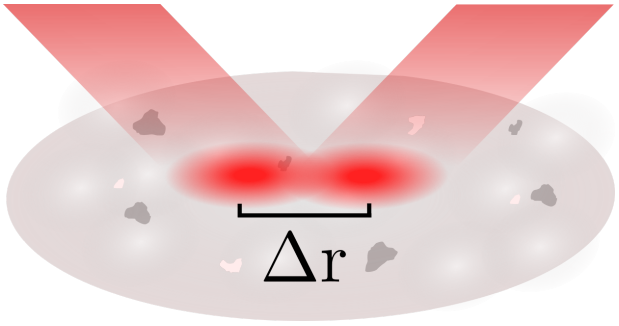

FIGURE 5.15: An illustrative example of the shift in the relative positions of the incident beams on the sample due to a change in the sample depth. As the sample moves away from the exact point of coincidence, the beams shift by a given distance Δr, which is given trigonometrically by the sample displacement and the angle of incidence.

The dependence of the correlation function upon the small displacement is a negligible contributor to the correlation of beams of width $\sim 0.5\,mm$. Assuming the transport mean free path to be of the order of several microns as measured using the angular memory effect, the elastic mean free path is on a shorter length scale, meaning that any correlation between realisations of the speckles falls off at a rate of at least $e^{-\Delta r/l_s}$. The form factor is therefore analogous to a delta-dirac function in experiments on this length scale. Thus the fits to the correlation as a function of the beam separation reverts to that of a Gaussian distribution.

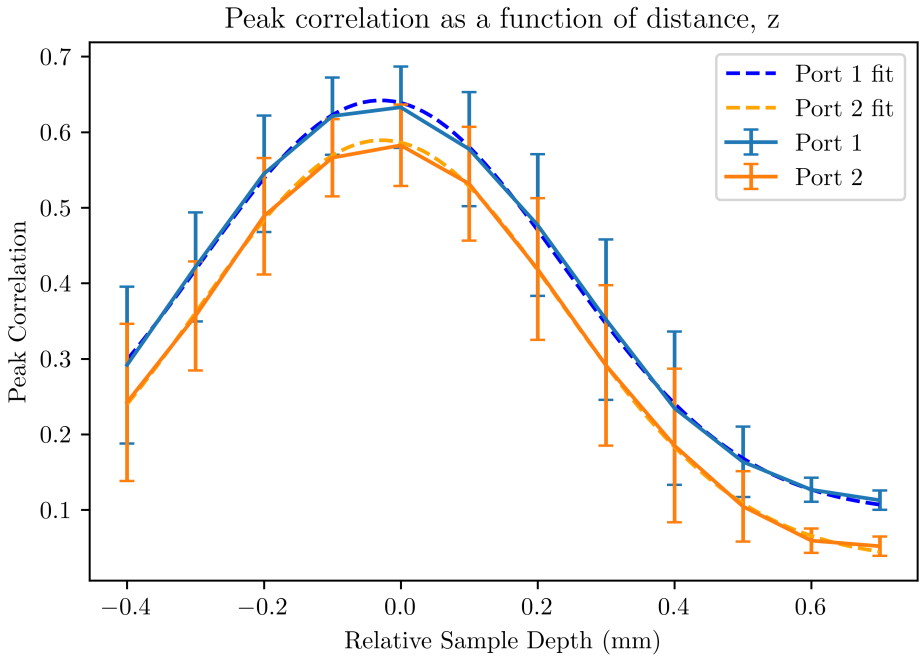

FIGURE 5.16: The peak cross correlation is measured for various sample positions as a function of sample "depth", displacement as measured along the z axis shown in Figure 5.6. The correlation is expected to be limited by the convolution of the beam intensity profiles as they begin to overlap and then separate. Assuming a Gaussian beam profile of the initial laser source, the fits are of a Gaussian distribution.

The cross correlation between the time reverse paths is shown as a function of the relative displacement Δz along the z axis in Figure 5.16. This shows a distinctive peak correlation at the point of maximum overlap of the two beams. The relative separation of the beams at the sample is calculated trigonometrically as $\Delta r = \Delta z \tan(\theta_i)$, where θ_i is the angle of incidence relative to the normal of the surface.

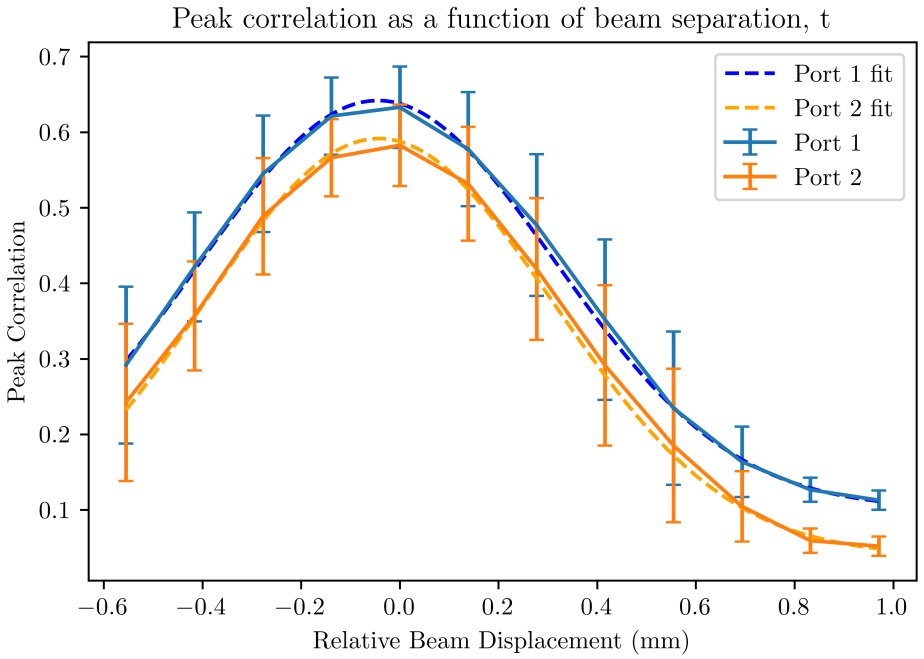

FIGURE 5.17: The peak cross correlation measured as a function of the relative displacement of the centre of the beams on the surface of the sample (Δr). The correlation is expected to be limited by the convolution of the beam intensity profiles as they begin to overlap and then separate. Assuming a Gaussian beam profile the fits follow a Gaussian distribution.

The Gaussian fits to the sample peak correlation merely describe the convolution of the beam intensity profiles, their mean FWHM to be calculated as

$$FWHM = \frac{2\sqrt{2\ln(2)}}{\sqrt{2}}\sigma = 2\ln(2)\sigma, \tag{5.6}$$

where σ is the standard deviation of the convolution, as measured from the time reverse set up. The FWHM of the is found to be $FWHM = 0.73 \pm 0.02\,mm$ with a mean amplitude of 0.55 ± 0.01 and an average background constant of 0.70 ± 0.01, as an average across both of the detection ports. This result illustrates the powerful nature of the speckle correlation provided by the time reverse memory effect that, despite the relatively weak scattering in the given sample, the spatial extent of the correlation function as measured in the free space geometry is predominantly a function of the width of the outgoing beams.

5.4.6 Angular Dependence of the Correlation Coefficient

The angular dependence of the spatial correlation function was also investigated. The 2D spatial correlation was measured as a function of the normal of the surface of the sample to the line which bisects the counter-propagating beams. This was achieved

by rotating the sample about the point of coincidence such that the position of the two beams on the surface of the sample remained steady, thus probing the dependence of the relative angle of incidence and reflection of the two beams. This effect is then shown in Figure 5.18. A fit to the measured data is also shown, following equation 2.21

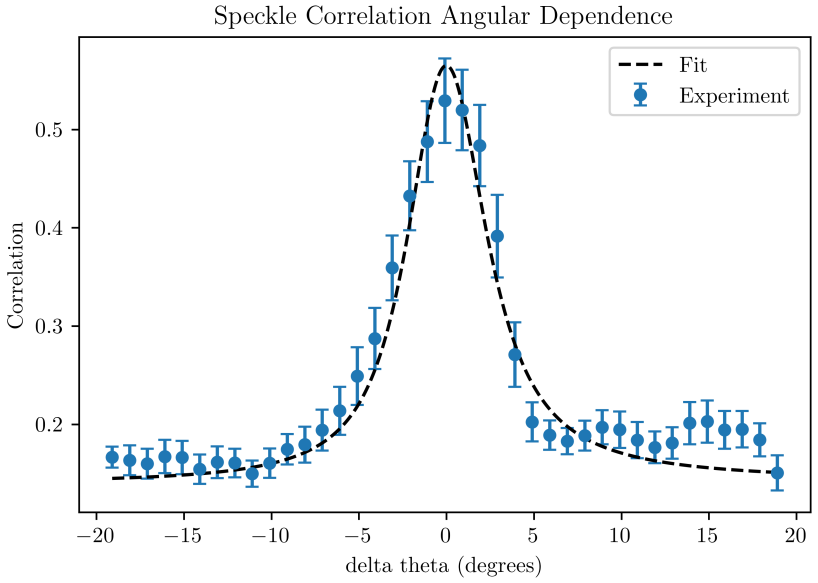

FIGURE 5.18: Experimental measurement and theoretical fit to the angular dependence of the peak of the spatial correlation function following equation 2.21, measured as a function of the difference in angle of incidence and angle of detection relative to one another. Plot shows a 10 point moving average of the data set with a standard deviation over 6 repeat measurements.

The data can also be expressed as a function of the transverse component of the wave vector of the incoming light, relative to it's counter-propagating component. In this case the peak is centred around the value which represents the geometry of the interferometer, where the incoming and outgoing beams are co-propagating along the direction of detection.

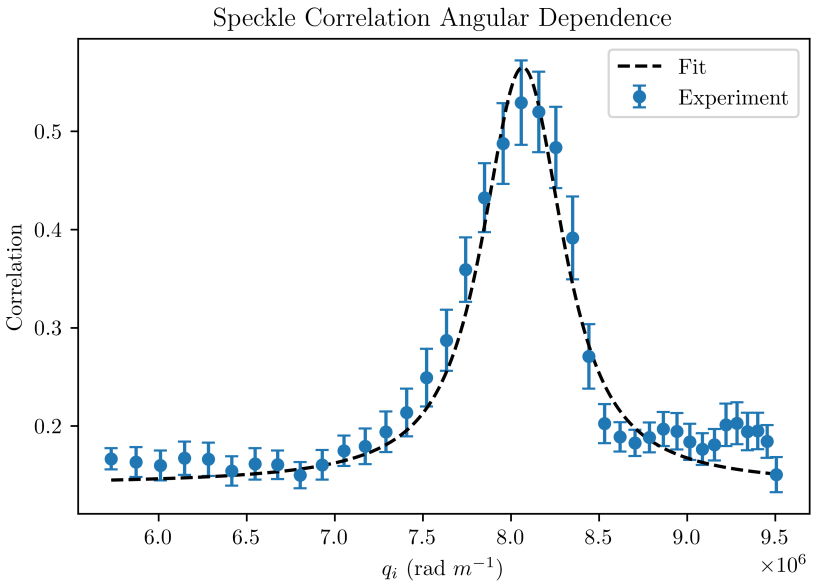

FIGURE 5.19: Experimental measurement and theoretical fit to the angular dependence of the spatial correlation function following equation 2.21, given as a function of the absolute value of the transverse wave vector, q_i, relative to the normal to the surface of the sample. Plot shows a 10 point moving average of the data set with a standard deviation over 6 repeat measurements.

The experimental data is fit to theory following equation 2.21, with the fitting parameters $l_t = 4.3\,\mu m$, $L = 8.6\,\mu m$, and with a background constant of 0.14.

5.4.7 Survival of Phase in the Time Reverse Memory Effect

The time reversal symmetry of the multiple scattering process is what gives rise to the correlations given in the optical memory effect, as described in Section 2.3. It is therefore the preservation of phase during this multiple scattering regime which leads to a constant phase difference between the counter-propagating paths, leading to the constructive and deconstructive interference seen in the speckle pattern produced when recombined in a reflection geometry such as that shown in Figure 5.6. When the reflected speckles are combined so as to produce the signals detected in ports 1 and 2, it is apparent that due to the change in phase induced by reflection at the non-polarising beamsplitter, a constructive interference of speckles produced in the clockwise and counter-clockwise beams in port 1 will lead to a deconstructive interference of those same speckles in port 2. This presents a problem when attempting to use the time reversal symmetry of a system to determine information from the sample such as the time of flight or intensity of signal, since two detectors are required to be analysed and compared or combined simultaneously. There is also an issue of de-phasing during the time of flight of the beams, an issue which is not present in an optical laboratory setup (given there are no large convection currents to introduce a large flow of air along the

beam-path), but which become non-negligible over practical distances, or when probing through dynamic systems.

A possible solution to this problem is to adjust the phase of one of the beams relative to the other, such that the interference at the recombined region is always constructive along one of the detection ports. Experimentally this is achieved using a simple phase delay consisting of a thin glass slide ($L \approx 150\mu m$) attached to a piezoelectric motor which can be driven with a DC voltage in order to change the relative angle of the glass, and therefore the relative phase of the beam. Refraction caused by the thin glass and small change in angle lead to a very small change in the beam path which is compensated for before measurements take place.

The relationship between the supplied voltage, and by direct association the relative phase between the two beams, and the peak value of the two dimensional cross correlation of the speckles produced along the two ports is given in figures 5.20 - 5.22.

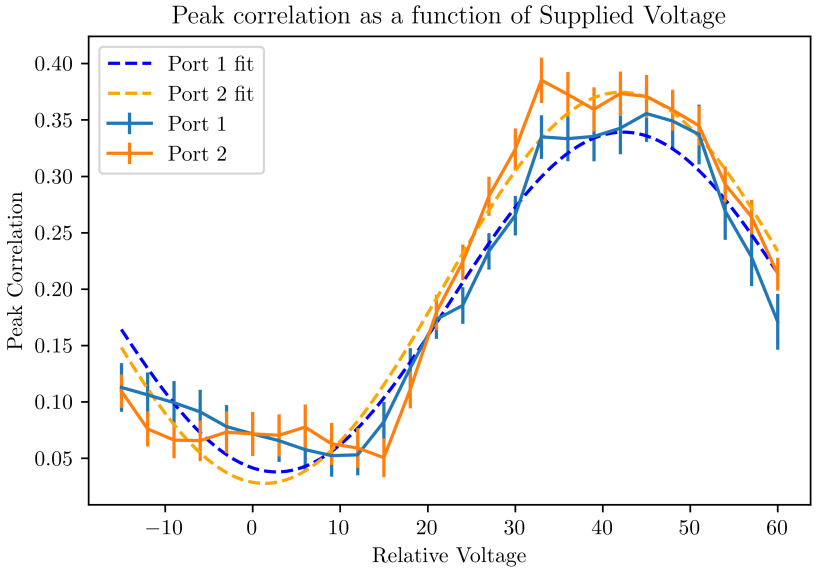

FIGURE 5.20: Measurement of the peak correlation between the clockwise and anticlockwise beams for a given relative voltage. Fits use a sinusoidal relationship, assuming direct proportionality between voltage supplied to the phase delay and the induced phase change. Error bars represent averaging over 21 realisations of the speckle.

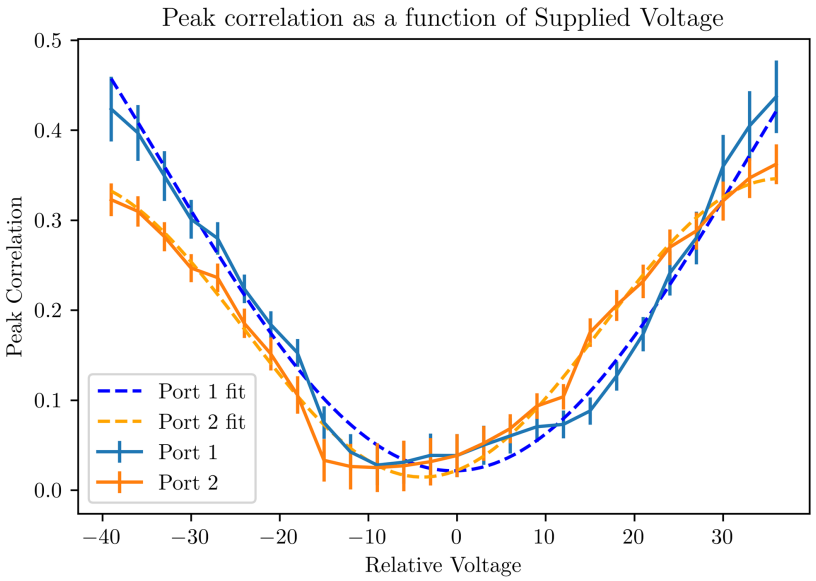

FIGURE 5.21: Peak correlation as a function of the relative phase between the incident beams. Error bars represent averaging over 21 realisations of the speckle. Fits are of a sinusoidal relationship, representing the induced change in phase.

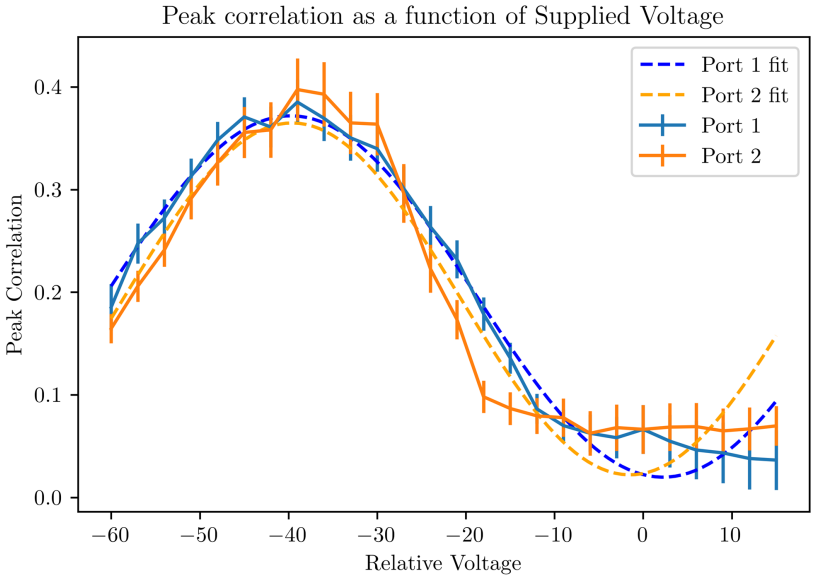

FIGURE 5.22: Peak correlation as a function of the relative phase between the incident beams. Error bars represent averaging over 21 realisations of the speckle. Fits are of a sinusoidal relationship representing the induced change in phase.

The cross correlation between the speckle patterns in ports one and two are measured in the time reverse geometry over 21 realisations of the speckle, achieved by translating the sample. Error bars are shown as the standard deviation of the peak correlation across the 21 sample positions. The sinusoidal relationship shows agreement with the change in relative phase induced in the arms leading to a constructive and deconstructive interference of each speckle across the entirety of the detection field.

5.5 Conclusion

In this chapter, an experimental investigation of the phase dependence of the time reverse optical memory effect has been undertaken. The spatial and angular dependence of the correlation of time reverse scattering geometry has been measured to a high degree of accuracy and found to corroborate previous theoretical and experimental results. The phase of light has been shown to be preserved in the multiple scattering time reverse memory effect, enabling active control of interference of the time reverse paths using a phase delay, and corroborating previous spatial phase modulation experiments undertaken predominantly in transmission. The active control is combined with a Mach-Zehnder interferometer-like detection geometry to show the correlation exhibited between reflected speckles within the Lorentz-reciprocal geometry when a π relative phase shift is introduced.

Additionally, initial experiments are undertaken which show that the phase modulation of the Sagnac interferometer may be extended to the high frequency pulsed regime and combined with single photon counting detection methods, enabling high resolution time of flight measurement. The robustness of the effect is also demonstrated over long time intervals, showing that perturbations to the phase delay due to environmental effects do not significantly impact the detected normalised signal. The system also implements the use of a single photon counting device, locked to a trigger frequency measured directly by the laser, which could enable a quantum statistical approach to exploring these interactions in the TRME, as well as drastically increasing the detection limit.

Chapter 6

Conclusions & Future Work

6.1 Conclusions

The summary of outcomes of the thesis are as follows:

- The transport of light in a strongly scattering random environment has been characterised using a novel experimental pump probe technique, which makes use of photo-induced absorption to measure the spatial and temporal propagation of near-infrared light.
- The pump probe technique was used to measure anisotropic scattering in thin, strongly scattering nanowire mats, showing a significant deviation of the diffusion constant in the longitudinal and transverse directions. This was corroborated using mechanical compression to reduce the diffusion constant in all directions across two different nanowire samples.
- The phase dependence of the time reverse memory effect was experimentally measured in the Sagnac interferometer-like reflection geometry, by examining the cross correlation of superposed speckles in a combined Mach-Zehnder interferometer detection system. This system was then applied to a pulsed optical system and the robustness of the effect was shown under time-resolved measurements.

The results presented in this thesis demonstrate the application of an ultra-fast pump probe technique to measure the diffuse propagation of light in random media. The separation of the diffusion constant into its vector components opens the way to a more detailed study of anisotropic light matter interaction. The detection method has demonstrated measurements of long light paths in strongly scattering nanowires. Utilising the non-linear transient absorption demonstrated in GaP, a methodology was produced to

identify and remove any contribution to the signal from thermalisation of the photo-excited electrons. The measurement of the diffusion constant resulted in the determination of an anisotropy of 1.65 and 1.47 in the transverse and longitudinal directions.

The optical memory effect has been investigated and results were found to be in agreement with established theory of the correlation of time reversal symmetry. A novel Mach-Zehnder detection geometry has been introduced, allowing for the determination of interference effects on the speckles produced in the time reverse memory effect. It is shown that the speckles produced become anti-correlated when recombined due to the reflection at the sample. This can be altered by introducing a phase delay which shows that the entire speckle may be switched between states. This effect is similar to wavefront shaping experiments used frequently in transmission but not demonstrated under time reversal symmetry until now. Finally the methodology was applied to the pulsed regime, in which a demonstration of the effect in time of flight measurements was shown using specular reflection, opening the door to further applications in target signal detection and ranging, as well as quantum statistical analysis thanks to the implementation of single photon counting.

6.2 Future Work

The time of flight pump probe measurements will benefit greatly from larger statistical averaging, especially when combined with a subject sample which is anisotropic in the dimensions transverse to the light propagation. This will likely lead to a greater certainty of the presence or absence of mesoscopic interactions in the light transport through such strongly scattering media. The system benefits from wavelength tunability of both the pump and probe, although sufficient power was not able to be generated at a low enough wavelength in order to study the titania nanoparticles.

In the search for Anderson localisation of light in three dimensions, this experiment offers a powerful technique to measure the spatial and temporal mesoscopic evolution of light in strongly scattering media. Future sample systems, which may exhibit properties of interest in the near infra-red or visible region, may make use of novel fabrication techniques to design materials with tunable anisotropy and scattering strength (54) (8) (92). Ultimately this may enable further progress towards the elusive goal of determining three dimensional Anderson localisation of light(60).

The optical memory effect is well established in transmission geometries, where most applications are found in real world environments. However a full experimental investigation of the possible improvements that can be made thanks to the time reversal symmetry introduced using the Sagnac interferometer geometry is still lacking. These measurements establish a methodology which can be combined with techniques established in previous works in the transmission geometry. The interference of the speckle

subject to the spatial correlation also provides a powerful noise rejection tool in the established long distance detection methods. A strongly scattering sample could also be used to identify the higher order contributions to the correlation function, allowing for confirmation of their phase dependence and the full description of this phenomenon. The single photon counting implemented in the pulsed apparatus also demonstrates the possibility of statistical measurement of the quantum interference in the time reverse optical memory effect.

References

[1] Diederik S. Wiersma. Disordered photonics. *Nature Photonics*, 7:188–196, 3 2013. ISSN 1749-4885. .

[2] Filippo Pratesi, Matteo Burresi, Francesco Riboli, Kevin Vynck, and Diederik S. Wiersma. Disordered photonic structures for light harvesting in solar cells. *Optics Express*, 21:A460, 5 2013. ISSN 1094-4087. .

[3] James R. Nagel and Michael A. Scarpulla. Enhanced absorption in optically thin solar cells by scattering from embedded dielectric nanoparticles. *Optics Express*, 18:A139, 6 2010. ISSN 1094-4087. .

[4] Matthieu Dupré, Liyi Hsu, and Boubacar Kanté. On the design of random metasurface based devices. *Scientific Reports*, 8:1–9, 12 2018. ISSN 20452322. .

[5] Diederik S. Wiersma. The physics and applications of random lasers. *Nature Physics*, 4:359–367, 2008. ISSN 17452481. .

[6] S. E. Skipetrov and J. H. Page. Red light for anderson localization. *New Journal of Physics*, 18, 2016. ISSN 13672630. .

[7] T Sperling, L Schertel, M Ackermann, G J Aubry, C M Aegerter, and G Maret. Can 3d light localization be reached in 'white paint'? *New Journal of Physics*, 18:013039, 1 2016. ISSN 1367-2630. .

[8] Alexey Yamilov, Sergey E Skipetrov, Tyler W Hughes, Momchil Minkov, Zongfu Yu, and Hui Cao. Anderson localization of electromagnetic waves in three dimensions. *Nature Physics*, 2023. .

[9] Isaac Freund, Michael Rosenbluh, and Shechao Feng. Memory effects in propagation of optical waves through disordered media. *Physical Review Letters*, 61: 2328–2331, 1988. ISSN 00319007. .

[10] Antton Goïcoechea, Sergey E. Skipetrov, and John H. Page. Suppression of transport anisotropy at the anderson localization transition in three-dimensional anisotropic media. *Physical Review B*, 102, 12 2020. ISSN 24699969. .

[11] Tom Strudley, Tilman Zehender, Claire Blejean, Erik P. A. M. Bakkers, and Otto L. Muskens. Mesoscopic light transport by very strong collective multiple scattering in nanowire mats. *Nature Photonics*, 7:413–418, 5 2013. ISSN 1749-4885. .

[12] Gustav Mie. Beiträge zur optik trüber medien, speziell kolloidaler metallösungen. *Annalen der Physik*, 330:377–445, 1 1908. ISSN 00033804. .

[13] Qian Zhao, Ji Zhou, Fuli Zhang, and Didier Lippens. Mie resonance-based dielectric metamaterials. *Materials Today*, 12:60–69, 2009. ISSN 13697021. .

[14] Tatsuki Hinamoto, Shinnosuke Hotta, Hiroshi Sugimoto, and Minoru Fujii. Colloidal solutions of silicon nanospheres toward all-dielectric optical metafluids. *Nano Letters*, 20:7737–7743, 10 2020. ISSN 1530-6984. .

[15] Kwanyong Seo, Munib Wober, Paul Steinvurzel, Ethan Schonbrun, Yaping Dan, Tal Ellenbogen, and Kenneth B. Crozier. Multicolored vertical silicon nanowires. *Nano Letters*, 11:1851–1856, 4 2011. ISSN 15306984. .

[16] R A Shelby, D R Smith, and S Schultz. Experimental verification of a negative index of refraction. *Science*, 292:77–80, 2001.

[17] J. B. Pendry. Negative refraction makes a perfect lens. *Physical Review Letters*, 85: 3966–3969, 2000. ISSN 00319007. .

[18] P. Spinelli, M. A. Verschuuren, and A. Polman. Broadband omnidirectional antireflection coating based on subwavelength surface mie resonators. *Nature Communications*, 3:1–5, 2012. ISSN 20411723. .

[19] Isabelle Staude, Andrey E. Miroshnichenko, Manuel Decker, Nche T. Fofang, Sheng Liu, Edward Gonzales, Jason Dominguez, Ting Shan Luk, Dragomir N. Neshev, Igal Brener, and Yuri Kivshar. Tailoring directional scattering through magnetic and electric resonances in subwavelength silicon nanodisks. *ACS Nano*, 7:7824–7832, 2013. ISSN 19360851. .

[20] Arseniy I Kuznetsov, Andrey E Miroshnichenko, Yuan Hsing Fu, Jingbo Zhang, and Boris Luk. Magnetic light. *Scientific Reports*, pages 1–6, 2012. .

[21] Chengyun Zhang, Yi Xu, Jin Liu, Juntao Li, Jin Xiang, Hui Li, Jinxiang Li, Qiaofeng Dai, Sheng Lan, and Andrey E. Miroshnichenko. Lighting up silicon nanoparticles with mie resonances. *Nature Communications*, 9:2964, 12 2018. ISSN 2041-1723. .

[22] Andrey B Evlyukhin, Sergey M Novikov, Urs Zywietz, Rene Lynge Eriksen, Carsten Reinhardt, Sergey I Bozhevolnyi, and Boris N Chichkov. Demonstration of magnetic dipole resonances of dielectric nanospheres in the visible region. *Nano Letters*, 2012.

[23] M. Garín, R. Fenollosa, R. Alcubilla, L. Shi, L. F. Marsal, and F. Meseguer. All-silicon spherical-mie-resonator photodiode with spectral response in the infrared region. *Nature Communications*, 5:3440, 5 2014. ISSN 2041-1723. .

[24] Otto L. Muskens, Silke L. Diedenhofen, Maarten H.M. Van Weert, Magnus T. Borgström, Erik P.A.M. Bakkers, and Jaime Gómez Rivas. Epitaxial growth of aligned semiconductor nanowire metamaterials for photonic applications. *Advanced Functional Materials*, 18:1039–1046, 4 2008. ISSN 1616-3028. .

[25] P. W. Anderson. Absence of diffusion in certain random lattices. *Physical Review*, 109:1492–1505, 3 1958. ISSN 0031899X. .

[26] Sajeev John. Strong localization of photons in certain disordered dielectric superlattices. *Volume 58, Issue 23, Pages 2486 - 2489*, 58:2486–2489, 1987. ISSN 00319007. .

[27] Eli Yablonovitch. Inhibited spontaneous emission in solid-state physics and electronics. *Physical Review Letters*, 58:2059 – 2062, 1 1987. ISSN 00319007. .

[28] Otto L. Muskens, A. Femius Koenderink, and Willem L. Vos. Broadband coherent backscattering spectroscopy of the interplay between order and disorder in three-dimensional opal photonic crystals. *Physical Review B*, 83:155101, 4 2011. ISSN 1098-0121. .

[29] Kevin Vynck, Romain Pierrat, Luis S Froufe-P ´ Erez, Frank Scheffold, Riccardo Sapienza, Silvia Vignolini, Juan José Jos´, and José Sáenz. Light in correlated disordered media. *Reviews of Modern Physics*, 95, 2023. .

[30] Pierre Etienne Wolf and Georg Maret. Weak localization and coherent backscattering of photons in disordered media. *Physical Review Letters*, 55:2696–2699, 1985. ISSN 00319007. .

[31] Meint P.Van Albada and Ad Lagendijk. Observation of weak localization of light in a random medium. *Physical Review Letters*, 55:2692, 12 1985. ISSN 00319007. .

[32] Eric Akkermans and Gilles Montambaux. Mesoscopic physics of photons. *Journal of the Optical Society of America B*, 21:101, 2004. ISSN 0740-3224. .

[33] E Akkermans, P E Wolf, R Maynard, and G Maret. Theoretical study of the coherent backscattering of light by disordered media. *Journal de Physique*, 49:77–98, 1988. ISSN 0302-0738. .

[34] Martin B. Van Der Mark, Meint P. Van Albada, and Ad Lagendijk. Light scattering in strongly scattering media: Multiple scattering and weak localization. *Physical Review B*, 37:3575–3592, 1988. ISSN 01631829. .

[35] Otto L. Muskens, Silke L. Diedenhofen, Bernard C. Kaas, Rienk E. Algra, Erik P.A.M. Bakkers, Jaime Gómez Rivas, and Ad Lagendijk. Large photonic strength of highly tunable resonant nanowire materials. *Nano Letters*, 9:930–934, 2009. ISSN 15306984. .

[36] R. Sapienza, P. D. García, J. Bertolotti, M. D. Martín, Á Blanco, L. Viña, C. López, and D. S. Wiersma. Observation of resonant behavior in the energy velocity of diffused light. *Physical Review Letters*, 99:1–4, 2007. ISSN 00319007. .

[37] L. Schertel, G. J. Aubry, C. M. Aegerter, and G. Maret. Coherent multiple light scattering in faraday active materials. *European Physical Journal: Special Topics*, 226: 1409–1421, 5 2017. ISSN 19516401. .

[38] Otto L. Muskens, Paul Venn, Timmo van der Beek, and Thomas Wellens. Partial nonlinear reciprocity breaking through ultrafast dynamics in a random photonic medium. *Physical Review Letters*, 108:223906, 5 2012. ISSN 0031-9007. .

[39] Ad Lagendijk, Bart Van Tiggelen, and Diederik S. Wiersma. Fifty years of anderson localization. *Physics Today*, 62:24–29, 2009. ISSN 00319228. .

[40] Hefei Hu, A. Strybulevych, J. H. Page, S. E. Skipetrov, and B. A. Van Tiggelen. Localization of ultrasound in a three-dimensional elastic network. *Nature Physics 2008 4:12*, 4:945–948, 10 2008. ISSN 1745-2481. .

[41] L. A. Cobus, S. E. Skipetrov, A. Aubry, B. A. Van Tiggelen, A. Derode, and J. H. Page. Anderson mobility gap probed by dynamic coherent backscattering. *Physical Review Letters*, 116:1–5, 2016. ISSN 10797114. .

[42] Tal Schwartz, Guy Bartal, Shmuel Fishman, and Mordechai Segev. Transport and anderson localization in disordered two-dimensional photonic lattices. *Nature*, 446:52–55, 2007. ISSN 14764687. .

[43] J. T. Edwards and D. J. Thouless. Numerical studies of localization in disordered systems. *Journal of Physics C: Solid State Physics*, 5:807, 4 1972. ISSN 0022-3719. . URL https://iopscience.iop.org/article/10.1088/0022-3719/5/8/007https://iopscience.iop.org/article/10.1088/0022-3719/5/8/007/meta.

[44] Patrick A. Lee and T. V. Ramakrishnan. Disordered electronic systems. *Reviews of Modern Physics*, 57:287, 4 1985. ISSN 00346861. . URL https://journals.aps.org/rmp/abstract/10.1103/RevModPhys.57.287.

[45] R Rezvani Naraghi, S Sukhov, J J Sáenz, and A Dogariu. Near-field effects in mesoscopic light transport. *Physical Review Letters*, 2015. .

[46] Roxana Rezvani Naraghi and Aristide Dogariu. Phase transitions in diffusion of light. *Physical Review Letters*, 117:1–5, 2016. ISSN 10797114. .

[47] Jose M. Escalante and Sergey E. Skipetrov. Longitudinal optical fields in light scattering from dielectric spheres and anderson localization of light. *Annalen der Physik*, 529:1700039, 8 2017. ISSN 15213889. .

[48] Gilberto F. de Sá, Gabriel F. Basso, V. A. Ermakov, Niklaus U. Wetter, F. C. Marques, Weliton S. Martins, M. C. S. Xavier, Ernesto Jimenez-Villar, and Valdeci Mestre. Anomalous transport of light at the phase transition to localization: strong dependence with incident angle. *Photonics Research, Vol. 6, Issue 10, pp. 929-942*, 6: 929–942, 10 2018. ISSN 2327-9125. .

[49] S.E. Skipetrov and I. M. Sokolov. Absence of anderson localization of light in a random ensemble of point scatterers. *Physical Review Letters*, 112:023905, 1 2014. ISSN 0031-9007. .

[50] Laura A. Cobus, Georg Maret, and Alexandre Aubry. Transient critical regime for light near the three-dimensional anderson transition. *ArXiV*, 9 2021.

[51] Yuri Kivshar and Andrey Miroshnichenko. Meta-optics with mie resonances, 2017. ISSN 1047-6938.

[52] T. Sperling, W. Bührer, C. M. Aegerter, and G. Maret. Direct determination of the transition to localization of light in three dimensions. *Nature Photonics 2012 7:1*, 7: 48–52, 12 2012. ISSN 1749-4893. .

[53] Jakub Haberko, Luis S. Froufe-Pérez, and Frank Scheffold. Transition from light diffusion to localization in three-dimensional amorphous dielectric networks near the band edge. *Nature Communications*, 11:4867, 9 2020. ISSN 2041-1723. .

[54] Frank Scheffold, Jakub Haberko, Sofia Magkiriadou, and Luis S. Froufe-Pérez. Transport through amorphous photonic materials with localization and bandgap regimes. *Physical Review Letters*, 129, 10 2022. ISSN 10797114. .

[55] Ad Lagendijk, Rob Vreeker, and Pedro De Vries. Influence of internal reflection on diffusive transport in strongly scattering media. *Physics Letters A*, 136:81–88, 3 1989. ISSN 0375-9601. .

[56] J. Gómez Rivas, R. Sprik, A. Lagendijk, L. D. Noordam, and C. W. Rella. Static and dynamic transport of light close to the anderson localization transition. *Physical Review E*, 63:046613, 3 2001. ISSN 1063-651X. .

[57] Akira. Ishimaru. *Wave propagation and scattering in random media*. Academic Press, 1978. ISBN 0123747023.

[58] N. Garcia, A. Z. Genack, and A. A. Lisyansky. Measurement of the transport mean free path of diffusing photons. *Physical Review B*, 46:14475–14479, 1992. ISSN 01631829. .

[59] T. Van Der Beek, P. Barthelemy, P. M. Johnson, D. S. Wiersma, and A. Lagendijk. Light transport through disordered layers of dense gallium arsenide submicron particles. *Physical Review B - Condensed Matter and Materials Physics*, 85:115401, 2012. ISSN 10980121. .

[60] B. C. Kaas, B. A. Van Tiggelen, and A. Lagendijk. Anisotropy and interference in wave transport: An analytic theory. *Physical Review Letters*, 100, 3 2008. ISSN 00319007. .

[61] Diederik S. Wiersma, Alessandro Muzzi, Marcello Colocci, and Roberto Righini. Time-resolved experiments on light diffusion in anisotropic random media. *Physical Review E*, 62:6681–6687, 11 2000. ISSN 1063-651X. .

[62] P. D. García, R. Sapienza, J. Bertolotti, M. D. Martín, Á Blanco, A. Altube, L. Viña, D. S. Wiersma, and C. López. Resonant light transport through mie modes in photonic glasses. *Physical Review A*, 78:023823, 8 2008. ISSN 1050-2947. .

[63] Ernesto Pini, Peter Naglic, Miran Bürmen, Alexander Gatto, Henrik Schäfer, Diederik S. Wiersma, and Lorenzo Pattelli. Experimental determination of effective light transport properties in fully anisotropic media. *https://doi.org/10.1117/1.APN.3.5.056017*, 3:056017, 9 2024. ISSN 2791-1519. .

[64] I. M. Vellekoop, P. Lodahl, and A. Lagendijk. Determination of the diffusion constant using phase-sensitive measurements. *Physical Review E - Statistical, Nonlinear, and Soft Matter Physics*, 71:1–11, 2005. ISSN 15393755. .

[65] Patrick M. Johnson, Arnout Imhof, Boris P. J. Bret, Jaime Gómez Rivas, and Ad Lagendijk. Time-resolved pulse propagation in a strongly scattering material. *Physical Review E*, 68:016604, 7 2003. ISSN 1063-651X. .

[66] Eric Akkermans and Gilles Montambaux. *Mesoscopic physics of electrons and photons*, volume 9780521855. Cambridge University Press, 1 2007. ISBN 9780511618833. .

[67] Shechao Feng, Charles Kane, Patrick A Lee, and A Douglas Stone. Correlations and fluctuations of coherent wave transmission through disordered media. *Physical Review Letters*, 61, 1988.

[68] Richard Berkovits and Moshe Kaveh. Time-reversed memory effects. *PHYSICAL REVIEW B*, 41, 1990.

[69] B. Shapiro. Large intensity fluctuations for wave propagation in random media. *Physical Review Letters*, 57:2168–2171, 1986. ISSN 00319007. .

[70] P. Sebbah, B. Hu, A. Z. Genack, R. Pnini, and B. Shapiro. Spatial-field correlation: The building block of mesoscopic fluctuations. *Physical Review Letters*, 88:123901, 3 2002. ISSN 10797114. .

[71] Isaac Freund and Michael Rosenbluh. Time reversal symmetry of multiply scattered speckle patterns. *Optics Communications*, 82:362–369, 9 1991. ISSN 0030-4018. .

[72] Isaac Freund. Time-reversal symmetry and image reconstruction through multiple-scattering media. *JOSA A, Vol. 9, Issue 3, pp. 456-463*, 9:456–463, 9 1992. ISSN 1520-8532. .

[73] Jean-Francois Léger, Sylvain Gigan, Laurent Bourdieu, Jacopo Bertolotti, and Sam Schott. Characterization of the angular memory effect of scattered light in biological tissues. *Optics Express, Vol. 23, Issue 10, pp. 13505-13516*, 23:13505–13516, 9 2015. ISSN 1094-4087. .

[74] Benjamin Judkewitz, Ying Min Wang, Roarke Horstmeyer, Alexandre Mathy, and Changhuei Yang. Speckle-scale focusing in the diffusive regime with time reversal of variance-encoded light (trove). *Nature Photonics 2013 7:4*, 7:300–305, 9 2013. ISSN 1749-4893. .

[75] Benjamin Judkewitz, Roarke Horstmeyer, Gerwin Osnabrugge, Ioannis N Papadopoulos, and Ivo M Vellekoop. Generalized optical memory effect. *Optica, Vol. 4, Issue 8, pp. 886-892*, 4:886–892, 9 2017. ISSN 2334-2536. .

[76] Tom Strudley, Roman Bruck, Ben Mills, and Otto L Muskens. An ultrafast reconfigurable nanophotonic switch using wavefront shaping of light in a nonlinear nanomaterial. *Light: Science & Applications*, 3:e207–e207, 9 2014. ISSN 2047-7538. .

[77] Benjamin Judkewitz, Roarke Horstmeyer, Ivo M. Vellekoop, Ioannis N. Papadopoulos, and Changhuei Yang. Translation correlations in anisotropically scattering media. *Nature Physics 2014 11:8*, 11:684–689, 6 2015. ISSN 1745-2481. .

[78] J. W. Goodman. Some fundamental properties of speckle*. *JOSA, Vol. 66, Issue 11, pp. 1145-1150*, 66:1145–1150, 11 1976. ISSN 0030-3941. .

[79] L. E. McNeil and R. H. French. Multiple scattering from rutile tio2 particles. *Acta Materialia*, 48:4571–4576, 12 2000. ISSN 1359-6454. .

[80] O. L. Muskens, M. T. Borgström, E. P.A.M. Bakkers, and J. Gómez Rivas. Giant optical birefringence in ensembles of semiconductor nanowires. *Applied Physics Letters*, 89, 2006. ISSN 00036951. .

[81] Otto L. Muskens, Jaime Gómez Rivas, Rienk E. Algra, Erik P.A.M. Bakkers, and Ad Lagendijk. Design of light scattering in nanowire materials for photovoltaic applications. *Nano Letters*, 8:2638–2642, 9 2008. ISSN 15306984. .

[82] Mostafa A. El-Sayed. Small is different: Shape-, size-, and composition-dependent properties of some colloidal semiconductor nanocrystals. *Accounts of Chemical Research*, 37:326–333, 5 2004. ISSN 00014842. .

[83] Martina Abb, Erik P.A.M. Bakkers, and Otto L. Muskens. Ultrafast dephasing of light in strongly scattering gap nanowires. *Physical Review Letters*, 106, 4 2011. ISSN 00319007. .

[84] Guanjun Lin, Qian Zhang, Xiaoyu Lin, Dongfang Zhao, Ran Jia, Naikun Gao, Zhiyuan Zuo, Xiangang Xu, and Duo Liu. Enhanced photoluminescence of gallium phosphide by surface plasmon resonances of metallic nanoparticles. *RSC Advances*, 5:48275–48280, 5 2015. ISSN 20462069. .

[85] Taeho Shin, Samuel W. Teitelbaum, Johanna Wolfson, Maria Kandyla, and Keith A. Nelson. Extended two-temperature model for ultrafast thermal response of band gap materials upon impulsive optical excitation. *The Journal of Chemical Physics*, 143:194705, 11 2015. ISSN 0021-9606. .

[86] Martin C. Fischer, Jesse W. Wilson, Francisco E. Robles, and Warren S. Warren. Invited review article: Pump-probe microscopy. *The Review of Scientific Instruments*, 87:031101, 3 2016. ISSN 10897623. .

[87] O. L. Muskens and A. Lagendijk. Method for broadband spectroscopy of light transport through opaque scattering media. *Optics Letters*, 34:395, 2 2009. ISSN 0146-9592. .

[88] Romain Pierrat, Rémi Carminati, and Jean-Jacques Greffet. Photon diffusion coefficient in scattering and absorbing media. *JOSA A, Vol. 23, Issue 5, pp. 1106-1110*, 23:1106–1110, 9 2006. ISSN 1520-8532. .

[89] Jesse Dykes, Zeina Nazer, Allard P. Mosk, and Otto L. Muskens. Imaging through highly scattering environments using ballistic and quasi-ballistic light in a common-path sagnac interferometer. *Optics express*, 28:10386, 3 2020. ISSN 1094-4087. .

[90] J. C. Dainty. I the statistics of speckle patterns. *Progress in Optics*, 14:1–46, 1 1977. ISSN 0079-6638. .

[91] Abhijit Roy. Spatial statistics of superposition of two uncorrelated speckle patterns with polarization diversity. *Results in Optics*, 5:100187, 12 2021. ISSN 2666-9501. .

[92] Evangelos Marakis, Ravitej Uppu, Maryna L. Meretska, Klaas Jan Gorter, Willem L. Vos, and Pepijn W.H. Pinkse. Deterministic and controllable photonic scattering media via direct laser writing. *Advanced Optical Materials*, 8, 12 2020. ISSN 21951071. .